Spin injection, transmission and detection in antiferromagnets

Lamprini Frangou

To cite this version:

Lamprini Frangou. Spin injection, transmission and detection in antiferromagnets. Materials Science [cond-mat.mtrl-sci]. Université Grenoble Alpes, 2017. English. NNT : 2017GREAY079 . tel-01788513

HAL Id: tel-01788513
https://theses.hal.science/tel-01788513v1

Submitted on 9 May 2018

Communauté
UNIVERSITÉ Grenoble Alpes

THÈSE

Pour obtenir le grade de

DOCTEUR DE LA COMMUNAUTE UNIVERSITE GRENOBLE ALPES

Spécialité : **Physique**

Arrêté ministériel : 25 mai 2016

Présentée par

Lamprini FRANGOU

Thèse dirigée par **Vincent BALTZ, Chargé de recherche CNRS au Laboratoire SPINTEC**

préparée au sein du **Laboratoire SPINTEC**
dans **l'École Doctorale de Physique**

Injection, transmission et détection de spin dans les matériaux antiferromagnétiques

Thèse soutenue publiquement le 14 novembre 2017,
devant le jury composé de :

Mme Alexandra MOUGIN
Directrice de recherche CNRS au LPS Orsay, Rapporteure
M. Jörg WUNDERLICH
Ingénieur/chercheur à Hitachi Cambridge, Rapporteur
M. Michel VIRET
Ingénieur/chercheur au CEA Saclay, Membre
Mme Stefania PIZZINI
Directrice de recherche CNRS à l'Institut Néel, Présidente

Acknowledgments

It is a great pleasure to have the opportunity to thank all the people that contributed one way or another to my doctoral work.

First and foremost, I would like to express my sincere gratitude to my supervisor, Vincent Baltz, for his guidance, support and for providing me with the means to carry out this research. For sharing with me his knowledge and ideas. For always being available for discussions and solving problems. For the opportunity to attend all these interesting conferences and workshops that enriched both my scientific and cultural knowledge. Without his guidance and persistent help this dissertation would not have been possible.

There are many people that have devoted their time and knowledge for this work to be completed. In particular, I am indebted to Serge Gambarelli and Vincent Maurel, for allowing me to use their laboratory facilities, at SYMMES, and for their immense help with the EPR machine. Thank you very much! I am also grateful to Ursula Ebels for letting me use the CPW-FMR the last three years. I would also like to thank Isabelle Joumard, for her help and technical assistance with the VSM experiments. Moreover, I am very grateful to Stephane Auffret for fabricating my samples and for sharing his valuable knowledge on materials science.

I would like to further thank Guillaume Forestier and Olga Gladii, for their immense help with the experiments and all the fruitful discussions. Thank you for being a part of this work. Additionally, I would like to thank Laurent Vila and Paul Noël for the advice and help with the spin pumping experiments as well as for all the valuable scientific discussions.

Special thanks go to Rachel Mauduit for helping me with all the administrative duties and responsibilities, as well as to Catherine Broisin.

Furthermore, I must thank all my co-workers at SPINTEC for providing a friendly and stimulating workplace. Special thanks go to my colleagues/friends for being an important part of my life: Paulo, Tan, Alex, Bene, Alexandre, Mathieu, Cecile, Jay, Dali, Nicolas, Daniel, Haozhe, Alexu, Jyotirmoy, Safeer, Paul, Magali, Claire, Anika, Guillermo and Titiksha. Thanks a lot guys!

Finally, I wish to deeply thank my parents, Efstratia and Nikolao, for the encouragement and love with which they have surrounded me during all these years. My brother, Aris and my sister, Katerina for their love and for always being there for me. My friends, Theano and Christoforo for their huge support and all the great moments we have shared with in Grenoble. Last but not least, I must thank Kean for his unconditional love, inspiration and support. Είσαι τα πάντα για μένα!

CONTENTS

Introduction

Electron comprises two fundamental degrees of freedom, the charge and the spin. Over the past years, conventional electronic devices used only the charge of electron in order to store and manipulate information. Currently, electronics have reached the limits of storage density due to the dramatic increase of power consumption as a consequence of scaling-related enhancements. A new concept that could offer a way out is thus highly desired. A major breakthrough in the information technologies occurred in 1988, when A. Fert [8] and P. Grünberg [9] discovered independently the giant magnetoresistance. This discovery heralded the beginning of spintronics field which relies not only on electrons' charge, but also on electrons’ spin, offering perspectives for a new generation of devices [10]. The first application of spintronics in the realm of information processing was spin valves sensors, e. g. used in hard disk drive read heads and later magnetic random access memories, MRAMs [11].

MRAMs are candidates to replace electric current-based memories, due to their non-volatility, large read/write endurance and fast read/write operations. Until recently, the main active components in spintronic devices were ferromagnetic materials, in which the positive exchange interaction between neighboring spins imposes a parallel alignment of the magnetic moments. Current efforts in designing spintronic devices target at a strong and robust control of the magnetic order, while at the same time seeking for more power-efficient route. In traditionally ferromagnetic-based devices this is a fundamental limiting factor, as spurious magnetic fields lead to undesired instabilities, magnetic field cross-talks limit the potentials for high storage density, and high current densities are still required to encode information [11].

The ever increasing demand for speed acceleration and size reduction led researchers to turn their attention toward exploring alternative structures to overcome the drawbacks of ferromagnets. In fact, little attention had been paid to the spin dependent transport properties of their intimate counterparts, that is to say, of antiferromagnets. In antiferromagnetic materials, the exchange interaction is negative in sign leading to an antiparallel alignment of the magnetic moments. Basically, in the simplest case, the antiferromagnet is seen as a sum of two sublattices which spontaneous magnetization point in opposite directions. The latter explains the zero net magnetization present in this kind of magnetic materials. Antiferromagnets are more abundant in nature than ferromagnets. Most interestingly, they also appear in a wide variety of flavors in terms of electrical properties, as they can be metals, insulators, semimetals, semiconductors or even superconductors. Furthermore, the antiferromagnetic ordering can take different forms (e.g. ways how magnetic moments can be arranged on a crystal lattice) in order to obtain zero net magnetic moment. For instance, fully compensated collinear or noncollinear and non-coplanar sublattices with compensated or uncompensated structures can be found in antiferromagnets. Figure 1 shows the crystallographic structures of three antiferromagnets, ranging from metallic to semi metallic to insulating: IrMn, CuMnAs and NiO. Some of them will be discussed in details later in this thesis.

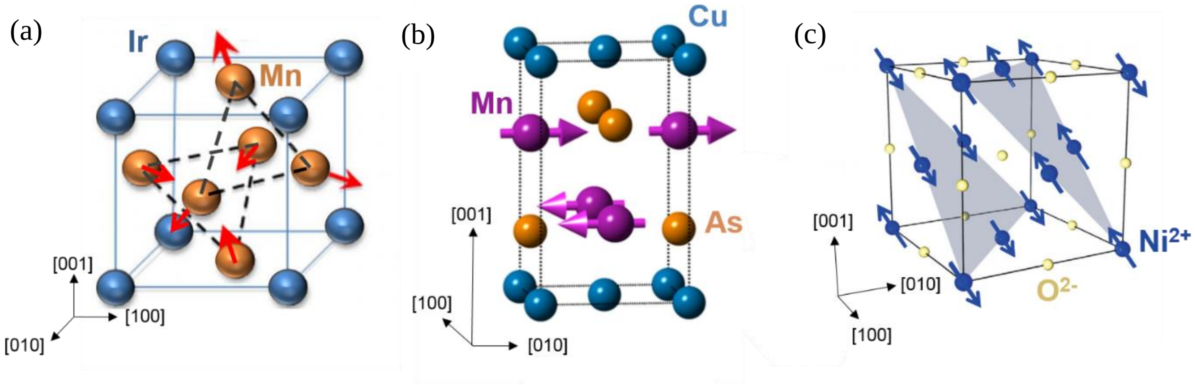

Figure 1 : Crystallographic and spin structure of: (a) metallic γ-IrMn, (b) semi-metallic CuMnAs and (c) insulating NiO. Adapted from Ref. [12–14].

Antiferromagnets comprise unique properties, such as absence of stray fields, robustness to disturbing magnetic fields, ultrafast dynamics and the possibility of generating large magneto-transport effects. Despite, the long list of outstanding features antiferromagnets were once considered as magnetically inactive materials, with no practical application. However, a series of fundamental explorations led to the discovery of exchange anisotropy [15,16], which couples magnetically the ferromagnetic layer adjacent to the antiferromagnet. The latter has been used in spin valve sensors and magnetic random access memories to provide auxiliary support to ferromagnet, by setting a single remanent direction which is used as a reference for the spin of the electrons that are driven through these devices.

Currently, there is an even more ambitious vision for antiferromagnets: to explore their full potentials as active components in spintronic devices, where reading and writing of magnetic information can be achieved in a ferromagnet-free environment. Interest in this possibility has been stimulated by recent theoretical [17] and experimental studies [18–20] which showed that relativistic effects are equally feasible in ferromagnets and antiferromagnets. This vision led to intense research efforts aimed to elucidate spin transport properties in antiferromagnets, which established gradually a new and independent field, known as antiferromagnetic spintronics [21–25]. Spin-transfer effects, spin-orbit effects as well as magnetization dynamics play a crucial role in the field of antiferromagnetic spintronics, providing means for spin manipulation and detection.

An ever growing subset of antiferromagnetic spintronics field is interested in using antiferromagnets to generate, detect and transmit spin currents. One can imagine that using spin currents to transmit information will boost the functionalities of spintronic devices, promising pathways towards lower power consumption and providing solution to the size scalability problem. Nonetheless, due to the wide diversity under which antiferromagnetism appears in nature, the realization of such pure spin devices becomes challenging. Various fundamental parameters specific to antiferromagnets are yet to be determined prior to accomplish a viable device. To this end, several theoretical and experimental studies have been conducted to determine antiferromagnetic spin dependent transport properties [26–33]. Namely, the interfacial spin mixing conductance, which relates to the interfacial transparency, the spin penetration length and relaxation mechanisms, associated to the bulk properties of antiferromagnets, as well as the critical temperature at the nanoscale, which will set the threshold for data retention in future antiferromagnet-based devices. These parameters are of particular importance as they define the strength of the dynamic interaction in antiferromagnets and consequently the efficacy of spin current generation, transmission and detection.

In the frame of this thesis, we investigated spin injection, transmission and detection in both metallic and insulating antiferromagnets, by means of spin pumping. We mainly aim for a better and deeper understanding of the involved effects and phenomena occurring at the antiferromagnetic phase transition and their impact on spin transport.

This thesis is divided into four chapters.

Chapter 1 aims to introduce the reader into the field of antiferromagnetic spintronics. First, we address the role of antiferromagnets in current spintronic devices; spin valve sensors and magnetic memories. The second part of this chapter is dedicated to the most current advances in the field of pure antiferromagnetic spintronics. We mainly discuss about possible ways to read and write the antiferromagnetic configuration.

Chapter 2 is devoted to the experimental results on spin injection and transmission in antiferromagnets. The chapter starts with a brief introduction to magnetic relaxation and spin injection by spin pumping, necessary to understand the experimental procedure and results. Temperature dependence measurements of ferromagnetic relaxation in ferromagnetic-spin-injector / (spin-conductor) / antiferromagnetic-spin-sink bilayer and trilayer systems consisting of different antiferromagnets, both metallic and insulating, are discussed in details in this chapter. In fact, the nature of spin transport, whether it is an electronic or magnonic transport, is defined by the electrical properties of the antiferromagnet and the presence or not of exchange bias. A special attention is given on the effect of linear fluctuations at the antiferromagnetic phase transition on spin pumping.

Chapter 3 summarizes the experimental results obtained in search of electrical detection of spin currents and non-linear spin fluctuations in antiferromagnets. The spin current is injected by spin pumping, like in chapter 2, and detection is achieved by spin Hall effect. First, we discuss about the fundamental principles of the spin Hall effect, along with the necessary conceptual framework to our work. Next, we present our electrical measurements in spin Hall geometry, which revealed a non-monotonous temperature dependence of transverse dc voltage associated to the ferromagnetic layer itself which was unrelated to spin rectification effects. This behavior overshadowed the effects associated to antiferromagnet but triggered interest in potential spin current detection by ferromagnets.

Chapter 4 focuses on tuning the properties of antiferromagnets so that they can be used as functional materials in antiferromagnetic spintronics. These properties were detected by means of ferromagnetic/antiferromagnetic exchange bias. The first section is dedicated to the phenomenology of exchange bias, to some theoretical models and to the methodology used in throughout this chapter. The experiments demonstrate a way to manipulate the spatial dispersion of antiferromagnetic properties in spintronic devices and at the same time how to reduce such dispersions in order to improve simultaneously the thermal stability of antiferromagnets.

At the end, a general conclusion regarding the main achievements of this thesis is given and future perspectives complete the manuscript.

I. Antiferromagnets for spintronics: state of the art

In this chapter, we start by briefly introducing the role of antiferromagnets in current information technology devices, in which they provide only a static supporting role to ferromagnets via the exchange bias phenomenon. Next, we address the recent advances in the field of pure antiferromagnetic spintronics devices, which valorised the spin dependent transport properties of antiferromagnets. This brief introduction intends to define the research field area in which this thesis is situated.

I.1 Current technology

In current spintronic devices, that is to say, in magnetic sensors like magnetoresistive read heads for hard disk drives and in magnetic random access memories, MRAMs [15,34], antiferromagnets provide a static supporting role of enhancing the magnetic stability of ferromagnetic components, via the exchange bias phenomenon [15]. Exchange bias is a fundamental property that occurs when a ferromagnetic layer is coupled to an antiferromagnet. It is manifested as a shift of the hysteresis curve along the magnetic field axis. When the shift is larger than the coercivity, a single remnant state remains. It is said that the antiferromagnet pins the magnetization of the ferromagnetic layer along a reference direction. The basics of exchange bias will be described in Chapter IV.1. For now we simply recall that pinning by exchange bias sets a reference direction for the spin of electrons flowing through a device. This is of crucial importance for reading, as will be discussed thereafter. It should be emphasized that, in a reciprocal manner, the antiferromagnetic order can be manipulated and studied via exchange bias [24]. Later in this manuscript, exchange bias is used as a tool to characterize the properties of antiferromagnets (Chapter IV), as well as to increase the spin pumping efficiency, acting as a spin current amplifier (Chapter II.3 and II.4).

I.1.1 Magnetic sensors

Spin valve sensors, consisting of an exchange bias based system, led to the development of advanced high performance hard disk drives [35]. A typical spin valve sensor is part of a merged read-write recording head which is mounted on a ceramic slider, located some nanometers above the recording media, as depicted in Figure 2.

The read sensor senses the small stray fields from the magnetizing regions (bits) on the recording disk spinning underneath. In its current simplest form, it consists of a nonmagnetic insulating spacer sandwiched between a ferromagnetic layer (free layer) and an exchange biased ferromagnetic/antiferromagnetic bilayer known as the hard layer. The free layer is used to read the bit of the magnetic media; it orients its magnetization along the magnetization of the stray field. The hard layer is used as the reference layer of the spin valve, meaning that its magnetization is pinned to a specific direction and does not turn under the change of the stray field. Since the tunneling probability depends on the relative orientation of the ferromagnets magnetizations, a rotation of the free layer magnetization due to stray field results in a resistance change of the sensor when a current goes through this latter.

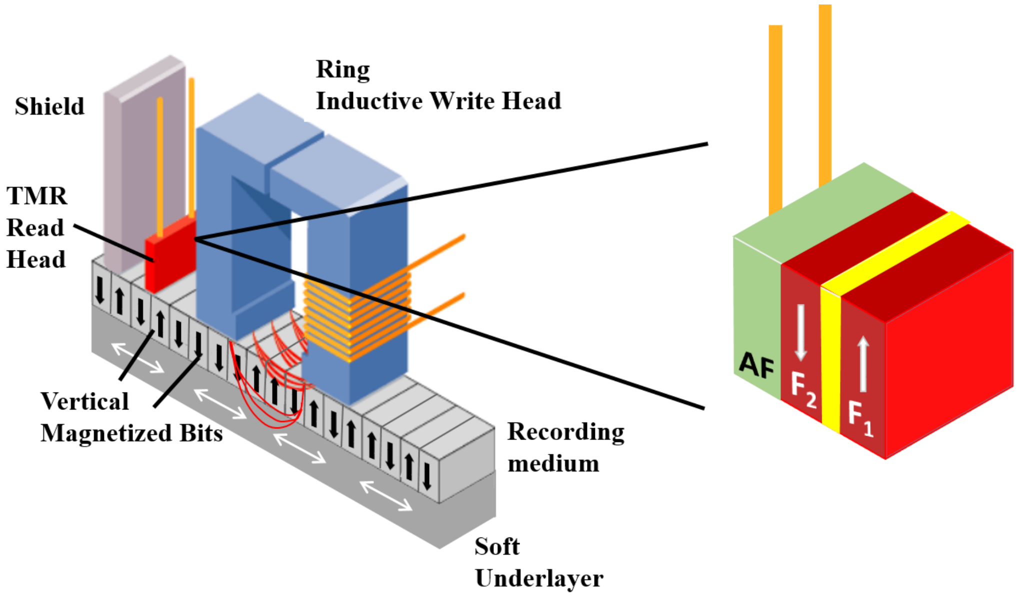

Figure 2 : Schematic view of a spin valve located in a computer hard disk drive. Adapted from Ref. [36].

I.1.2 Magnetic memories

Another application that uses a spin valve structure i.e. involving ferromagnetic/antiferromagnetic exchange bias, is the magnetic random access memory. MRAM technology provides interesting features like non-volatility, low voltage operation, large read and write endurance, fast read and write operation. It is based on magnetic storage elements. Each of these storage elements uses a spin valve device. There are a variety of MRAM structures [35,37]. Some of the early devices, the field driven MRAM, were made of horizontal and perpendicular power strips which are referred to as word and bit lines. At the intersection of the lines a spin valve is situated, see Figure 3(a). The magnetization direction of the free ferromagnetic layer is used for information storage. Consequently the writing and erasing of the data is achieved by switching the magnetization direction of the free layer. The writing of the bit is realized by a current flowing simultaneously through the desired word and bit lines. The two currents generate magnetic fields and the superposition of the two fields orients the magnetization direction of the free layer in the desired direction. The reading operation is accomplished with a low voltage applied across the desired cell and the magnetic state of the magnetic tunnel junction spin valve is derived from the measured resistance.

MRAM exists in various structures. They are categorized based on the write and read method used each time, e.g. Stoner-Wolhfarth Toggle MRAM, spin-transfer torque MRAM (STT-MRAM) and three-terminal spin-orbit torque MRAM (SOT-MRAM), which are currently receiving great attention, and thermally assisted MRAM (TA-MRAM). More details on MRAM technology and applications can be found in Ref. [37]. In the following, the relevant working principle of thermally assisted MRAM is briefly reviewed, since part of our research work presented in Chapter IV deals with the characterization and optimization of antiferromagnetic properties with the example of TA-MRAM devices.

Thermally assisted-MRAM, see Figure 3(b), promises better thermal stability and write selectivity, and less power consumption for MRAM applications [38,39]. A thermally assisted MRAM is composed of an additional antiferromagnetic layer exchange biasing the storage ferromagnetic layer, see Figure 3(d). The write selectivity is achieved by heating the magnetic cell above the storage layer blocking temperature, T_B, and cooling down in the presence of a magnetic field, see Figure 3(c). For now, we consider that the blocking temperature is the temperature above which the coupling between the ferromagnet and the antiferromagnet is lost. More about that will be discussed in Chapter IV.1. The heating is achieved by injecting a current through the magnetic tunnel junction. The storage and the reference ferromagnetic layer must be exchange biased at different blocking temperatures. The reference layer should present a high blocking temperature in order to pin the ferromagnetic layer in a fixed magnetization direction. The storage layer having a blocking temperature smaller than the writing temperature gets unpinned and its magnetization direction can be switched.

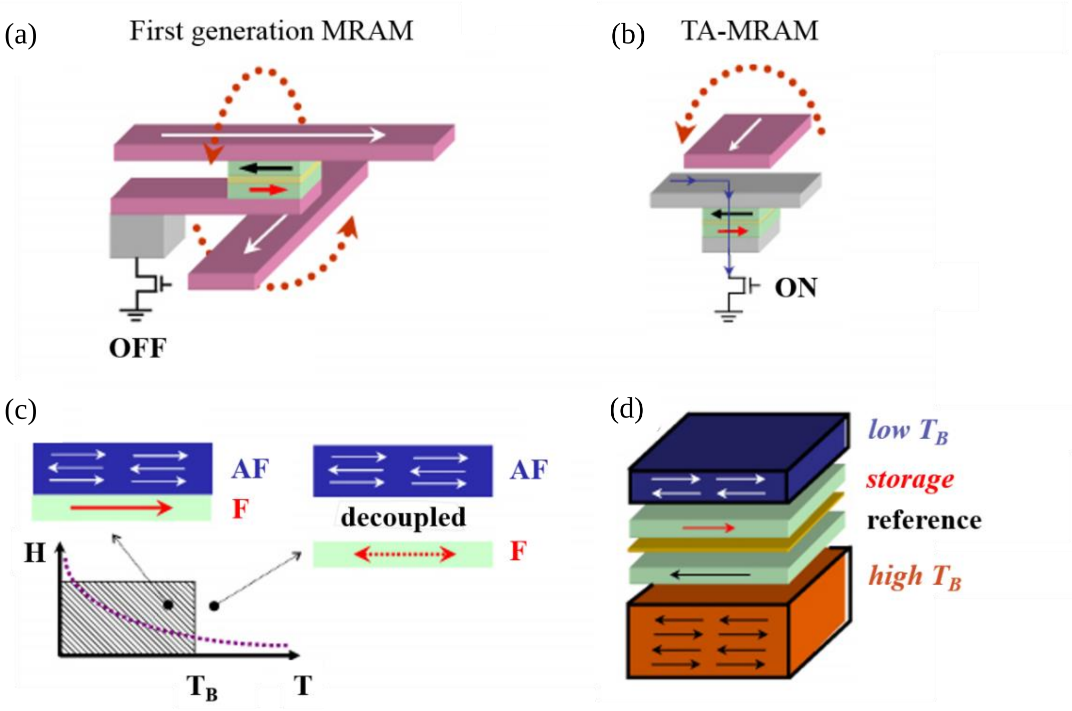

Figure 3 : Writing process in first generation (a) Toggle MRAM and (b) TA-MRAM. (c) Writing of a TA-MRAM is possible only at $T>T_B$. (d) TA-MRAM stack with both the storage and the reference layers, both pinned with antiferromagnetic materials. From Ref. [38].

I.2 Towards pure antiferromagnetic spintronic devices

Thus far the role of antiferromagnets was limited to offering stability to their ferromagnetic counterparts via the exchange bias phenomenon, thus playing a passive role for spin dependent transport.

In fact for applications, antiferromagnets present advantageous features and may eventually replace ferromagnets in the next generation of spintronic devices. We recall that, antiferromagnets show ultrafast magnetization dynamics, operating at the terahertz regime, promising higher-frequency applications beyond ferromagnetic resonance (which is typically in gigahertz range) [40]. Antiferromagnets show no net magnetic moment implying that the stored magnetic information will be immune to strong magnetic fields (up to the spin-flop transition, e.g. [24]), 'invisible' to magnetic probes and could be densely packed as antiferromagnets produce no parasitic stray fields (no cross-talks between magnetic cells in antiferromagnetic memories) [22–24], contrary to ferromagnets. The challenge faced by researchers is to find a way to efficiently control and detect the magnetic state of antiferromagnets.

In the following, we briefly introduce some of the current advances in the field of antiferromagnetic spintronics. We first address several effects proposed to read the encoded information in antiferromagnetic configurations, namely the anisotropic magnetoresistance, the tunneling anisotropic magnetoresistance and the spin Hall effect. Next, we discuss about recent studies that have demonstrated direct manipulation of antiferromagnetic order via optical and electrical means, bringing about a new dimension to the role of antiferromagnets in spintronics. Thorough descriptions of the field of antiferromagnetic spintronics can be found in recent review articles, such as in Refs [22–25].

I.2.1 Reading an antiferromagnet

Anisotropic magnetoresistance

The anisotropic magnetoresistance effect, AMR, is a result of itinerant electrons scattering at atomic orbitals. In particular, different resistance is anticipated depending on the relative orientation of magnetization with respect to the direction of the probing current direction. AMR has been extensively used in the first generation of spintronic devices (e.g. magnetic sensors) but got replaced by giant and tunnel magnetoresistance sensors as they display larger signals (~130% in compare to maximum 3% observed for AMR). Nonetheless, recent experiments have succesfully demonstrated anisotropic magnetoresistance in antiferromagnetic devices. Note that, antiferromagnets also display AMR because the effect is even in magnetization. In this direction, Marti *et al.* [19] have first demonstrated room-temperature bistable antiferromagnetic memory using FeRh, a collinerar antiferromagnet which undergoes an antiferromagnetic to ferromagnetic phase transition at 400K.

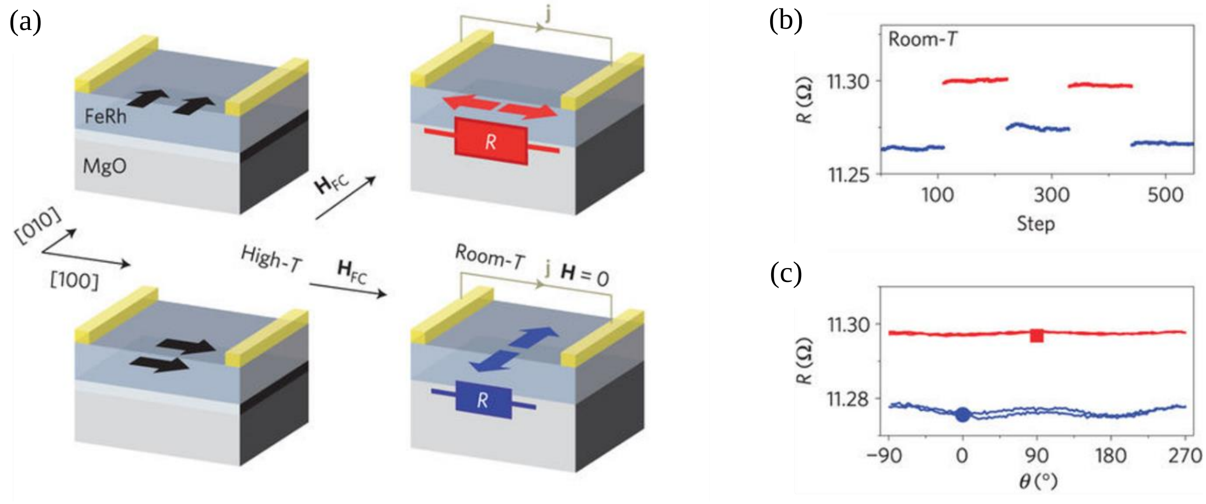

Figure 4 : (a) FeRh-based memory resistor. Different field-cooling procedures result in two distinct resistance states of FeRh. (b) Room-temperature resistance measurements after cooling the sample with field parallel to current flow (blue) and perpendicular. (c) Stability measurement of the two states while rotating a 10000 Oe magnetic field. Adapted from Ref. [19].

In their work, writing of information comprised field cooling procedures, in which the system was heated above the metamagnetic phase transition and subsequently cooled down in the presence of a magnetic field which aligned the antiferromagnetic moments in a specific direction. Figure 4(a) shows the two distinct magnetic states: one where the antiferromagnetic spins are parallel to the electrical current flow and the other one when they are perpendicular to it. The resistance measurements are depicted in Figure 4(b) where two different resistance states arise due to two different field-cooling directions.

The effect observed here is referred to as ‘non-crystalline’ AMR as it depends only on the relative change of angle of antiferromagnetic spins with respect to the flowing current. Since then, non-crystalline AMR was reported for other antiferromagnets, see Ref. [18,41–44]. Further experiments have demonstrated also ‘crystalline’ AMR in the antiferromagnetic semiconductor Sr_2IrO_4 [45].

Tunneling anisotropic magnetoresistance

Tunneling anisotropic magnetoresistance, TAMR, stems from the anisotropy of the electronic structure governed by spin-orbit coupling [46]. It is an intrinsic effect that can arise in junctions with only one magnetic electrode. A change in the magnetic configuration with respect to the probing current direction induces a measurable change in junction’s resistance. So far, this effect has been studied [47] mainly for ferromagnet-based junctions.

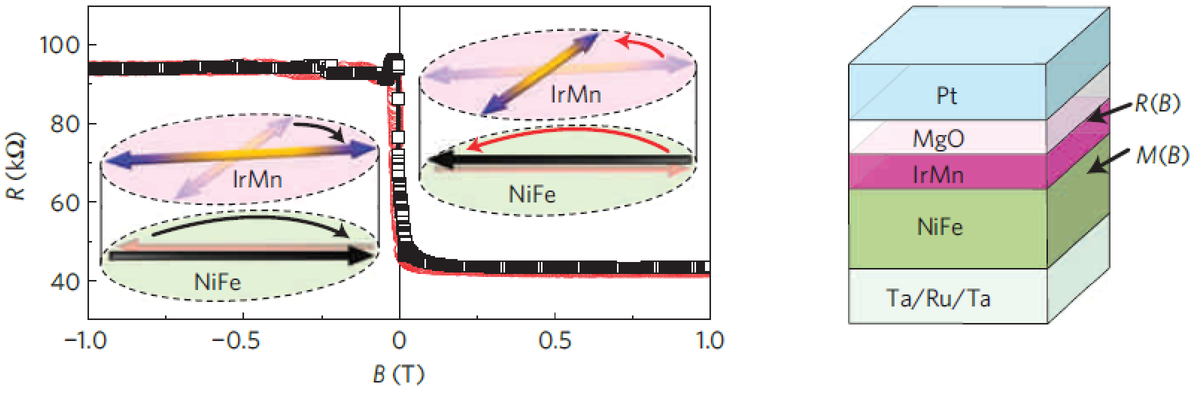

Figure 5 : Resistance versus magnetic field recorded on the depicted tunneling device, showing a large bistable antiferromagnetic TAMR signal at 4 K. From Ref. [20].

Inspired by *ab initio* studies [48] that predicted large TAMR signals in antiferromagnets, Park *et al.* [20] confirmed the theoretical predictions for metallic IrMn antiferromagnet. This bimetallic alloy meets all the criteria for strong magnetic anisotropy being composed of a heavy noble metal (large spin orbit interaction) along with a transition metal (large spontaneous moments). In their pioneering experiment, they observed an antiferromagnetic TAMR signal of 160% at 4K. The corresponding tunneling device was made of NiFe/IrMn/MgO/Pt multilayers, where NiFe/IrMn served as the magnetic electrode. In contrast to conventional tunnel junction stacks, IrMn was in contact with MgO governing the tunneling transport. Being exchange biased to NiFe, antiferromagnetic spins were able to rotate via the exchange-spring effect in such a way so as to achieve the largest possible tunnel anisotropic magnetoresistance signal, see Figure 5. This work inspired further investigations on antiferromagnetic TAMR which led to the observation of the TAMR effect at room temperature [49,50], despite the small signals of around 0.1%.

Spin Hall effect

The new spintronic devices are supposed to include or ‘exclusively’ use the spin degree of freedom of electrons in the form of pure spin currents. This asks for new materials that allow for generation, control and detection of such spin currents. Different methods have been proposed in the literature to generate spin currents including the spin Hall effect [51,52] (discussed in Chapter III), spin pumping [53,54] (addressed in Chapter II) and spin Seebeck effect [55]. To comply with the existing information technology, the detection of spin currents calls for relativistic effects which can convert the spin into charge current. As a matter of fact, the inverse process of spin Hall effect allows for detection of spin currents in materials with strong spin-orbit coupling [56]. This effect was originally demonstrated in nonmagnetic materials [54] but not long ago was also observed in antiferromagnetic materials [26,29,57], highlighting the potential of antiferromagnets to be efficient spin current detectors.

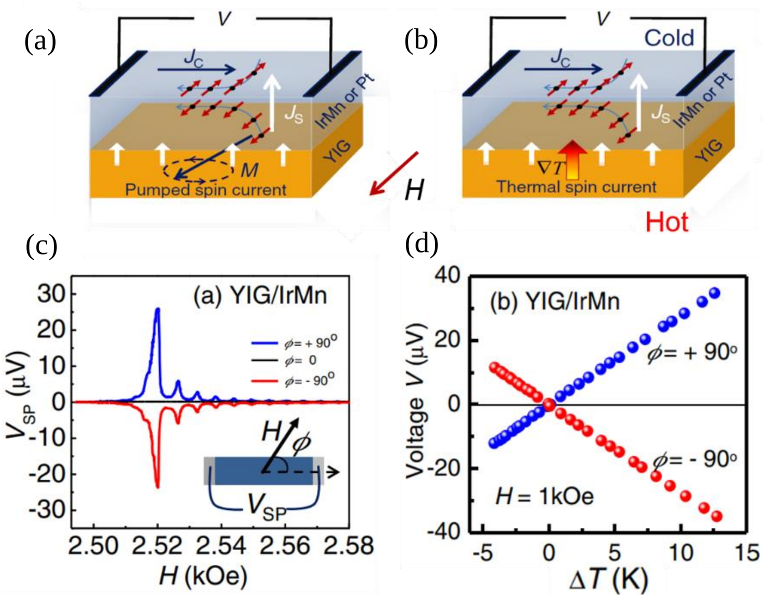

Figure 6 : Schematic illustration of the generated spin current via: (a) spin pumping and (b) spin Seebeck effect. (c) and (d) show the generated voltage in IrMn as a function of the magnetic field and the temperature difference across the stack, respectively. Adapted from Ref. [26].

Here, we present briefly the pioneering experimental results of spin Hall effect in metallic IrMn, as illustrated by Mendes *et al.*[26]. In this work, spin current generation was achieved via spin pumping and thermally via the spin Seebeck effect, see Figure 6(a) and (b), respectively. The generated spin current flowed from the ferromagnetic YIG, towards the IrMn layer and subsequently got converted into charge current in the antiferromagnet. Figure 6(c) and (d) shows the generated voltage as a function of the bias magnetic field and the temperature difference across the stack, respectively. In fact, IrMn demonstrated a strong conversion efficiency which was comparable to that of Platinum.

These results triggered a series of studies where various antiferromagnets were tested as efficient spin current detectors, using various methods [29,58–61]. Notably, in exchange biased systems antiferromagnets act also as efficient spin current transmitters, as demonstrated in Refs. [58,62–66]. The exchange coupling combined to the spin Hall effect in the antiferromagnet provides a viable solution for the deterministic switching of a ferromagnet with out of plane anisotropy, in zero applied magnetic field [62–66].

I.2.2 Writing an antiferromagnet

So far, we have discussed about various methods to read the information encoded in antiferromagnets. Next, we present ways of writing the magnetic information in antiferromagnets. First, we talk about how electromagnetic radiation can be used to control and detect spin order in antiferromagnets, and then we explain how antiferromagnets can be manipulated electrically. The latter led to the recent demonstration of a purely antiferromagnetic device [18].

Antiferromagnetic opto-spintronics

It was shown that the antiferromagnetic order can be manipulated and detected optically [67,68]. More specifically, it was demonstrated that canted antiferromagnets (i.e. weak ferromagnets) can be reoriented upon optical excitation due to inertial dynamics, see Figure 7. In fact, a laser-generated magnetic field (pulse of 100 fs) gives the necessary momentum to spins to overcome the potential barrier and switch their magnetic orientation, long after the action of the stimulus [69]. This inertia-based mechanism of spin reorientation could be used to write the magnetic information in antiferromagnets, using extremely short magnetic field pulses. The latter observations triggered a series of experimental and theoretical works on antiferromagnetic opto-spintronics, ranging from optical detection methods [69,70] to terahertz emission [71], ultra-fast magnetization switching [67,72] and time-resolved spin-dynamic measurements [67,73]. Interested readers are encouraged to complement their knowledge by consulting the review article by Nemec *et al.* [40] and by Baltz *et al.* [24].

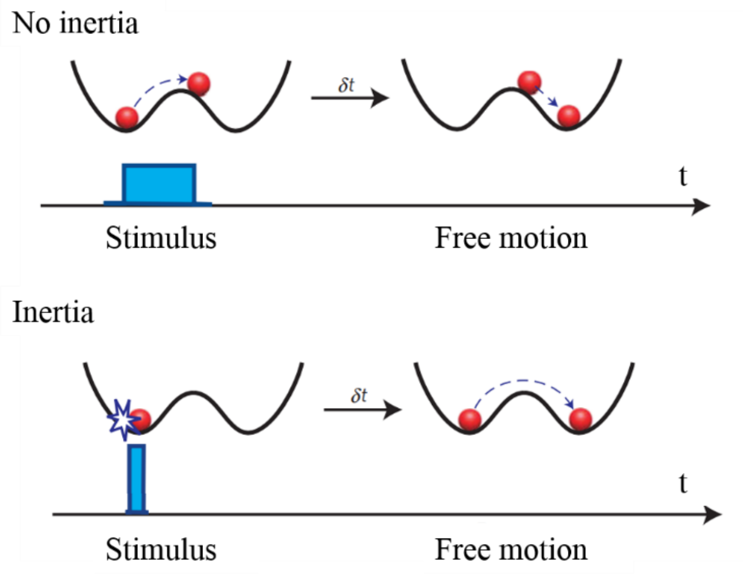

Figure 7 : Non-inertial and inertial spin reorientation, related to ferromagnetic and antiferromagnetic dynamics. From Ref. [69].

Inverse spin galvanic torque

In 2014, Železný *et al.* [17] predicted theoretically the electrical current-induced antiferromagnetic manipulation via Néel-spin-orbit torques, which was further demonstrated experimentally by Wadley *et al.* [18], at ambient conditions. It was observed for semi-metallic CuMnAs antiferromagnet, whose full lattice shows an inversion symmetry, as illustrated in Figure 8(a). The latter structure consists of two sublattices, formed by Mn atoms, which individually have broken inversion symmetry and form inversion partners [17].

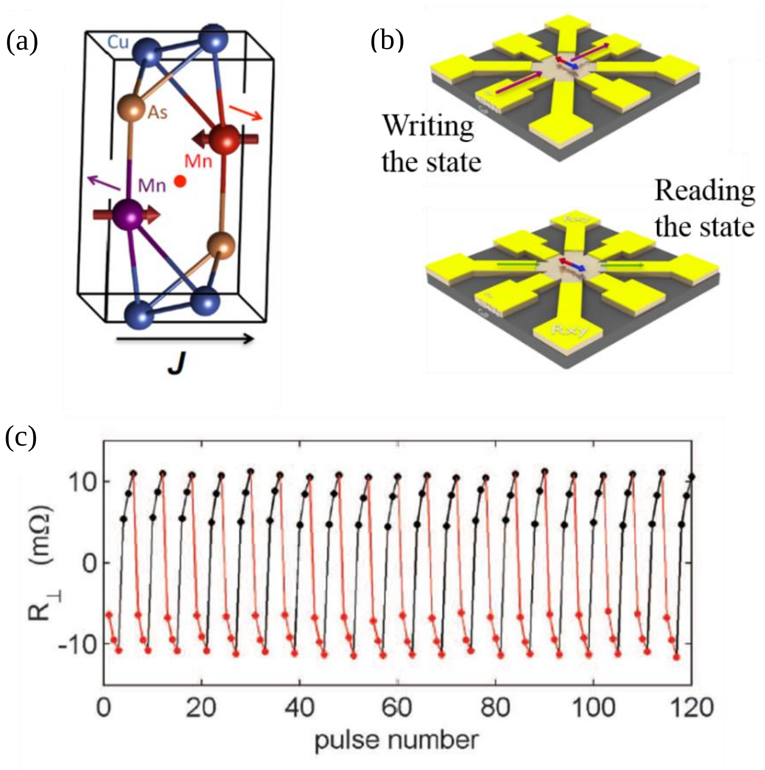

Figure 8 : (a) CuMnAs crystallographic and spin structure. (b) current-induced writing with the inverse spin galvanic effect (top) and AMR(planar Hall effect)-assisted reading (bottom) (c) Resistance measurements showing the stability of the two memory states, corresponding two distinct antiferromagnetic configurations, where the antiferromagnetic order points along 0 and 90°. Adapted from Ref. [18].

The charge current induces a nonequilibrium spin polarization in the bulk of the material. Basically the electrical current induces nonequilibrium fields that alternate in sign (staggered fields) and apply a torque on each magnetic sublattice which eventually rotates the antiferromagnetic spins by 90 degrees, with respect to the flowing current. In such a way the information is encoded in the antiferromagnetic configuration via electrical means (see Figure 8(b), top sketch). The readout is achieved also electrically through the planar Hall effect, PHE, which is intimately related to the anisotropic magnetoresistance effect. This effect has been also demonstrated recently in Mn_2Au [74,75]. Notably, Roy *et al.* [76] have also computationally shown for the very same material robust picosecond writing, with minimal risk of overshoot. In their work, they examined the switching process of the antiferromagnet taking into account the impact of spin-orbit field strength, current pulse properties, and damping. Overall, these studies emphasize the possibility of switching the antiferromagnetic order by current injection.

Summary

The designing of antiferromagnet-based spintronic devices involve two approaches. The first approach targets at boosting the functionalities of ferromagnets, via the exchange bias phenomenon. The second effort, which is more radical, focuses on finding novel ways of reading and writing the magnetic information in purely antiferromagnetic spintronic devices. In this direction, one of the proposed solutions is to exclusively use the spin degree of freedom of electrons in the form of pure spin currents. Currently, considerable efforts have been invested towards more efficient spin current generation, transmission and detection in antiferromagnets. Nonetheless, there still remain significant gaps in our knowledge concerning the antiferromagnetic spin dependent transport properties, as some of the basic parameters, such as the interfacial spin mixing conductance, the spin penetration length as well as the Néel temperature, still need further investigation. Central to our work is to study and determine some of these characteristic parameters.

II. Spin injection and transmission in antiferromagnets

In this chapter we consider spin injection and transmission in both metallic and insulating antiferromagnets. The ferromagnetic resonance via the spin pumping technique is well suited for this purpose, as it probes magnetization dynamics and gives information on the dissipation of energy, including dissipation due to spin absorption in a neighboring layer, for example in an antiferromagnet. Section II.1 provides the necessary conceptual framework to our work and discusses theoretical issues related to magnetization dynamics and relaxation (intrinsic and extrinsic). Subsequently, a brief description of the experimental procedure is addressed and is dedicated to the ferromagnetic resonance technique and the extraction of the corresponding parameters and in particular of the extrinsic relaxation parameters. Sections II.2 to II.5 are devoted to the experimental results. Our experiments have revealed a novel enhanced Gilbert damping associated to the fluctuating magnetic order of the antiferromagnet under investigation. The latter opens new ways towards more efficient spin pumping, while providing at the same time a versatile method to probe magnetic phase transitions of ultrathin films.

II.1 Introduction to magnetic relaxation and spin pumping

II.1.1 Magnetization dynamics

Magnetization dynamics in thin ferromagnetic films are well described by the Landau-Lifshitz-Gilbert (LLG) equation [77,78], which accounts for damped precessional motion. Let us first consider the model proposed by Landau and Lifshitz (LL) [79]. According to this model, when the magnetization, **M** is subjected to an effective magnetic field, $\mathbf{H_{eff}}$ which exerts a field-torque, it precesses with a constant cone angle around the field axis, as depicted in Figure 9(a). This leads to a classical equation of motion for an undamped magnetization:

$$\frac{d}{dt}\boldsymbol{M} = -\gamma\left(\boldsymbol{M} \times \boldsymbol{H_{eff}}\right) \qquad \text{(Eq. II.1).}$$

The effective field in the Eq. II.1 consists of the Zeeman contribution due to the applied magnetic field, the exchange interaction field, the demagnetizing field and the anisotropy contribution.

An additional damping-torque term was later included to the LL model in order to explain the experimental observations. The combination of field- and damping- torques pushes the magnetization into a spiral motion until it aligns with the field direction. This is described by the following equation:

$$\frac{d}{dt}\boldsymbol{M} = -\gamma\left(\boldsymbol{M} \times \boldsymbol{H_{eff}}\right) - \frac{\lambda}{M_S^2}\boldsymbol{M} \times \left(\boldsymbol{M} \times \boldsymbol{H_{eff}}\right) \qquad \text{(Eq. II.2),}$$

where λ is a phenomenological damping constant specific to the material/stack, that will be detailed in the next paragraph.

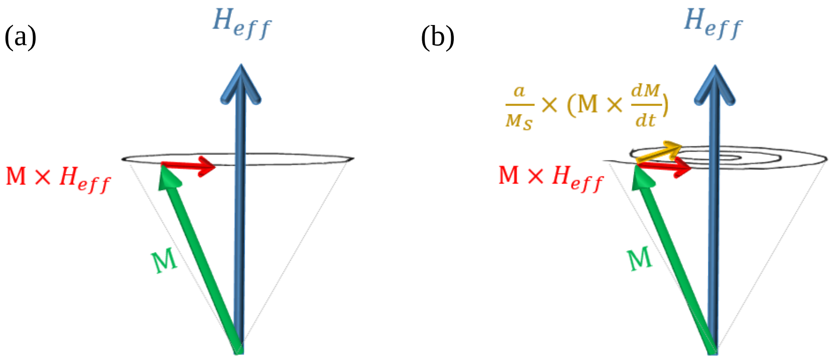

Figure 9 : Schematic illustration of (a) Landau-Lifshitz and (b) Landau-Lifshitz-Gilbert (LLG) equation.

However, both theory and experiments indicated that the damping parameter takes different values depending on the magnitude of the magnetic field, the response frequency as well as the magnetization angle with respect to the field direction. In 1955 Gilbert [77] described damping as a ‘viscous’ force proportional to the time derivative of the magnetization. In this way, the equation of motion governing magnetization precession took the following form, named as the LLG equation:

$$\frac{d}{dt}\boldsymbol{M} = -\gamma\left(\boldsymbol{M}\times\boldsymbol{H}_{\boldsymbol{eff}}\right) + \frac{\boldsymbol{\alpha}}{M_s}\left(\boldsymbol{M}\times\frac{d\boldsymbol{M}}{dt}\right) \qquad \text{(Eq. II.3).}$$

The first term in the LLG equation refers to the uniform magnetization precession about the effective field, with conservative dynamics. The second term corresponds to the phenomenological Gilbert damping term, α, where the magnetization undergoes a damped precessional movement towards the effective field, see Figure 9(b).

The Gilbert damping describes the relaxation of magnetization. Due to its big technological impact (e.g. for magnetic memories and oscillators) it has received much attention over the last decades. Despite its simplified implementation in the LLG equation, there is still considerable and rich physics with regard to its physical origin. In this subsection we will try to clarify the main physical concepts that contribute to the Gilbert damping.

It should be emphasized that Gilbert damping is highly sample dependent. This means that it suffers from both intrinsic and extrinsic contributions to the material system. The intrinsic damping is related to unavoidable contributions which eventually lead to the dissipation of energy. On the other hand, the contributions that could be prevented, such as the ones that come from the measurement geometry, sample structure and properties are considered to be extrinsic.

II.1.2 Relaxation mechanisms

II.1.2.1 Intrinsic mechanisms

There are three major physical concepts that may contribute to the intrinsic Gilbert damping: magnon-phonon interactions, magnon-electron interactions and eddy currents. In the following we will briefly examine the aforementioned mechanisms.

Magnon-phonon interactions

The presence of lattice vibrations at finite temperature are described as phonons in quantum mechanics (elementary vibrational motion). Similarly, elementary excitations of the spin structure in a lattice are described as magnons. In a magnetic film, the magnon-phonon interactions contribute to magnetic damping. This is sometimes referred to as the phonon drag: a precessing spin exerts periodically attractive or repulsive forces to the neighbor atoms as a result of the direct coupling between the spins, which unavoidably leads to phonons. The reciprocal phenomenon involves decoherence of the spin waves due to the propagating phonons, which eventually leads to dissipation of energy.

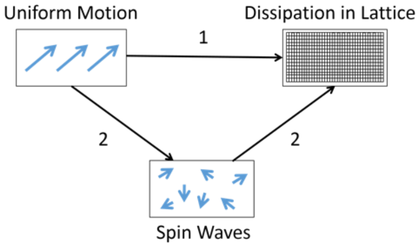

Figure 10 : The two possible dissipation processes of the uniform motion as explained by Suhl. From Ref. [80].

Suhl [80] investigated the interaction between the uniform magnetization mode and the lattice motions, see Figure 10 and concluded in the following equation in an effort to quantify the Gilbert phonon damping, α^{ph}:

$$\alpha^{ph} = 2\eta(\gamma \frac{B_2(1+\nu)}{E})^2 \qquad \text{(Eq. II.4),}$$

where E constitutes the Young’s modulus, η the phonon viscosity, B_2 the magnetoelastic shear constant, ν the Poisson ratio and γ the gyromagnetic ratio. According to experimental results [81,82], the Gilbert phonon damping takes very small values, 30 times smaller (around 10^{-4}) than typical intrinsic damping for *3d* transition metals. It is therefore usually neglected for such materials.

Magnon-electron interactions

The most important intrinsic contribution to magnetic damping and especially in the case of metallic ferromagnets, refers to the dissipation of energy through interactions between magnons and itinerant conduction electrons. The latter justifies why metallic ferromagnets present higher values of Gilbert damping compared to their insulating counterparts. Two different mechanisms were used to explain magnon scattering with itinerant electrons. The first mechanism relies on the *s-d* exchange interaction, as proposed by Heinrich *et al.* [83] and the other mechanism is related to spin-orbit interactions and is based on the works of Kambersky *et al.* [84] and Gilmore *et al.* [85]. The difference between the two approaches lies on whether the incoherent scattering of electron-hole pair excitations by magnons and phonons gives rise to spin-flip or to non-spin-flip excitations.

Heinrich *et al.* showed that the intrinsic damping can be treated by using the *s*-*d* exchange interaction: the interaction between the *d*-localized moments and the *s* itinerant electrons. In this process, magnons and itinerant electrons are coherently scattered, which yields to creation and annihilation of electron-hole pairs, as presented in Figure 11. Consequently, the itinerant electron flips its spin so as to conserve angular momentum. A second three particle scattering process will then take place and eventually lead to the emission of a magnon. Magnetic relaxation is expected only when the spin flip hole-electron pairs scatter incoherently by thermally excited phonons or magnons.

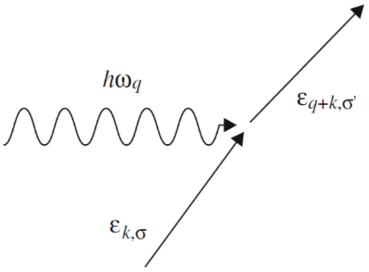

Figure 11 : Schematic diagram of the spin-flip excitation where the magnon collides with an itinerant electron with energy $\varepsilon_{k,\sigma}$ (momentum k and spin orientation σ) and creates an itinerant electron with energy $\varepsilon_{q+k,\sigma'}$ (momentum k+q and spin orientation σ′) [83].

The *s*-*d* model predicts Gilbert damping dependence on the spin-flip lifetime, τ_{sf} as follows:

$$\alpha^{el} = \frac{\chi_{Pauli}}{\gamma M_s \tau_{sf}} \quad \text{(Eq. II.5),}$$

where M_s corresponds to the saturation magnetization and χ_{Pauli} to Pauli's susceptibility for the itinerant electrons. Eq. II.5 describes the behavior of Gilbert damping at low temperatures as conductivity-like, since it increases with decreasing temperature, just like the electronic relaxation time. At high temperature a resistivity-like behavior is expected instead, as will be discussed in the following subsection.

Having examined the approach by Heinrich *et al.*, we will now focus on Kambersky's model [84]. This model describes the intrinsic Gilbert damping in terms of spin-orbit interaction Hamiltonian. No spin flip scattering events are involved in this process. Kambersky took into account the effect of precessing magnetization on the Fermi surface. He pointed out that the Fermi surface undergoes periodic transformations due to the change in magnetization direction. This process changes the energy of the electronic states: part of the occupied states jumps above the Fermi level and part of the unoccupied states stay below the Fermi level. The creation of electron-hole pairs near the Fermi level is therefore inevitable. Note that the repopulation of the energy levels with the magnetization precession exists only for a certain timescale, the phenomenological relaxation time τ, before it relaxes towards the instantaneous equilibrium through electron-phonon scattering processes. Basically, the phase lag between the Fermi surface distortions and the magnetization precession is a dissipative process which leads to magnetic damping. Based on the nature of the transitions, it is possible to distinguish between intraband transitions and interband transitions (which are associated with energy gaps).

The temperature dependence of the magnetic damping depends on the nature of the corresponding transitions. For intraband transitions the magnetic damping increases linearly with the relaxation time and follows a conductivity-like behavior at low temperatures. On the other hand, interband transitions dominate at high temperatures, where the Gilbert damping is roughly inversely proportional to the electron relaxation time which results in a resistivity-like behavior [85]. This behavior is typical for ferromagnetic 3*d* transition metals. We will show an experimental measurement of that in section II.1.3, Figure 22(c).

<u>Eddy currents in ferromagnetic films</u>

The magnetization relaxation by eddy currents is another possible damping mechanism. The conduction electrons can effectively interact with the excitation microwave field, giving rise to additional damping. To calculate their impact on the magnetization relaxation, one has to solve the LLG and Maxwell equations simultaneously:

$$\alpha^{eddy} = \frac{1}{6}\left(\frac{4\pi}{c}\right) 2\sigma (M_s \gamma t_F)^2 \qquad \text{(Eq. II.6)},$$

where σ is the film conductivity, c the light velocity and $\mathrm{t_F}$ the film thickness. Eddy currents contribution to Gilbert damping becomes important in thick ferromagnetic films only, when the film thickness is the same or bigger than the skin depth, δ.

It should be noted here that α^{eddy} depends strongly on the material. For instance, in the case of Fe this contribution is comparable to the intrinsic damping only for a film thickness of 70 nm, as it takes values of around 10^{-3} [81]. For Permalloy, which is at the focus of our studies, α^{eddy} needs to be taken into account only for thicknesses above 100 nm. In the case where the ferromagnet is surrounded by metallic films, there might be an extra contribution to damping originating from eddy currents flowing in the metallic neighbors. This case will be presented in the next section (II.1.2.2), as well as in section II.5, where experimental measurements of this kind will be discussed.

II.1.2.2 Extrinsic mechanisms

So far we have talked about intrinsic dissipative processes which contribution cannot be avoided. In this section, we shall discuss about the extrinsic mechanisms that contribute to the magnetization relaxation. They are related to structural and interfacial defects, inhomogeneity of the magnetic properties or to the presence of neighboring layers. Different mechanisms can account for extrinsic damping, such as two-magnon scattering, slow-relaxing impurities, spatial inhomogeneity of the magnetic parameters, eddy currents in neighboring metals and spin pumping by neighboring layers. The following paragraphs will be devoted to the description of the abovementioned dissipative processes.

Two-magnon scattering

The two-magnon scattering mechanism describes the scattering of spin waves with zero wave vector (uniform magnetization precession) into the manifold of degenerate modes by defects [86]. The latter is viewed as a dephasing contribution to magnetization relaxation. Structural and crystal defects, as well as boundaries, can all act as scattering centers and give rise to the two-magnon contribution to damping. Arias and Mills [87,88] developed an expression accounting for magnon scattering by surface and interface defects in ultrathin films given by [89]:

$$\alpha^{tms} \propto \Gamma \, sin^{-1}\sqrt{\frac{\sqrt{\omega^2+{\omega_0}^2}-\omega_0/2}{\sqrt{\omega^2+{\omega_0}^2}+\omega_0/2}} \qquad \text{(Eq. II.7),}$$

where ω is the resonant frequency, $\omega_0=4\pi\gamma M_{eff}$ and Γ is a prefactor that gives the strength of two-magnon scattering. Their theory infers that the two-magnon scattering contribution is significantly important in films magnetized in the film plane, whereas it is absent when the magnetic field is applied perpendicular to the film plane, since in this case no spin waves degenerate with uniform magnetization precession exist. Additionally, they pointed out the strong dependence of the two-magnon scattering strength on the interfacial roughness and the scaling of it with the squared of the film thickness.

It is noteworthy here that the two-magnon scattering mechanism is not characterized as viscous Gilbert-like damping since it is not proportional to the resonance frequency. We will further present evidence that two-magnon scattering is not the dominant contribution in our experiments, see section II.5.

Slow-relaxer

The slow-relaxing impurity model was initially proposed to explain the extra relaxation in magnetization precession in rare earth doped YIG samples [90–92]. It was further used to explain the experimental results of Gilbert damping in the case of exchange bias systems [93–96] where broadening of the resonance field and resonance linewidth was observed. This behavior was attributed to slow relaxation due to thermal reversal of antiferromagnetic grains, with an analogous behavior displayed by superparamagnetic ferromagnetic grains. In the initial model, the anisotropic exchange coupling between the 4*f* magnetic moments of impurities and the 3*d* magnetic moments of the host magnetization plays a key role. More specifically, it results in the modulation of 4*f* exchange splitting during the precession of 3*d* magnetic moments. Subsequently, the population of the 4*f* levels tries to follow the temporal changes of magnetization but instead it is delayed by the impurities spin lattice relaxation time, τ. In an effort to reach thermal equilibrium, moments will undergo transitions between the split 4*f* states which in turn will lead to a locally fluctuating field acting on the precessing 3*d* moments.

This translates into extra dissipation of the magnetization relaxation and is expressed by the following equation:

$$\alpha^{slow-relaxer} \propto \frac{\omega\tau}{1+(\omega\tau)^2} \qquad \text{(Eq. II.8),}$$

where ω is the resonant frequency. We shall discuss later in section II.4.3 more about the spin-relaxing impurity model, specific to our experimental results. We will further prove that slow-relaxation mechanisms are not the dominant contribution to our findings.

Magnetic inhomogeneities

Magnetic inhomogeneities relate to the local variations of the effective field due to different values of surface anisotropies, e.g. due to roughness and inhomogeneous interdiffusion of species. As can be seen from Figure 12, the interfacial roughness gives rise to different inhomogeneous magnetostatic fields at different sample locations, where the corresponding spins precess on different trajectories. This process is associated with the decoherence of the uniform precession mode and consequently with damping [97]. In the same context, Tserkovnyak and coworkers [98] talked about the effect of weak nonuniform transverse spin-wave excitations on Gilbert damping , which was formulated mathematically as follows:

$$\alpha^{inhom.} \propto \frac{\hbar\gamma^2 g_{eff}^{\uparrow\downarrow}/4\pi V}{1+[4\lambda/\lambda_{sw} tanh(2\pi t_F/\lambda_{sw})]^{-1}} \qquad \text{(Eq. II.9),}$$

where $g_{eff}^{\uparrow\downarrow}$ is the effective spin mixing conductance (explained later in this section), λ is the transport mean free path in the ferromagnetic film, λ_{sw} the wavelength of excitation and V the volume of the ferromagnet.

In section II.1.3 we will show how to "isolate" experimentally the contribution of magnetic inhomogeneities to Gilbert damping. The potential impact of roughness on damping will later be discussed in the framework of the experimental results presented in section II.5.

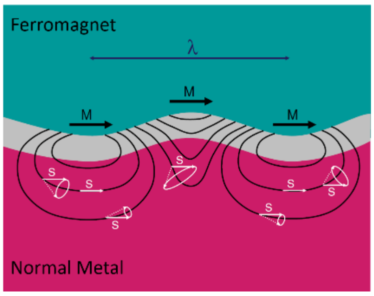

Figure 12 : The effect of interface roughness on the uniform magnetization precession. Adapted from Ref. [97].

Eddy currents in metallic films adjacent to the ferromagnetic layer

In section II.2.1.1 we discussed about eddy currents in ferromagnetic layers and their contribution to the intrinsic damping. Recent studies [99,100] have shown that in specific geometrical configuration, eddy currents generated in a nonmagnetic material, adjacent to ferromagnetic layer, lead to extra damping, see Figure 13. In fact, the oscillation of the ferromagnet magnetization generates a radiofrequency magnetic field that creates extrinsic eddy currents in the surrounding metallic layers. In return, the eddy currents generate a feedback radiofrequency magnetic field that contributes to the dephasing of the magnetization dynamics of the ferromagnet. Rather than acting on the damping itself, this dephasing translates into an asymmetry of the resonance lineshape of the ferromagnet. We shall see experimental findings of this kind in section II.5.

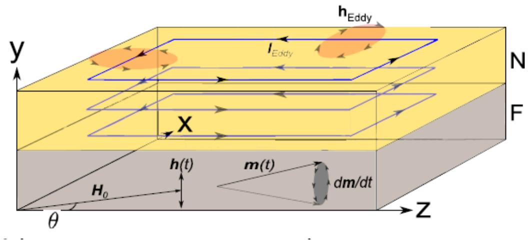

Figure 13 : Schematic illustration of the sample geometry showing the generated eddy currents in the nonmagnetic layer, adjacent to ferromagnet. From Ref. [99].

Spin pumping

In general, structures in which the ferromagnet is sandwiched between different layers give rise to an additional nonlocal damping, as pointed out by Mizukami et coworkers [53]. These authors observed a deviation of the ferromagnetic NiFe experimental damping with regard to the calculation values using the LLG equation, dependent on the nature of the adjacent layer. More specifically, the deviation was found to be more pronounced in the case when the NiFe was in contact with heavy metals. The enhanced damping displayed $1/t_{NiFe}$ dependence, pointing out the existence of an interfacial process. Tserkovnyak et coworkers [98,101,102] later described the phenomenon in terms of adiabatic pumping of spins from the ferromagnetic layer towards the adjacent material. The mechanism was named as the spin pumping effect.

For a visual representation of the spin pumping effect the reader is referred to Figure 14, where a bilayer system is considered. A chemical potential imbalance is induced at the interface due to the different magnetic nature of the two materials. This imbalance creates a spin accumulation, i.e. an out of equilibrium distribution of spins. In the case of static magnetization this translates into a d.c. chemical imbalance in the nonmagnetic metal. Though as shown in Figure 14, the magnetization is not static, instead it is precessing: the magnetization is switched back and forth as it is subjected to an oscillating magnetic field. As a result the ferromagnetic bands instantaneously will shift in energy due to the exchange splitting. In order to return back to equilibrium there has to be a spin transfer from one band to the other (spin relaxation process) [103]. Given the circumstances the spin relaxation can occur in the normal metal by the emission of an a.c. spin current, $\boldsymbol{I_s^{pump}}$. To put it simply, the normal metal acts as a spin sink to the pumped spin current. The spin current carries spin angular momentum flowing perpendicular to the interface with a polarization direction pointing towards $\boldsymbol{M} \times \frac{d\boldsymbol{M}}{dt}$.

Depending on the spin dependent properties of the spin sink, the spin current will either relax by spin-flip scattering giving rise to the nonlocal damping or it will flow back to the precessing ferromagnet, $\boldsymbol{I_s^{back}}$ in a way that $\boldsymbol{I_s^{pump}} = \boldsymbol{I_s^{back}}$. The former refers to perfect spin sinks and the latter to poor spin sinks.

The overall pumped spin current can be derived as [101]:

$$\boldsymbol{I_S^{pump}} = \frac{\hbar}{4\pi} \mathrm{g}_{\mathrm{eff}}^{\uparrow\downarrow} \boldsymbol{M} \times \frac{d\boldsymbol{M}}{dt} \qquad \text{(Eq. II.10),}$$

where $\mathrm{g}_{\mathrm{eff}}^{\uparrow\downarrow}$ refers to the dimensionless effective spin mixing conductance, which describes the spin angular momentum transfer efficiency from the ferromagnet to the nonmagnetic layer.

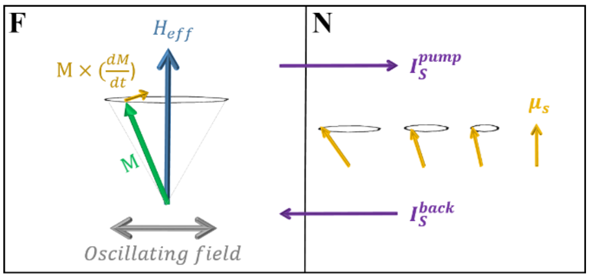

Figure 14 : Schematic illustration of the spin pumping effect in a ferromagnet(F)-normal metal(N) bilayer system.

The absorption of spin current leads to the permanent loss of spin angular momentum out of the precessing ferromagnet which can be seen as a damping-like contribution acting on the magnetization. This extrinsic damping contribution can be derived from I_S^{pump}, and is given by [101]:

$$\alpha^p = g_{eff}^{\uparrow\downarrow} \frac{\gamma\hbar}{4\pi M_S V} \qquad \text{(Eq. II.11).}$$

This additional nonlocal damping is Gilbert like and follows a linear dependence with the ferromagnet thickness 1/t_F. It contains the physics of the spin absorption/transmission at the various interfaces and within the materials adjacent to the ferromagnet.

II.1.3 Typical experimental procedure

Thus far, we have seen that in physical systems the out-of-equilibrium dynamics are governed by numerous parameters. In practice, magnetization dynamics can be coherently controlled by external means so as to reach resonance conditions. Thus, resonance experiments are very powerful to characterize the physical systems to an extent which depends on how well it is possible to disentangle the effects associated with the magnetization dynamics. In this section, we will discuss on how to extract some of the physical properties related to the ferromagnet, such as saturation magnetization, anisotropy and eventually Gilbert damping. To quantify the magnetization relaxation of a system, a number of experimental techniques exist, such as:

brillouin light scattering (BLS) [104], ferromagnetic resonance (FMR) [105], time resolved neutron scattering [106], X-ray magnetic circular dichroism [107] and magneto-optical Kerr effect magnetometry [108]. Among those, BLS and FMR can probe small-angle magnetization dynamics. For our studies we used the ferromagnetic resonance technique.

The aim of our work is to study spin injection, absorption and detection in antiferromagnets. To this end, the general idea here is to generate the spin pumping effect and to further extract the extrinsic contribution to ferromagnetic damping related to spin-dependent mechanisms in the adjacent antiferromagnet. Note that, in our case the ferromagnet is not the main object of interest since its contribution is limited to probe the physics of spin relaxation in the antiferromagnets. Most frequently, magnetoresistive and dynamic experiments are used to study the parameters controlling spin-dependent mechanisms. These experiments are commonly applied to ferromagnetic layers, but they are not ideal for antiferromagnetic films, which display low magnetoresistive signals and require very high frequency (THz) to induce dynamic excitation. For this reason, FMR and spin pumping is more suitable to study spin-dependent transport in antiferromagnets.

Experimental setups.

In a conventional FMR experiment, the sample is subjected to a static (bias) magnetic field ($\mathbf{H}$) that exerts a torque over the magnetization, $\mathbf{M}$, yielding to a precessional motion around the axis of the effective field, $\boldsymbol{H_{eff}}$. In order to maintain the precession a transverse rf field ($\mathbf{h_{rf}}$) is applied perpendicular to the static field and counters the effect of damping. The resonance condition is satisfied when the frequency of the $\mathbf{h_{rf}}$ field matches the natural resonance frequency, $\omega_{res}/(2\pi)$, of the ferromagnetic thin film. Since the resonance frequency is determined by the effective magnetic field, one can either sweep the frequency at a fixed field or keep the frequency fixed and sweep the magnetic field, like in our case. Here, we used two FMR setups: a cavity based spectrometer (fixed frequency, variable temperature) (see Figure 15(a)) and a coplanar waveguide based spectrometer (variable frequency, fixed temperature) (see Figure 15(b)). It is noteworthy that the data presented in Figure 22(b) were obtained by C. Cheng and W. E. Bailey from the Columbia University of New York using a third coplanar waveguide based spectrometer operating at cryogenic temperatures.

The cavity-based FMR experiments were conducted using a continuous wave electron paramagnetic resonance spectrometer owned by the CEA/INAC/SYMMES laboratory (Serge Gambarelli and Vincent Maurel) and operating at 9.6 GHz fitted with a dual-mode rectangular cavity. The system is based on a helium cryostat that can operate in the temperature range of 4 to 300K. Figure 15(a) shows the key components of the cavity-based FMR, used in our experiments, which consists of: the cavity, the microwave bridge, the gaussmeter, the electromagnet and the detection diode for signal process [105]. We also use a lock-in detection (the dc applied field is modulated by a small rf field created by Helmholtz modulation coils, (few Oe, 201 Hz)), in order to increase the signal to noise ratio. The cavity is impedance matched to the waveguide in order to ensure maximal coupling. The detector diode placed at the end of the cavity records the microwaves. When the ferromagnetic resonance condition is satisfied, a change in the cavity impedance is observed. As a result microwaves are reflected and detected by the detection diode, giving rise to the FMR signal. Figure 15(b) is a schematic illustration of the coplanar waveguide broadband FMR spectrometer [109] used in our experiments at SPINTEC. This setup was built in 2011 by A. Ghosh, U. Ebels and W. E. Bailey on the occasion of the PhD thesis work of A. Ghosh [109]. The spectrometer operates at 300K. The microwave magnetic field of variable frequencies (4 to 24 GHz) is generated by a vector network analyzer (VNA) and is transmitted through a double ground plane coplanar waveguide (CPW). Like in the previous setup, we use a lock-in detection with a small rf field created by the Helmholtz coils shown in the Figure 15(b). The resulting signal as received from the lock-in amplifier is a derivative of the absorbed power versus the applied field. The conversion of the transmitted signal into voltage is done using a Schottky diode.

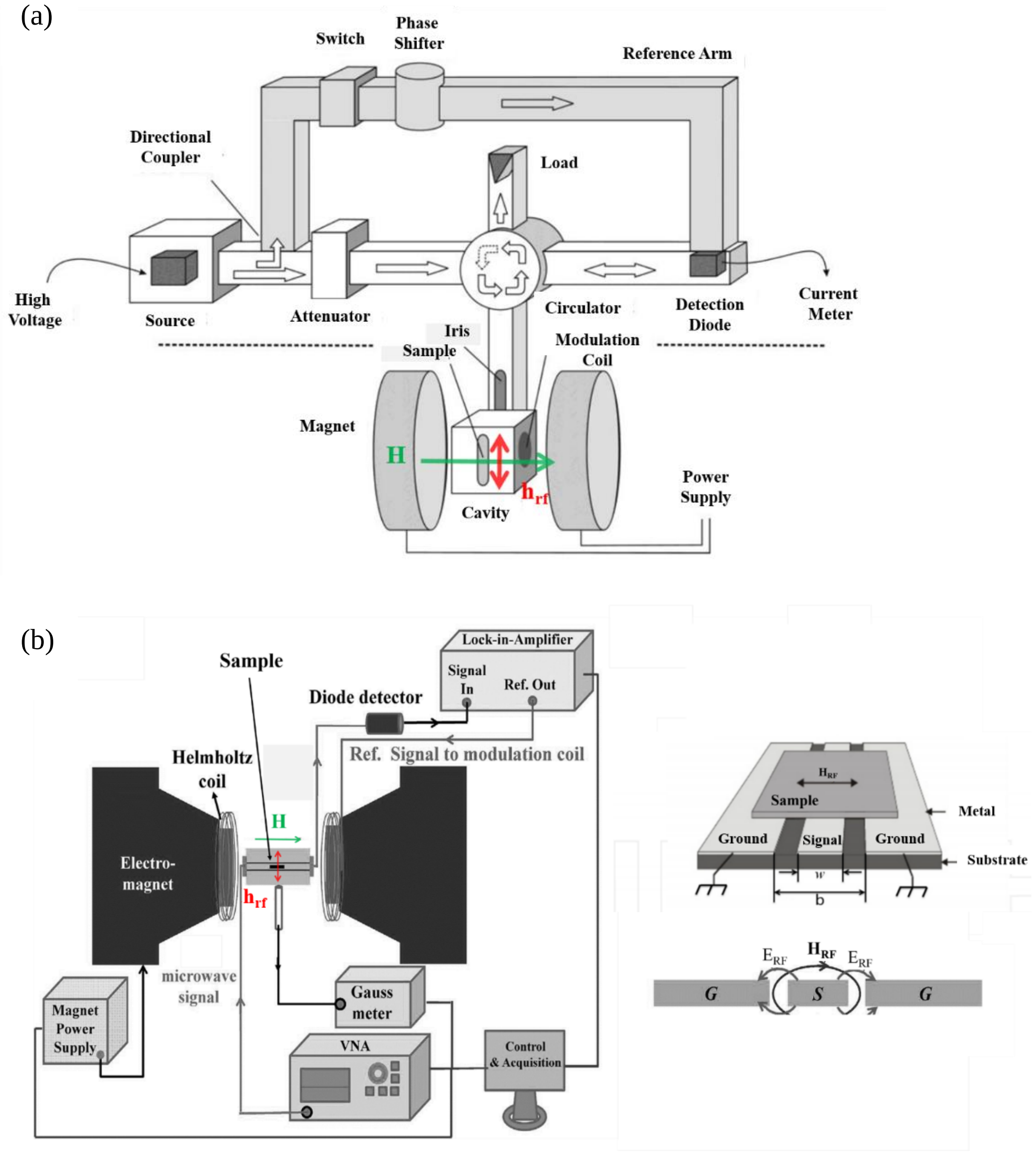

Figure 15 : Schematic illustration of the FMR spectrometer setup of : (a) a cavity based spectrometer, adapted from Ref. [110] and (b) a coplanar waveguide based spectrometer, adapted from Ref. [111][112].

Determination of physical parameters from FMR experiments.

Regardless the experimental setup, a strong absorption of the incident microwave radiation occurs and a Lorentzian-like resonance signal appears in the energy absorption spectrum. The absorbed power is given by the following relation:

$$P = \frac{1}{2}\omega\chi''\boldsymbol{h}_{\boldsymbol{rf}}^{\boldsymbol{2}} \qquad \text{(Eq. II.12)},$$

where χ'' refers to the imaginary part of susceptibility of the ferromagnet. In practice we measure the Lorentzian absorption curve of χ'' (sometimes in literature it is referred to as χ^2, including our case) as a function of the static (bias) field, **H**. We shall now explain the way to express χ'' vs H considering resonance conditions.

As shown in Figure 16, the magnetization is defined as: $\mathbf{M} = m_x\mathbf{x} + m_y\mathbf{y} + m_z\mathbf{z}$, where $m_x \sim M_s >> m_y, m_z$. Thus, the effective field takes the following form:

$$\boldsymbol{H}_{\boldsymbol{eff}} = (\boldsymbol{H} + H_u)\boldsymbol{x} + \boldsymbol{h}_{\boldsymbol{rf}}\boldsymbol{y} - \frac{M_{eff}}{M_S}m_z\boldsymbol{z} \qquad \text{(Eq. II.13)},$$

where H_u corresponds to the uniaxial anisotropy field; $H_u = \frac{2K_a^u}{\mu_0 M_S}$ (with K_a^u the uniaxial anisotropy constant) and M_{eff} is the effective magnetization: $M_{eff} = M_S - \frac{2K_a^S}{\mu_0 M_S t_F}$ (with K_a^S the surface anisotropy constant). Since the microwave field is applied in the y axis we are mainly interested in χ_{yy}. To deduce the χ_{yy} parameter we plug in Eq. II.13 to Eq. II.3 which results into the following relation [109]:

$$\chi_{yy} = \chi'_{yy} + i\chi''_{yy} = \frac{m_y}{\boldsymbol{h}_{\boldsymbol{rf}}} = M_S\frac{\left(A+i\alpha\frac{\omega}{\gamma}\right)\left[AB-\left(\frac{\omega}{\gamma}\right)^2(\alpha^2+1)-i\alpha\frac{\omega}{\gamma}(A+B)\right]}{\left[AB-\left(\frac{\omega}{\gamma}\right)^2(\alpha^2+1)\right]^2+\left[\alpha\frac{\omega}{\gamma}(A+B)\right]^2} \qquad \text{(Eq. II.14)},$$

where χ'_{yy} and χ''_{yy} are the dispersive and absorptive parts of the rf susceptibility, respectively. A = $M_{eff} + H + H_u$ and B = $H + H_u$.

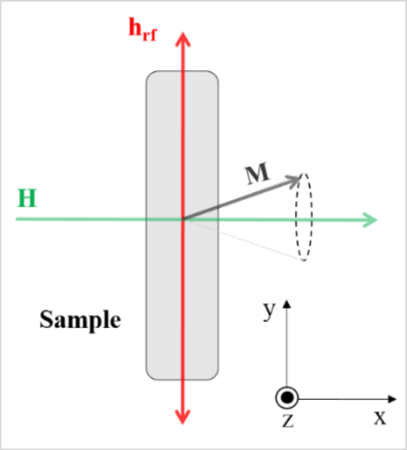

Figure 16 : Schematic representation of the measurement geometry.

The resonance condition is satisfied when the denominator in Eq. II.14 is at minimum; m_y becomes maximum for a given $\boldsymbol{h_{rf}}$. The latter can be expressed as:

$$AB - \left(\frac{\omega_{res}}{\gamma}\right)^2 (\alpha^2 + 1) = 0 \qquad \text{(Eq. II.15).}$$

Consequently, χ''_{yy} is defined as:

$$\chi''_{yy} = -M_S \frac{1}{[\frac{\omega_{res}}{\gamma}(M_{eff} + 2(\boldsymbol{H} + H_u))]^2} \qquad \text{(Eq. II.16).}$$

Note that, Eq. II.16 is a conventional Lorentzian function. Thus, the absorbed power, see Eq. II.12, is also a Lorentzian.

Since α is very small (see Eq. II.15), the resonance condition is defined as $\left(\frac{\omega_{res}}{\gamma}\right)^2 = AB$. Replacing now A and B to their original forms, we also get the Kittel resonance formula:

$$\left(\frac{\omega_{res}}{\gamma}\right)^2 = (M_{eff} + H + H_u)(H + H_u) \qquad \text{(Eq. II.17).}$$

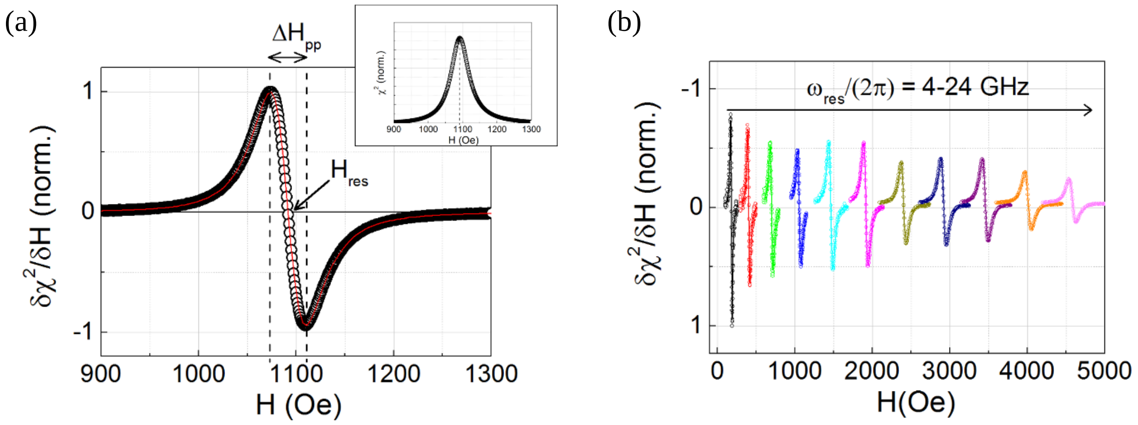

Figure 17 : (a) The real part of the susceptibility as a function of the applied field at resonance, for a typical sample with an 8-nm thick NiFe layer. The x-intercept gives the resonance field, H_{res} and the peak-to-peak resonance linewidth is ΔH_{pp}. The inset is the imaginary part of susceptibility deduced from the main graph. (b) Ferromagnetic resonance (FMR) spectra of a typical sample with a 8-nm thick NiFe layer, recorded at selected frequencies; 4 to 24 GHz with a frequency step of 2 GHz.

Figure 17(a) shows a typical FMR spectra corresponding to an 8-nm thick NiFe layer. We recall that we use a lock-in detection technique to improve the signal to noise ratio. The processed signal is the derivative of χ''_{yy} with H, i.e. the derivative of a Lorentzian function. Figure 17(b) shows typical frequency dependent measurements that are used subsequently to plot Figure 19 and verify the Kittel function. Note that, in Figure 17(b), the amplitude of the resonance peak decreases with increasing the resonant frequency, since χ''_{yy} is inversely proportional to ω_{res} (see Eq. II.16).

The red continuous line in Figure 18 is a fit to the Kittel formula, see Eq. II.17. The effective saturation magnetization, M_{eff} as well as the uniaxial anisotropy field, H_u are extracted from the fitting line: M_{eff}= 8305 Oe, (660 emu.cm^{-3}) and $H_u = 4\ Oe$. Both in good agreement with literature values [109,113] where H_u were in the range of 5 – 7 Oe and M_{eff} approximately 8790 Oe.

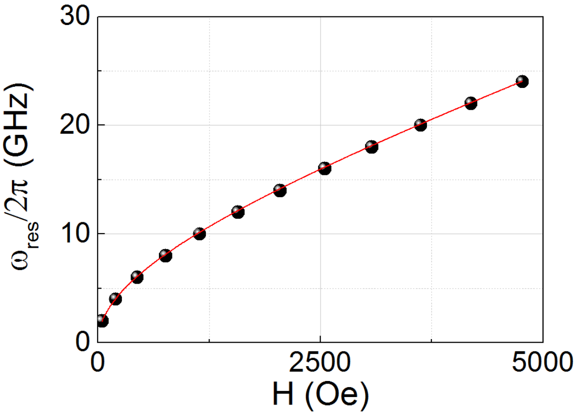

Figure 18 : The dependency of the resonance frequency on the magnetic field, for a typical sample with an 8-nm thick NiFe layer. The red continuous line is a fit to the Kittel equation, see Eq. II.17.

From the peak to peak linewidth of the FMR spectra it is possible to extract the total α Gilbert damping using the relation:

$$\Delta H_{pp} = \Delta H_0 + \frac{2}{\sqrt{3}|\gamma|}\alpha\omega_{res}, \qquad \text{(Eq. II.18),}$$

where ΔH_0 corresponds to the inhomogeneous broadening associated with the dispersion of the magnetic material parameters (see section II.1.2.2).

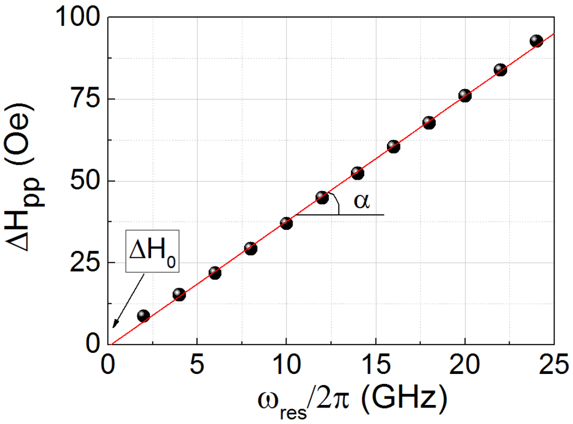

Figure 19 : The resonance linewidth as a function of frequency, for a typical sample with an 8-nm thick NiFe layer. The line through the data is fit to the Eq. II.18. Alpha Gilbert damping is extracted from the slope of the linear fit. The y-intercept reveals the inhomogeneous broadening, ΔH_0.

Figure 19 shows the peak-to-peak linewidth as a function of the frequency (deduced from the data in Figure 17(b)), which follows the expected linear dependence. The red line through the experimental data is a fit to the equation Eq. II.18. From the corresponding slope the total α Gilbert damping can be extracted which is found to be 8 x 10^{-3} for bare NiFe, in agreement with literature values [109,113–116] . The y-intercept reveals the inhomogeneous broadening, ΔH_0, which played a negligible role in our experiments.

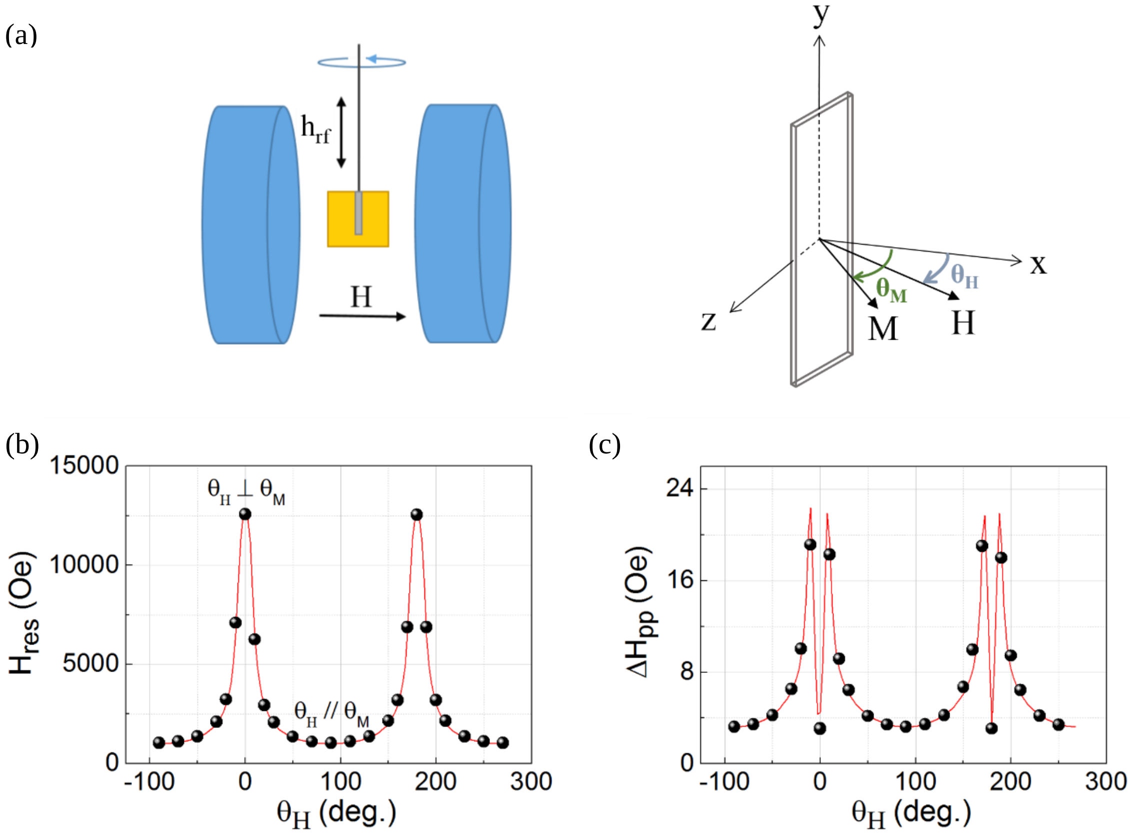

Figure 20 : (a) Simplified schematic of the spectrometer used for the resonance linewidth (ΔH_{pp}) measurements versus the applied magnetic field direction, θ_H. θ_M is the magnetization angle. Angular dependence of (b) the resonance field and (c) the resonance linewidth as a function of the applied magnetic field direction, θ_H, for a typical 8-nm thick NiFe layer. The red solid line results from numerical calculation, detailed in Figure 21.

Through angular dependence measurements it is also possible to determine the effective magnetic anisotropy, the g-factor and the effective magnetization, M_{eff}. We therefore conducted experiments where the sample was rotated about the y axis, in order to change the direction of the static (bias) field. Figure 20(a) shows the sample and field geometry. Figure 20 (b) and (c) depicts the measured and calculated angular dependence of ΔH_{pp} and H_{res} respectively, for an excitation frequency of 9.6 GHz. The resonance field increases by few kOe as we change the applied magnetic field direction and becomes maximum when the magnetization lies normal to the film plane. This corresponds to the demagnetizing field. The magnetic moments are oriented perpendicular to the film plane having their dipolar fields pointing opposite to their neighbors. ΔH_{pp} increases with the applied magnetic field angle, reaching a maximum at an intermediate angle and a minimum in the perpendicular configuration. The maximum peak is attributed to the magnetic dragging effect caused by the lag in the magnetization response to the external field direction [117].

The calculated variation of the resonance field and peak to peak linewidth are compared to the experimental results (see red solid line in Figure 20(b) and (c)). Regarding the numerical calculations we first determined the resonance field for various directions of the applied field. To do so we considered the Smit-Beljers [118] equation which is well suited for this purpose as it gives the resonance condition for small precession angles of M around its equilibrium position. It is described by the following relations:

$$\frac{\omega}{\gamma} = \sqrt{H_1 H_2} \qquad \text{(Eq. II.19),}$$

where $H_1 = H_{res}\cos(\theta_M - \theta_H) - 4\pi M_{eff}\cos(2\theta_M)$ and $H_2 = H_{res}\cos(\theta_M - \theta_H) - 4\pi M_{eff}cos^2\theta_M$. The condition for static equilibrium is satisfied when the net torque on M_s is set to zero, leading to the following expression [119,120]:

$$2H_{res}\,sin(\theta_M - \theta_H) = 4\pi M_{eff}sin(2\theta_M) \qquad \text{(Eq. II.20).}$$

Combining Eq. II.19 and Eq. II.20 we deduce the dispersion relationship: the excitation frequency as a function of the external magnetic field for various angles θ_H. The results are shown in Figure 21.

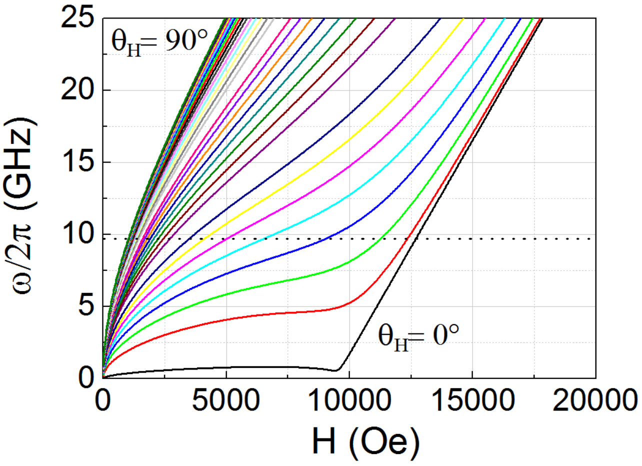

Figure 21 : Numerical simulation results of the excitation frequency versus the external magnetic field applied at different angles, θ_H. The intercept at f=9.65 GHz gives the resonance field for the corresponding angle.

The intercept at $\omega_{res}/(2\pi)$=9.65 GHz gives the resonance field for the corresponding angle. The red solid line in Figure 20(b) is the numerical fit. The g-factor and effective magnetization,

M_{eff} have been extracted: M_{eff}=9300 Oe and g=2.088 within the error bar of the fitting process, approximately 10%. Both are in agreement with what is expected for a NiFe thin film of 8 nm.

The numerical calculation of the peak to peak linewidth at a given frequency is determined as [121]:

$$\Delta H_{pp} = \Delta H_{pp}^{\alpha} + \Delta H_{\theta} \qquad \text{(Eq. II.21),}$$

where ΔH_{pp}^{α} is the Gilbert contribution to magnetization precession and ΔH_{θ} is the distribution of the demagnetizing field and the perpendicular anisotropy caused by inhomogeneities in the ferromagnetic thin film. $\Delta H_{pp}^{\alpha} = \frac{2\alpha\,\omega}{\sqrt{3}\gamma^2 M\cos(\theta_M-\theta_H)}$ and $\Delta H_{\theta} = |\frac{dH_{res}}{d\theta_H}|\Delta\theta$. The calculated values of ΔH_{pp} give satisfactory agreement with the measured values, as illustrated in Figure 20(c). The parameters α Gilbert damping and fluctuation of θ_H, Δθ are estimated from the fit lines with α=8 x 10^{-3} and Δθ=0.189°.

Having established the necessary experimental procedure to extract the parameters at room temperature, we shall focus now on extracting the temperature dependence of the total α Gilbert damping. To enable the calculation of α Gilbert damping according to the Eq. II.18 FMR linewidth as well as the inhomogeneous broadening parameter as a function of temperature have to be determined. Figure 22(a) shows the peak-to-peak linewidth as a function of temperature, extracted from individual absorption spectra recorded at various temperatures: from 10 to 300K, using a continuous wave electron paramagnetic resonance spectrometer operating at 9.6 GHz, as the one described in Figure 15(a). Figure 22(b) shows the thermal variations of ΔH_0. These data are a courtesy of C. Cheng and W. E. Bailey from the Columbia University of New York. They used a broadband FMR coplanar waveguide operating at variable frequencies. The mean value was found to be approximately 2.3 Oe with standard deviation of 0.7 Oe. Considering these results it is reasonable to conclude that ΔH_0 is a temperature-invariant parameter. Therefore for the calculation of α, ΔH_0 (T) = ΔH_0 (300K) is assumed. The dependence with temperature of total α Gilbert damping is shown in Figure 22(c). For bare NiFe, the signal agrees with the expected behavior for 3*d* transition metals [83–85]; conductivity-like behavior at low T and resistivity-like behavior at high T, see dashed lines (see also discussion in section II.1.2.1).

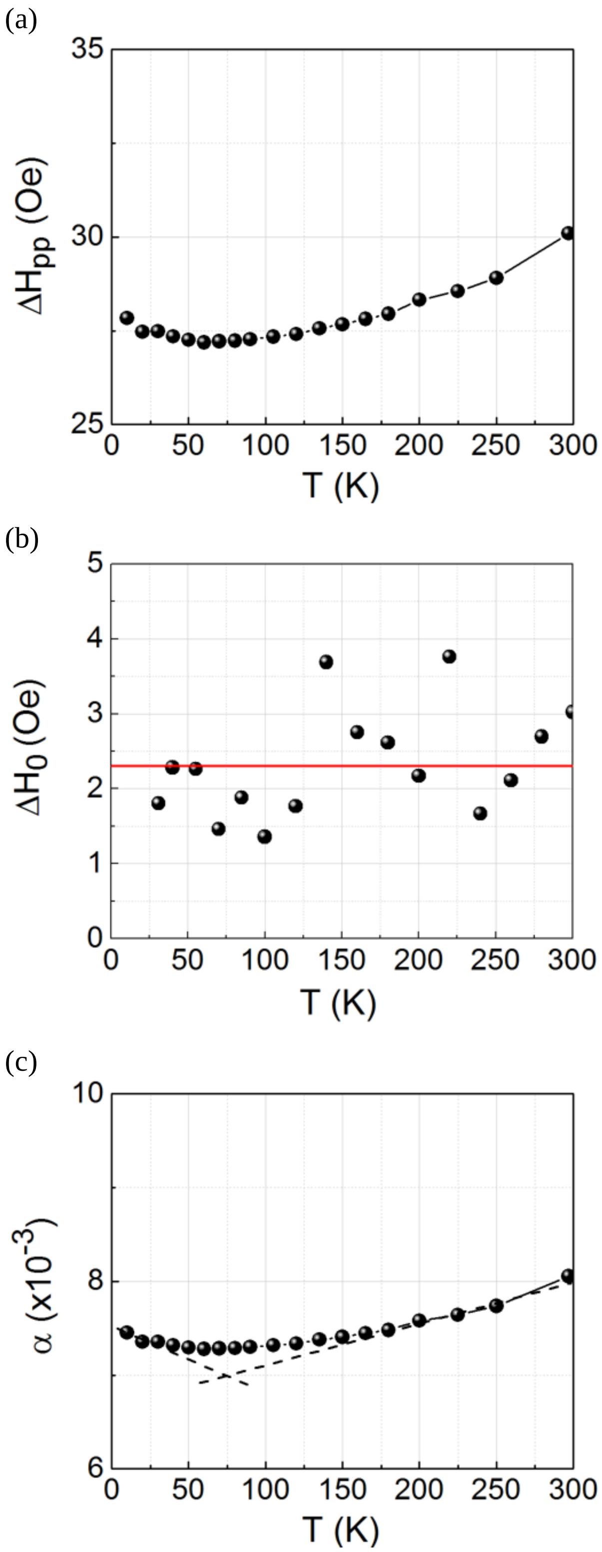

Figure 22 : (a) The temperature dependence of the NiFe resonance linewidth for Si/SiO$_2$/Cu6/NiFe8/Cu3/Al2 (nm). (b) Temperature dependence of the inhomogeneous broadening. The red line indicates the mean value. (c) The temperature dependence of the total Gilbert damping deduced from (a) and (b).

II.1.4 Problem statement

Chapter I highlighted the importance of antiferromagnetic materials as active components in new spintronic devices. Undoubtedly, the field of antiferromagnetic spintronics has witnessed a renewed interest as it opens up the door for fascinating new physics phenomena, with great scientific and technological interest. The last few years experiments on spin injection and transmission in antiferromagnets were carried out by different groups of researchers [26,28–33,122] in an attempt to identify the spin dependent transport properties of antiferromagnets. More specifically, lots of attention has been drawn on the determination of spin penetration length and the responsible relaxing mechanisms of spin currents in antiferromagnets. In the following paragraphs, a brief description of the existing literature will be addressed as well as some of the open questions which provided the foundations for the research dealt with in this thesis.

The spin penetration length [123], λ_{AF} is defined as the distance below which the spin current can travel into the spin sink without losing its coherency. Experimentally it is viewed as the saturation of α^p at a critical thickness of the antiferromagnet, see spin pumping in II.1.2.2. It is noteworthy that λ_{AF} is a material's property. One of the first studies in the field were performed at SPINTEC by Merodio and coworkers [31], who investigated the spin dependent transport of metallic antiferromagnets; IrMn and FeMn using the spin pumping technique. They recorded the extrinsic α Gilbert damping, α^p as a function of the antiferromagnetic film thickness (see Figure 23). From the corresponding dependence the responsible relaxation mechanism as well as the spin penetration length were identified for both antiferromagnets. In the case of IrMn, α^p seems to increase linearly with the thickness of the IrMn. This linear regime is typical for ferromagnetic spin sinks indicating spin dephasing as the responsible spin absorption mechanism. For FeMn the exponential dependence, mostly expected for paramagnetic spin sinks, is associated with spin flipping processes. The corresponding spin penetration lengths are depicted in Figure 23.

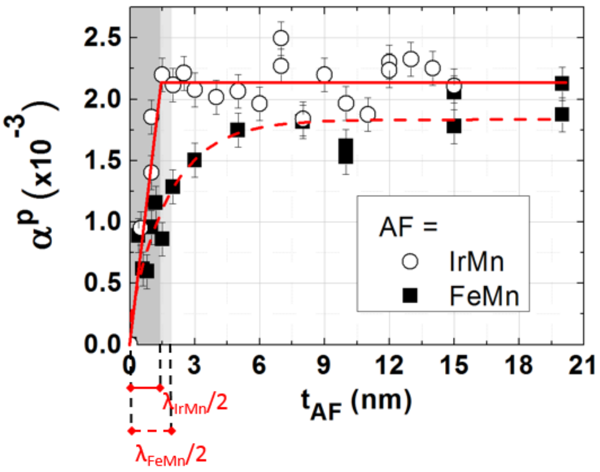

Figure 23 : Antiferromagnetic thickness dependence of the extra non-local damping, α^p for Si/SiO$_2$/NiFe8/Cu3/AF(t_{AF})/Al2 (nm) stacks where AF corresponds to IrMn and FeMn. From Ref. [31].

Further experiments were conducted in the field with the view to characterize spin-transport in different antiferromagnets both metals and insulators [26,28–30,32,122]. Inverse spin Hall effect was the most commonly employed characterization method. From the corresponding spin-to-charge conversion, valuable information were extracted, related mainly to interface characteristics, such as the spin mixing conductance and the spin Hall angle (discussed later in Chapter III.1). A cumulative list of spin penetration length for various antiferromagnets is presented in Table 1 [24]. For the sake of comparison, results for antiferromagnetic metals and insulators are tabulated together, although the physical mechanisms regulating the spin propagation significantly differ, as will be discussed in Chapter II.2 and II.3.

Certainly the spin current absorption by antiferromagnets is well documented in the literature. Nonetheless, the involved studies referred only to room temperature measurements. This was something of a pitfall as some of the corresponding antiferromagnets are expected to be paramagnetic due to their low film thickness or even undergo a magnetic phase transition. This issue clearly emphasize the need for further investigations in order to understand the role of the antiferromagnetic order on spin absorption as opposed to simple diffusive mechanisms, mostly related to the elements constituting the material [24]. More important is the fact that spin fluctuations near a magnetic phase transition are predicted to give rise to novel enhanced spin pumping mechanisms [124], although not yet observed experimentally.

AF material	**Spin penetration depth (nm)**	**ρ (μΩ.cm)**	**Technique**	**Stack**
Metallic AF in a F/N/AF stack, electronic transport through N				
$Ir_{20}Mn_{80}$	0.7	270	SP (ΔH)	NiFe/Cu/IrMn
$Ir_{50}Mn_{50}$	0.7 ± 0.2	293.3	SP	NiFe/Cu/FeMn
$Ir_{20}Mn_{80}$	≤ 1 (4.2K)	126	CPP-GMR	NiFe/Cu/IrMn/ Cu/NiFe
$Pd_{50}Mn_{50}$	1.3 ± 0.1	223	SP	NiFe/Cu/PdMn
$Fe_{50}Mn_{50}$	≤ 1 (4.2K)	87.5 ± 5	CPP-GMR	NiFe/Cu/FeMn/ Cu/NiFe
$Fe_{50}Mn_{50}$	1.8 ± 0.5	167.7	SP	NiFe/Cu/FeMn
$Fe_{50}Mn_{50}$	1.9	135	SP (ΔH)	NiFe/Cu/FeMn
$Pt_{50}Mn_{50}$	0.5 ± 0.1	164	SP	NiFe/Cu/PtMn
$Pt_{50}Mn_{50}$	2.3	$119+260/t_{AF(nm)}$	ST-FMR (HR)	FeCoB/Hf/PtMn
Metallic AF in a F/AF stack, electronic and magnonic transport regimes				
$Ir_{25}Mn_{75}$	0.5	250	ST-FMR	NiFe/IrMn
$Fe_{50}Mn_{50}$	2	166	ST-FMR (HR)	NiFe/FeMn/Pt
$Fe_{50}Mn_{50}$	< 2 electronic	/	SP	NiFe/FeMn/W
$Fe_{50}Mn_{50}$	9 magnonic	/	SP	NiFe/FeMn/W
Cr	2.1	25 - 325	SSE	YIG/Cr
Cr	4.5 (4.2K)	180 ± 20	CPP-GMR	Fe/Cr/Fe

Cr	13.3	500 - 1200	SP	YIG/Cr
Mn	10.7	980	SP	YIG/Mn
Insulating AF in a F/AF stack, magnonic transport				
NiO	1.3	>>	SSE	YIG/NiO/Ta
NiO	2.5	>>	SSE	YIG/NiO/Pt
NiO	2 - 5.5 (180 - 420K)	>>	SSE	YIG/NiO/Pt
NiO	2	>>	SP	YIG/NiO/Pt
NiO	3.9	>>	SP	YIG/NiO/Pt
NiO	9.8	>>	SP	YIG/NiO/Pt
NiO	10	>>	SP	YIG/NiO/Pt
NiO	50	>>	ST-FMR	NiFe/NiO/Pt
α-NiFe$_2$O$_4$	6.3	>>	SP	NiFe/α-NiFe$_2$O$_4$/Pt
α-YIG	3.9	>>	SP	NiFe/α-YIG/Pt
Cr$_2$O$_3$	1.6	>>	SP	Cr$_2$O$_3$

Table 1 : Spin penetration depth, and resistivity (ρ) for various antiferromagnetic materials. Finite size effects on ρ are reported in the table, whenever available. Unless specified otherwise, NiFe is close to Ni$_{81}$Fe$_{21}$, the composition of Permalloy, and YIG stands for epitaxial Y$_3$Fe$_5$O$_{12}$. When not specified the investigation temperature was 300 K. CPP-GMR = current perpendicular to plane excitation – giant magneroresistance detection, SP and SP (ΔH) = ferromagnetic resonance spin pumping excitation – inverse spin Hall effect detection when not specified, and ferromagnetic resonance linewidth detection when (ΔH) is specified, ST-FMR and ST-FMR (HR) = spin torque ferromagnetic resonance excitation induced by spin Hall effect as a result of an ac current flow – anisotropic magnetoresistance detection when not specified, and 2nd harmonic response detection of the anomalous Hall effect and/or anisotropic magnetoresistance when (HR) is specified, and SSE = longitudinal spin Seebeck excitation induced by a thermal gradient – inverse spin Hall effect detection. Table and caption from Ref. [24]. See Refs. therein.

II.2 Enhanced spin pumping efficiency at magnetic phase transition [1]

This section is adapted from Ref. [1] where the main findings were published.

The initial theoretical framework of spin pumping involves adiabatic charge pumping and a quality called spin mixing conductance [125] (section II.1.2.2). Recently, a linear-response formalism was developed to complete the existing theories and describe spin pumping near thermal equilibrium [124]. This formalism predicts a large enhancement of spin pumping near the magnetic phase transition due to spin sink fluctuations. These predictions, if validated experimentally, would help to progress towards more efficient spin sources, while also providing an alternative method to probe magnetic phase transitions. This type of alternative method is particularly needed in the case of materials with no net magnetic moments, such as antiferromagnets.

Extrapolating for the case of all-antiferromagnets devices [126], the order-disorder Néel temperature would set the thermal threshold for data retention. This temperature relates to the exchange stiffness between antiferromagnetic moments [15,16]. Sometimes, it is mistakenly confused with the blocking temperature which is specific to ferromagnetic/antiferromagnetic exchange bias interaction, but the Néel temperature is intrinsic to the antiferromagnet [15,16]. The blocking temperature is easily determined experimentally, for example by measuring the loss of the hysteresis loop shift as the external temperature rises, or by using specific field-cooling protocols [127,128]. In contrast, it is much more challenging to determine the Néel temperature of an isolated antiferromagnetic thin film. Despite the importance of such a basic parameter for antiferromagnetic spintronics, very few quantitative data have been published so far, see Titles I to III in Ref. [24], because of a lack of routinely available rapid measurement techniques compatible with most antiferromagnetic thin films. To our knowledge, neutron diffraction [129], magnetic susceptibility [130], nanocalorimetry [131], and resistivity measurements [132] are only appropriate for sufficiently thick single layers or for multiply repeated thinner layers.

II.2.1 Samples fabrication and structural characterization

In order to investigate the absorption of a spin current by antiferromagnetic IrMn thin films and deduce consequently the corresponding spin dependent parameters, we performed spin pumping experiments at various temperatures on Si/SiO_2/NiFe8/Cu3/IrMn(t_{IrMn})/Al2 (nm) stacks.

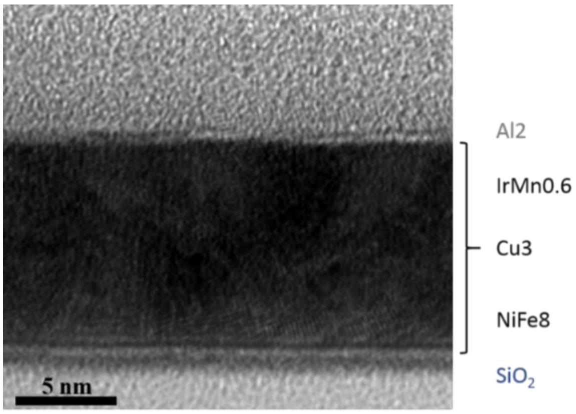

Figure 24 : Transmission electron microscopy image (TEM) for a Si/SiO_2/NiFe8/Cu3/IrMn0.6/Al2 (nm) sample. The TEM measurement was subcontracted to SERMA technologies.

The stacks were deposited at SPINTEC by Stéphane Auffret, at room temperature on thermally oxidized silicon substrates by dc-magnetron sputtering. A variable thickness of IrMn, t_{IrMn}, was deposited from an $Ir_{20}Mn_{80}$ target (at. %). The NiFe8 layer was deposited from a $Ni_{81}Fe_{19}$ target. To prevent oxidization in air, an Al2 cap was added which forms an AlOx protective film. This layer is known to have low spin current absorption properties. Because the spin diffusion length of copper is much longer than 3 nm, a Cu3 layer can eliminate exchange bias coupling without altering the spin propagation between the NiFe and IrMn layers. The influence of exchange coupling in samples without Cu layer will be discussed later in section II.3. Cu5 layers were also tested instead of Cu3. From the results we could conclude that it made no difference on the findings that will be presented below.

Transmission electron microscopy (TEM) analysis (Figure 24) was used to investigate the composition of a typical sample. A sample piece was capped with SiO_2 in preparation for the TEM experiment. This cap protects the sample's surface from damage during the thinning and polishing steps required for TEM. The cross sectional TEM image does not show sharp interfaces between the NiFe, Cu and IrMn layers. However the overall thickness of the stack NiFe/Cu/IrMn corresponds to the expected value (between 11.5 and 11.8 nm). The deviation from the ideal case suggests that we are probably dealing with species mixing and alloys formation. Energy-dispersive x-ray analysis, EDX (Figure 25) further confirms species mixing and alloys formation within the structure. It is actually well known that Cu and IrMn intermix at interfaces [133,134].

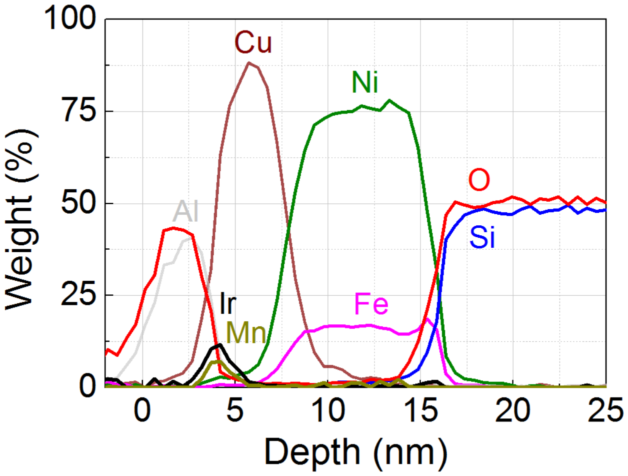

Figure 25 : Energy-dispersive x-ray spectroscopy (EDX) data for a $Si/SiO_2/NiFe8/Cu3/IrMn0.6/Al2$ (nm) sample. The EDX measurement was subcontracted to SERMA technologies.

II.2.2 Enhanced spin pumping by IrMn antiferromagnetic thin films

A series of ferromagnetic resonance spectra were recorded for temperatures (T) ranging between 10 and 300 K, using the continuous wave electron paramagnetic resonance spectrometer operating at 9.6 GHz fitted with a dual-mode rectangular cavity, see II.1.3. For each temperature the peak-to-peak linewidth (ΔH_{pp}) was determined by fitting the spectrum to a Lorentzian derivative and the total Gilbert damping (α) was extracted, as described in Chapter II.1.3.

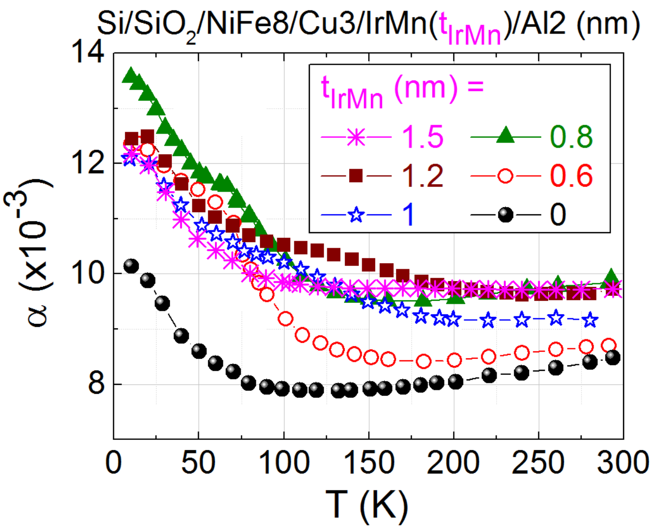

Figure 26 : The temperature dependence of the total α Gilbert damping as a function of temperature for Si/SiO$_2$/NiFe8/Cu3/IrMn(t_{IrMn})/Al2 (nm) stacks, where t_{IrMn} corresponds to thickness of the IrMn layer. From Ref. [1].

Figure 26 shows α plotted against temperature. The data for t_{IrMn}=0 correspond to the temperature dependence of the Gilbert damping that is used as a reference here: α^0. Although it is not of big importance in the present study, it will be shown later in section II.4 that α^0 does not correspond to the intrinsic Gilbert damping. In fact it is the sum of the intrinsic Gilbert damping and the additional damping related to the bottom SiO$_2$/NiFe interface. In the presence of the IrMn layer, the NiFe damping is the sum of local intrinsic damping and additional nonlocal damping (α^p) associated with the IrMn layer acting as a spin sink. From Figure 26 we estimated α(295 K) ~ (8.5; 8.7; 9.9; 9.25; 9.75; and 9.75) × 10^{-3} for t_{IrMn} = 0, 0.6, 0.8, 1, 1.2, and 1.5 nm, respectively. The overall increase of α with spin sink thickness up to a plateau from $t_{IrMn} = \lambda_{IrMn}/2$, was discussed in chapter II.1.4. This profile relates to the finite spin penetration length λ_{IrMn} for the spin sink. For IrMn, the penetration length at room temperature was approximately 0.7 nm [31]. The higher value we observed for t_{IrMn} = 0.8 nm may be due to oscillations when nearing saturation [135,136], but this is beyond the scope of our study.

The temperature dependence of the IrMn contribution to NiFe damping can be directly isolated from $\alpha^p(T) = \alpha(T) - \alpha^0(T)$, as illustrated in Figure 27(a). The central point of our study is that the signal displays a bump in α^p ($\delta\alpha^p$), highlighting a novel enhanced spin pumping effect. The position of this spin pumping peak depends on the temperature, which is related to the thickness of the IrMn layer. In an effort to isolate the effect, we deduced $\delta\alpha^p$ and $\delta\alpha^{p,max}$ as follows; we subtracted the baseline for each sample in a way that it either follows the natural trend of the signal or it is temperature invariant. For each peak $\delta\alpha^p$ and $\delta\alpha^{p,max}$ is recorded and compared in Figure 27(b). Qualitatively, $\delta\alpha^p$ reduces with the thickness of IrMn which will be discussed later on. In fact, a recent theory by Ohnuma and co-workers links $\delta\alpha^p$ to the interfacial spin mixing conductance [124]. This spin mixing conductance depends on the dynamic transverse spin susceptibility of the spin sink, which is known to vary around critical temperatures. Accordingly, the enhanced spin pumping efficiency observed here can be attributed to the fluctuating IrMn spin sink, around its magnetic phase transition. An arrow is added in Figure 27(a) to indicate the critical temperature, $\mathrm{T}_{\mathrm{crit}}^{\mathrm{IrMn}}$ of IrMn0.8 nm.

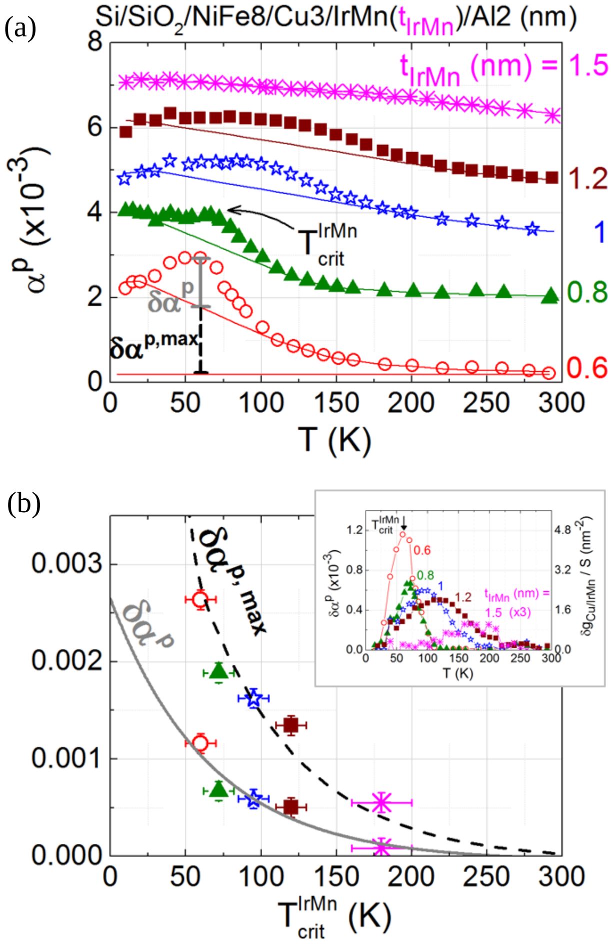

Figure 27 : (a) Dependence of additional extra non-local damping (α^{p}) on temperature. To facilitate reading, the data were shifted vertically. Note: α^{p} (295 K) ~ (0.2, 1.4, 0.75, 1.25 and 1.25) × 10^{-3} for t_{IrMn} = 0.6, 0.8, 1, 1.2, and 1.5 nm, which translates to $g_{eff}^{\uparrow\downarrow}$ /S (295 K) ~ 0.8, 5.6, 3, 5, and 5 nm^{-2}, respectively. The baselines are visual guides. From Ref. [1]. (b) Dependence of $\delta\alpha^{p,max}$ on temperature for T=T_{crit}^{IrMn}. An exponential function was fitted to the data as a visual guide. Inset: Temperature dependence of $\delta\alpha^{p}$. Adapted from Ref. [1].

Transposed to our case, the theory by Ohnuma et al. [124] predicts:

$$\delta\alpha^{p} = \frac{1}{4\pi S_0 N_{SI}} g^{\uparrow\downarrow}_{Cu/IrMn} \qquad \text{(Eq. II.22),}$$

where S_0 is the norm of the spin operator, N_{SI} is the number of lattice sites in the NiFe spin injector (SI), and $g^{\uparrow\downarrow}_{Cu/IrMn}$ is the spin mixing conductance across the Cu/IrMn interface.

As indicated by the corresponding theory, this last parameter is defined by:

$$g_{Cu/IrMn}^{\uparrow\downarrow} = \frac{8\pi J_{sd}^2 S_0^2 N_{\mathrm{int}}}{\hbar^2 N_{SS}} \sum_k \frac{1}{\Omega_{rf}} \mathrm{Im}\, \chi_k^R\left(\Omega_{rf}\right) \qquad \text{(Eq. II.23)},$$

where J_{sd} is the *s-d* exchange interaction at the Cu/IrMn interface, N_{int} is the number of localized spins at the interface, N_{SS} is the number of lattice sites in the IrMn spin sink (SS), k is the wave vector, Ω_{rf} is the NiFe angular frequency at resonance, and $\chi_k^R\left(\Omega_{rf}\right)$ is the dynamic transverse spin susceptibility of the IrMn layer. This model was initially developed for SS/SI bilayers but it can also be applied for the SS/Cu/SI trilayers described here since: (i) spin absorption by 3 nm of Cu is negligible, and (ii) the contribution of the SS/Cu interface is cancelled out when calculating α^p.

The expression of $g_{Cu/IrMn}^{\uparrow\downarrow}$ in Eq. II.23 elucidates also the thickness scaling effect, as when the thickness of the antiferromagnet is increased the ratio N_{int}/N_{SS} becomes less important. It is fair thus to conclude that it is an interfacial effect, as illustrated in Figure 27(b).

Alternatively, the variation corresponding to $g_{Cu/IrMn}^{\uparrow\downarrow}$ can be calculated from [101] (see also Eq. II.11 and the corresponding discussion) :

$$\frac{\delta g_{eff}^{\uparrow\downarrow}}{S} = \frac{4\pi M_{S,NiFe} t_{NiFe}}{|\gamma|\hbar} \delta\alpha^p \qquad \text{(Eq. II.24)},$$

where $g_{eff}^{\uparrow\downarrow}$ is the effective spin mixing conductance across the whole stack, $M_{S,NiFe}$ is the saturation magnetization of the NiFe layer, and t_{NiFe} is its thickness.

We measured the temperature dependence of $M_{S,NiFe}$ separately using a vibrating sample magnetometer, as shown in Figure 28. The results confirmed that, in the 10–300 K range, far from the NiFe Curie temperature, $M_{S,NiFe}$ only decreases slightly with temperature. At room temperature $M_{S,NiFe}$= 700 emu/cm^3. For the specific case of NiFe/Cu/SS trilayers, as shown by Ghosh et al. [123], because of cancellation of terms, $g_{eff}^{\uparrow\downarrow} \sim g_{Cu/SS}^{\uparrow\downarrow}$. More specifically, $1/g_{eff}^{\uparrow\downarrow} = 1/g_{NiFe/Cu}^{\uparrow\downarrow} - 1/g_{Sharvin,Cu}^{\uparrow\downarrow} + 1/g_{Cu/SS}^{\uparrow\downarrow}$, with $g_{NiFe/Cu}^{\uparrow\downarrow} \sim g_{Sharvin,Cu}^{\uparrow\downarrow} = 15$ nm^{-2}. We therefore took $\delta g_{eff}^{\uparrow\downarrow} = \delta g_{Cu/IrMn}^{\uparrow\downarrow}$ in Eq. II.24. The resulting values of $g_{Cu/IrMn}^{\uparrow\downarrow}$ range between 0 to 4.7 nm^{-2}. That is to say $g_{Cu/IrMn}^{\uparrow\downarrow}$ at $T_{\mathrm{crit}}^{\mathrm{IrMn}}$ for IrMn0.6, IrMn0.8, IrMn1, IrMn1.2 and IrMn1.5 takes the following values 4.7, 2.75, 2.4, 2, 0 nm^{-2}, respectively. Note that the experimental framework may differ from the ideal theoretical one, since the IrMn structure and the Cu/IrMn interface are altered by species mixing and alloy formation [134]. In addition, the influence on $g_{Cu/IrMn}^{\uparrow\downarrow}$ of the nontrivial orientation of the IrMn moments with respect to the interface [137] almost certainly complicates the real picture.

It should be emphasized that our experimental data show the antiferromagnetic to paramagnetic phase transition as an explanation for the enhancement of spin pumping. This was also demonstrated in YIG/CoO and YIG/NiO systems [138]. The authors attributed the enhanced spin pumping efficiency to the antiferromagnetic phase transition, that was further corroborated by X-ray magnetic linear dichroism measurement using a synchrotron facility [138].

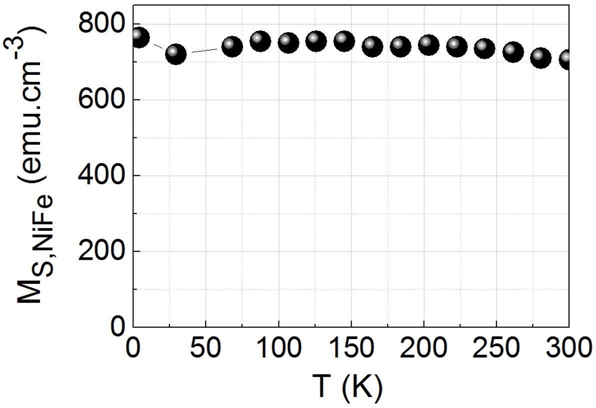

Figure 28 : Saturation magnetization as a function of temperature for a Si/SiO_2/NiFe8/Cu3/Al2 (nm) stack.

II.2.3 Finite size effects on the critical temperature for the magnetic phase transition

Figure 29 illustrates how the IrMn layer critical temperature (T_{crit}^{IrMn}) deduced from Figure 27(a) is linearly related to its thickness. This behaviour is corroborated by theoretical calculations taking magnetic phase transitions and finite size scaling into account [139].The model considers the finite divergence of the phenomenological spin-spin correlation length (n_0) near the critical temperature. For $t_{IrMn} < n_0$,

$$T_{crit}^{IrMn}(t_{IrMn}) = T_N^{IrMn}(bulk)\,\frac{t_{IrMn}-d}{2n_0} \qquad \text{(Eq. II.25),}$$

where $T_N^{IrMn}(bulk)$ is the Néel temperature of the IrMn bulk, equal to 700 K [26], and d is the interatomic distance. X-ray diffraction measurements of similar samples revealed a (111) growth direction and a related interatomic distance d of about 0.22 nm, similar to that for bulk IrMn [129]. Fitting our data to Eq. II.25 Figure 29(a) returned a spin-spin correlation length of n_0 =2.7 +/– 0.1 nm (around 12 monolayers). Typical correlation lengths for ferromagnets range from a few monolayers up to ten monolayers [139]. The data point for t_{IrMn}=2 nm is taken from Petti et al. [126], but was measured by calorimetry on a different stacking. The level of agreement is, nevertheless, satisfactory. We also noted that T_{crit}^{IrMn} = 300 K for t ~ 2.7 nm. Extrinsic damping due to IrMn spin sinks (α^p) [31] and the amplitude of the inverse spin Hall effect (ISHE) in IrMn layers [29] were found to be invariant around t_{IrMn} ~ 2.7 nm at 300K (see also Figure 23). Thus, α^p and ISHE are only mildly sensitive to the static magnetic ordering, but more so to the nature of the elements constituting the alloy.

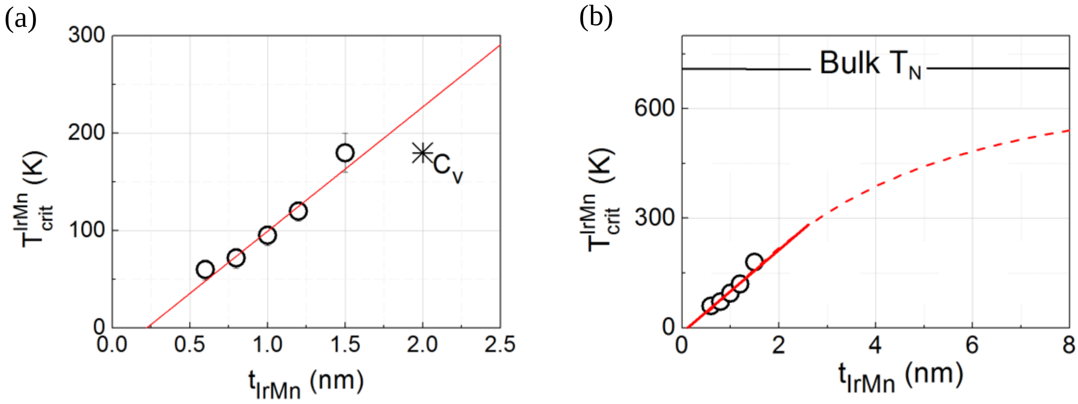

Figure 29 : Dependence of T_{crit}^{IrMn} on tIrMn. (a) The line is a fit based on Zhang et al. [139] in the thin-layer regime. The data point for t_{IrMn} = 2 nm is taken from Petti et al. [126]. (b) T_{crit}^{IrMn} vs t_{IrMn} for a wider scale, along with the calculation in the thick-layer regime (dashed line). Adapted from Ref. [1].

It should be noted that these data relate to polycrystalline films. In such a case, the different direction of the moments probably averages out any anisotropic spin relaxation contribution due to the magnetic order [24]. Because of fluctuations in the magnetic order, a bump is still expected at the threshold thickness [140]. Finally, for $t_{IrMn}>n_0$ the model presented by Zhang et al. [139] gives

$$T_{crit}^{IrMn}(t_{IrMn}) = T_N^{IrMn}(bulk)\left[1-\frac{n_0+d}{2t_{IrMn}}\right]^{\lambda} \qquad \text{(Eq. II.26)},$$

with λ=1. Knowing n_0 and using Eq. II.26 we can predict T_{crit}^{IrMn} vs t_{IrMn} for thick IrMn layers, as illustrated in Figure 29(b). Since critical temperatures are strongly linked to the extension of spin-spin interactions, we investigated the effect of the environment surrounding the IrMn layer. We fabricated Si/SiO$_2$/NiFe8/Cu3/IrMn0.8/Cap2 (nm) multilayers using various materials for the capping layer such as Pt and Pd, which are known to polarize easily. This could have enhanced n_0 and consequently T_{crit}^{IrMn}, but T_{crit}^{IrMn} remains unaffected by its environment, as shown in Figure 30.

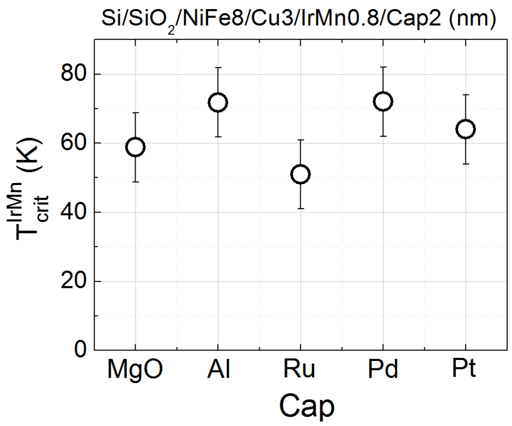

Figure 30 : T_{crit}^{IrMn} for various capping layers for Si/SiO$_2$/NiFe8/Cu3/IrMn0.8/Cap2 (nm) stack, where Cap=MgO, Al, Ru, Pd, Pt. Adapted from Ref. [1].

II.2.4 Search for anisotropic effects

We have seen in section II.2.2 from Eq. II.23 that the enhanced spin pumping probed here directly relates to the magnetic susceptibility. It is known that the temperature dependence of the magnetic susceptibility of antiferromagnets can be anisotropic (e.g. for collinear bipartite antiferromagnet). Consequently this would translate into anisotropic enhanced spin pumping. A typical paradigm measuring a collinear antiferromagnet, MnF_2 is depicted in Figure 23. Since IrMn is a non-collinear antiferromagnet, an isotropic enhancement of the Gilbert damping is anticipated regardless the applied magnetic field direction. The latter is presented in Figure 32 where Si/SiO_2/NiFe8/Cu3/IrMn0.6/Al2 was tested at 0, 25, 60 and 80° (almost perpendicular) as a function of temperature. The results were normalized to ease the reading.

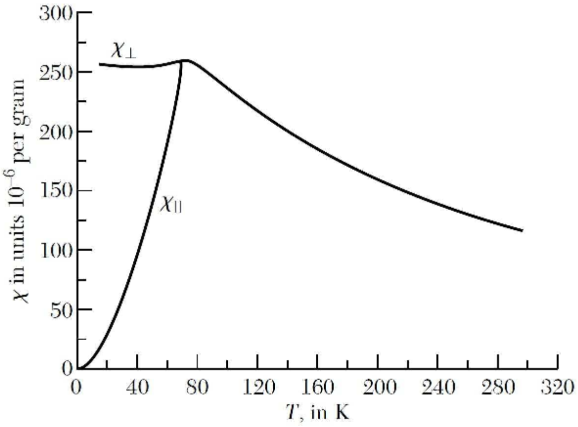

Figure 31: Temperature dependence of the magnetic susceptibility of MnF_2 single crystal. From Ref. [141].

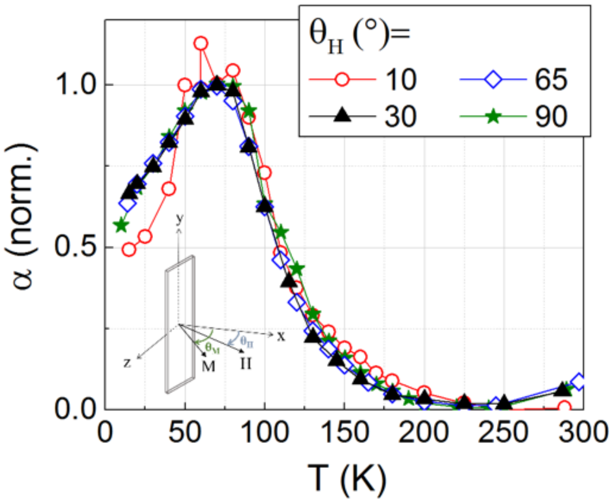

Figure 32 : α Gilbert damping vs temperature, for different applied magnetic field direction, θ_H; 10, 30, 65 and 90° for Si/SiO_2/NiFe8/Cu3/IrMn0.6/Al2 nm stack. For θ_H = 90, 65, 30 and 10° we get α(300K) and α(70K) = (8.5 x 10^{-3}, 9.7 x 10^{-3}, 17.7 x 10^{-3}, 32.6 x 10^{-3}) and (10.8 x 10^{-3}, 12.1 x 10^{-3}, 22.2 x 10^{-3}, 42.6 x 10^{-3}), respectively.

It should be noted here that similar experiments with CuMnAs collinear bipartite antiferromagnet have also been envisioned in collaboration with the University of Nottingham but postponed due to technical issues.

II.2.5 Impact of double spin pumping

So far we have examined the influence of a single spin sink on the temperature dependence of the NiFe Gilbert damping. By introducing a second IrMn layer into our structure, we investigated the effect of two spin sink absorbers as a function of temperature. For this purpose we fabricated the following structures; Si/SiO_2/Cu11/(IrMn0.6/Cu3)/NiFe8/(Cu3/IrMn0.6)/Al2 (nm) the so-called “double IrMn”, Si/SiO_2/Cu11/NiFe8/(Cu3/IrMn0.6)/Al2, the so-called “top IrMn” and Si/SiO_2/Cu11/(IrMn0.6/Cu3)/NiFe8/Cu3/Al2 (nm) the so-called “bottom IrMn”.

As can be seen from Figure 33 the single IrMn samples showed the expected peak at 65K and a similar value of $\delta\alpha^p$, in line with the previous findings. For the double IrMn sample we found a much higher value of about twice $\delta\alpha^p$ which can be justified by the presence of two spin absorbers placed about the precessing ferromagnet, NiFe. The total Gilbert damping, α in this case (e.g. see at 300K) also equals the intrinsic Gilbert damping, α^0 plus two times the extra non-local damping, α^p.

Despite of the apparent simplicity of the experiment, growth optimizations were necessary in order to obtain the desired IrMn structure. In fact fcc IrMn grows poorly on SiO_2 and that is why an additional Cu was used as buffer layer between SiO_2 and bottom IrMn which was subsequently used in all three stacks. However, even though fcc IrMn grows satisfactorily well on Cu, Cu itself wets poorly on SiO_2. Thus a sufficiently thick Cu layer is required in order to achieve the same growth quality for the single bottom and single top layers, for the sake of comparison (here we used 11 nm, more details will be given in section II.5). An example of the effect of Cu buffer layer thickness is given in Figure 34. The poor growth of IrMn on Cu3 results into a smaller critical temperature, which can be seen as a downshift of the maximum of spin pumping.

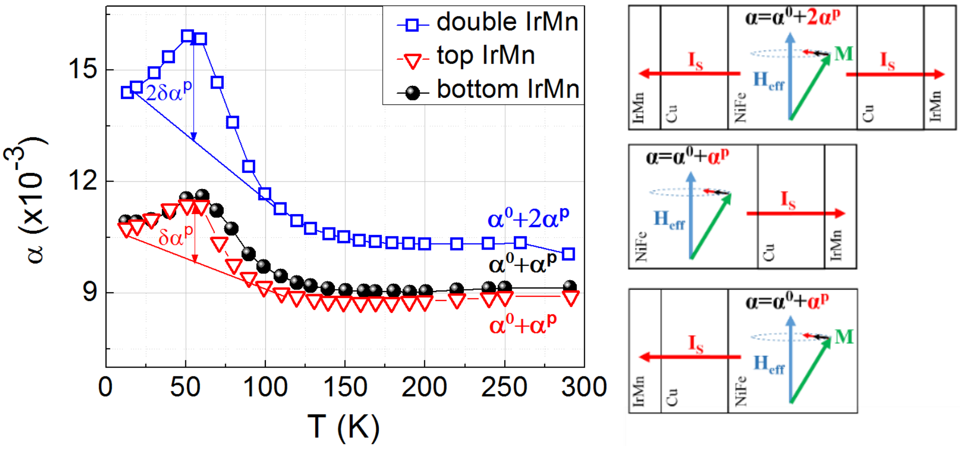

Figure 33 : α Gilbert damping vs temperature, for “double IrMn”, “top IrMn” and “bottom IrMn” spin sinking.

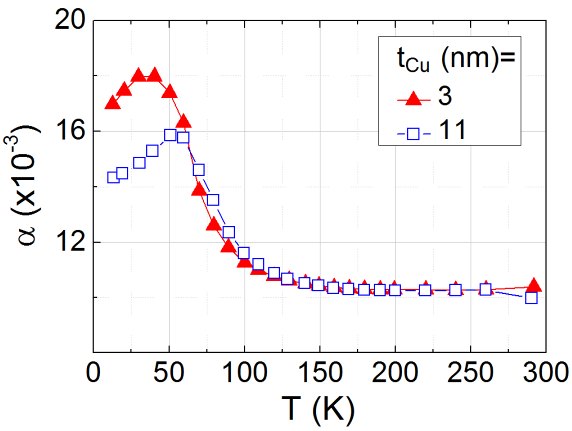

Figure 34 : Dependence of α on temperature, for Si/SiO$_2$/Cu(t_{Cu})/IrMn0.6/Cu3/NiFe8/Cu3/IrMn0.6/Al2 (nm) stacks.

In conclusion, the main contribution here is the experimental evidence that enhanced spin pumping efficiency can truly be achieved by using a fluctuating spin sink around the transition temperature for its magnetic order. This finding corroborates a recent theory linking enhanced spin pumping into a fluctuating spin sink to the interfacial spin mixing conductance. This spin mixing conductance depends on the transverse spin susceptibility of the spin sink, which is known to vary around critical temperatures. Spin pumping efficiency could be ultimately enhanced by including other magnetic orders and materials, preferably with large spin-orbit coefficients since larger enhancements are expected in such cases [124].

Finally, we showed that it is possible to detect magnetic phase transitions by spin pumping opening a new pathway for the further investigation of nontrivial magnetic orders, such as antiferromagnetism, with no net magnetic moment and potentially large magnetotransport effects. For example, by spotting the spin pumping peak, we experimentally determined how the IrMn critical temperature depended on the thickness of this layer. This information provided access to a fundamental parameter (the characteristic length for spin- spin interactions) which can be used to predict the full critical temperature vs thickness dependence. Until now, for IrMn, this parameter had been experimentally inaccessible, and it remains to be measured for numerous common antiferromagnets, including FeMn, PtMn, and Mn$_2$Au.

II.3 Electronic vs. magnonic spin transport [2]

Previously, the experimental results revealed an enhanced spin pumping efficiency in the temperature dependence of α Gilbert damping, attributed to the fluctuating magnetic order of the antiferromagnetic IrMn at its magnetic phase transition. It is important to emphasize that there was no exchange bias present in the system due to the presence of copper between NiFe and IrMn.

One complementary question is whether the exchange interaction could possibly have an effect on the spin current absorption by IrMn and especially at its magnetic phase transition. In the following subsection we will try to answer to this question after investigating similar structures as the ones examined in Chapter II.2 with the only exception being the absence of copper; Si/SiO$_2$/NiFe8/IrMn(t_{IrMn})/Al2 (nm) stacks, where t_{IrMn} corresponds to thickness of the IrMn layer, which varies from 0.6 to 1.2 nm. In fact, the presence or absence of a Cu layer defines the nature of the spin transport as magnonic transport is expected when NiFe is exchanged coupled to IrMn, whereas purely electronic transport is anticipated through Cu when the coupling is broken due to Cu.

Figure 35 illustrates the spin pumping experiments for the two structures under investigation; Si/SiO$_2$/NiFe8/Cu3/IrMn(t_{IrMn})/Al2 and Si/SiO$_2$/NiFe8/IrMn(t_{IrMn})/Al2 (nm).

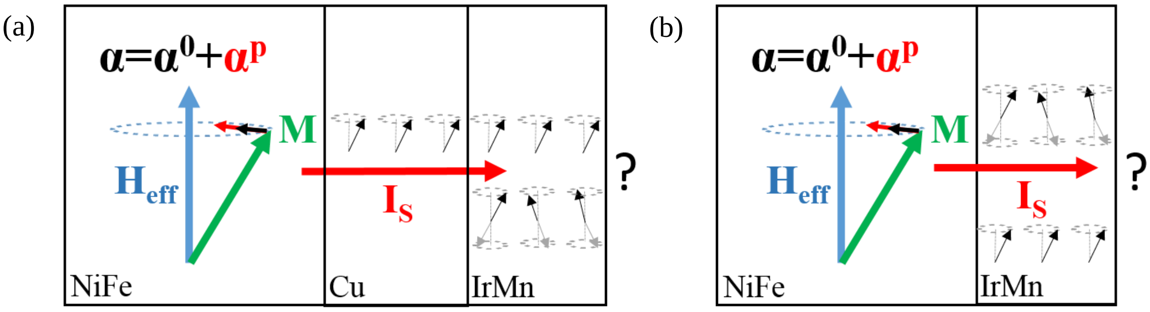

Figure 35 : Diagram representing the spin pumping experiment in (a) ‘electronic’ versus (b) ‘magnonic’ transport. In (a) the transport in Cu layer is purely electronic.

Electronic transport through Cu

In the first case (see Figure 35(a)), the spin transport is mediated by a purely electronic transport regime through Cu. The spin propagation is not altered by passing through this layer and will eventually reach and get absorbed by the IrMn layer. Previous investigations dealing with structures similar to NiFe/Cu/IrMn have demonstrated [29,58,142,143] that the spin pumping is the main mechanism responsible for the resulting α Gilbert damping. In these structures the spin mixing conductance across the interface between Cu/IrMn is of big importance as it defines the efficiency of spin angular momentum transfer.

Magnonic transport

In the absence of Cu (see Figure 35(b)), the transfer and propagation of spin angular momentum directly involves magnonic transport, meaning that IrMn is fed by spin waves through direct magnetic coupling with NiFe. Therefore the spin angular momentum transport shall be highly dependent on the exchange interaction and the interface magnetic ordering. To put it simply, due to the exchange anisotropy at the interface the precessing ferromagnet pulls the antiferromagnetic moments and as a result, the spin angular momentum transfer will suffer from additional dissipation of energy. The dissipation rate is believed to be proportional to the exchange bias and to the magnetic susceptibility of the antiferromagnet.

Electronic vs Magnonic transport

In an attempt to understand the underlying phenomena associated with each structure, we examined the temperature dependence of α Gilbert damping, illustrated in Figure 36(a)-(b). To ease the reading and facilitate the interpretation of the results shown in Figure 36 we have plotted the IrMn thickness dependence on $T_{\mathrm{crit}}^{\mathrm{IrMn}}$, $\delta\alpha^{p}$ and H_E for both configurations. The results are summarized in Figure 37.

For the NiFe/IrMn (Figure 36(b)) structures the data revealed a significant contribution to the damping. This was related to the presence of the IrMn film especially at the antiferromagnetic to paramagnetic phase transition. We attribute this large enhancement of α to the presence of exchange coupling between NiFe and IrMn, which shall open more conduction channels across the interface and act as spin current amplifier. An analogous non-monotonous behaviour of α versus temperature is captured in Figure 36(a) for NiFe/Cu/IrMn stacks. Though here the enhancement is much less important.

The maximum in spin pumping efficiency comes from the IrMn moments which fluctuate at the magnetic phase transition. The position of this extrinsic damping enhancement is roughly the same for both configurations regardless the nature of the spin transport; electronic or magnonic. For both cases the deduced $T_{\mathrm{crit}}^{\mathrm{IrMn}}$ follows a linear dependence on the thickness of the corresponding IrMn layer. This is in accordance to finite size scaling effects in ultrathin films with magnetic order [139]. Furthermore it confirms the fact that the enhanced spin pumping peak is intrinsic to the antiferromagnet.

Concerning the amplitude of the spin pumping peak, it seems that $\delta\alpha^{p}$ depends on the transport regime. More specifically, we found that it decreases for thicker IrMn thicknesses in the electronic transport regime (NiFe/Cu/IrMn) whereas it remains virtually constant in the magnonic transport regime (NiFe/IrMn). This underlines just how important the nature of spin transport is and the need for further investigations to understand the exact physical mechanisms responsible for this behavior.

The results shown in Figure 36(c)-(d) demonstrate how the resonance field changes as a function of temperature. For the exchange biased stacks (Figure 36(d)) there is a threshold temperature specific to each sample below which the resonance field decreases. This might be interpreted as the onset of exchange coupling between the ferromagnet and antiferromagnet, which gives rise in turn to an additional anisotropy, responsible for the shift of the resonance field (see Eq. II.17); when the temperature decreases, the coupling strengthens and therefore the resonant field reduces. The data obtained for the NiFe/Cu/IrMn structures (Figure 36(c)) showed a slight increase of the resonance field with temperature due to the small decrease of NiFe saturation magnetization, as evidenced in Figure 28 and to the small value of anisotropy constant (5-7 Oe) [113]. The almost negligible increase of the resonance field with temperature further supports the absence of exchange bias coupling between NiFe and IrMn. It is evident that in the case of NiFe/IrMn stacks the exchange coupling plays a crucial role in the transmittance of spin angular momentum. To quantify the exchange bias, we conducted magnetic measurements by taking hysteresis loops at various temperatures using a magnetometer. The experimental results are depicted in Figure 36(e)-(f). The samples where the ferromagnet is exchange coupled to the antiferromagnet showed a measurable exchange bias field, H_E, which increases with the thickness of the antiferromagnet. Note however that the onset of exchange bias should not be confused with the onset of the coupling. In some cases, we observe a zero H_E because the antiferromagnetic moments are dragged by the ferromagnetic moments due to the strong coupling. This may explain why there is no systematic relation between $\delta\alpha^p$ and H_E(5K).

Undoubtedly more systematic work is needed for a complete data interpretation. Currently more data are being collected/interpreted, in the framework of the Post-Doctoral project of Olga Gladii. Theory is also being formulated by K. Yamamoto, J. Sinova and H. Gomonay of the University of Mainz, in the frame of a collaboration.

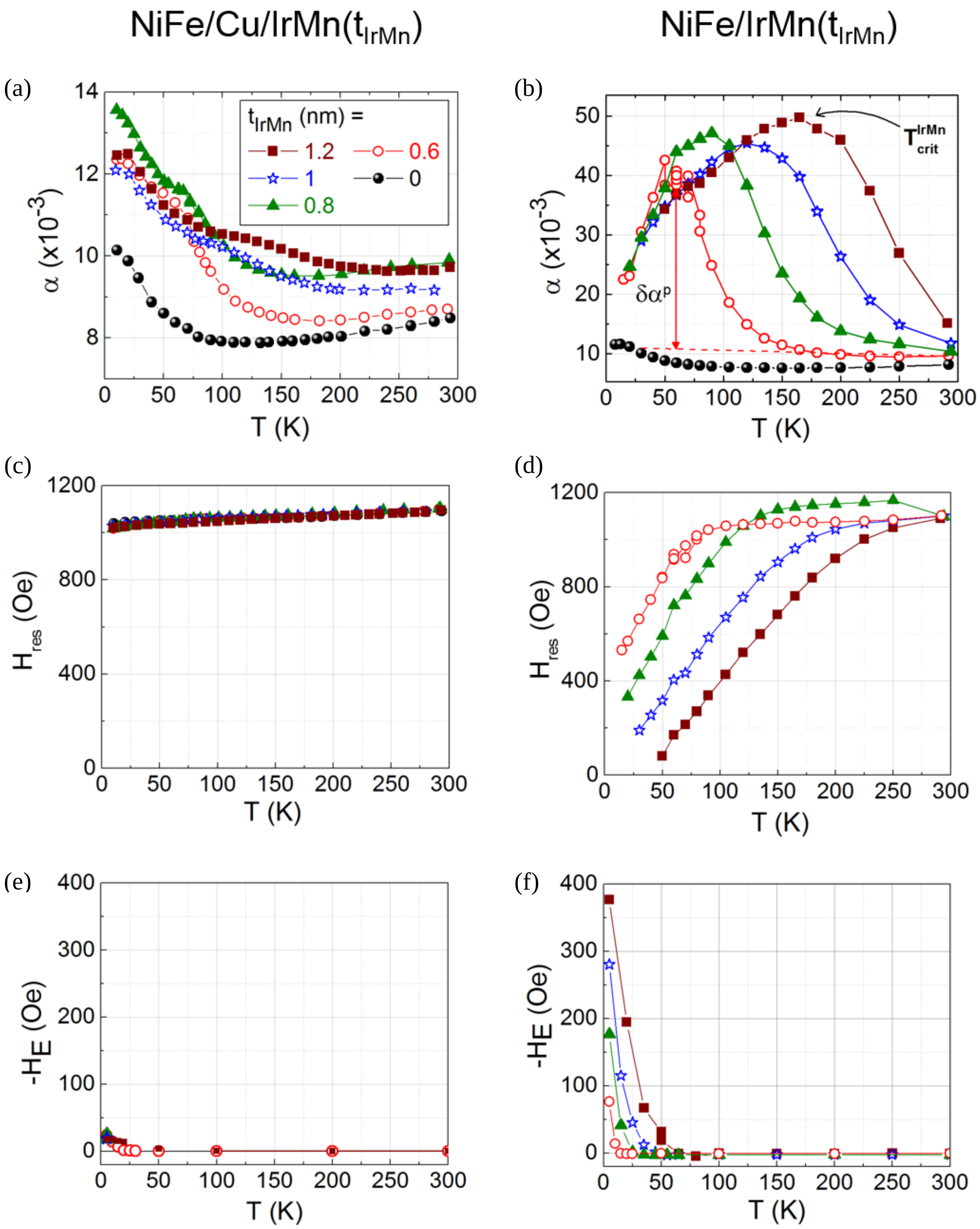

Figure 36 : The temperature dependence of the α Gilbert damping, resonance field and exchange bias of a NiFe ferromagnet (a), (c), (e) directly coupled to a antiferromagnetic IrMn, of various thicknesses; 0.6 to 1.5 nm or (b), (d), (f) separated by a 3-nm-thick Cu layer, respectively.

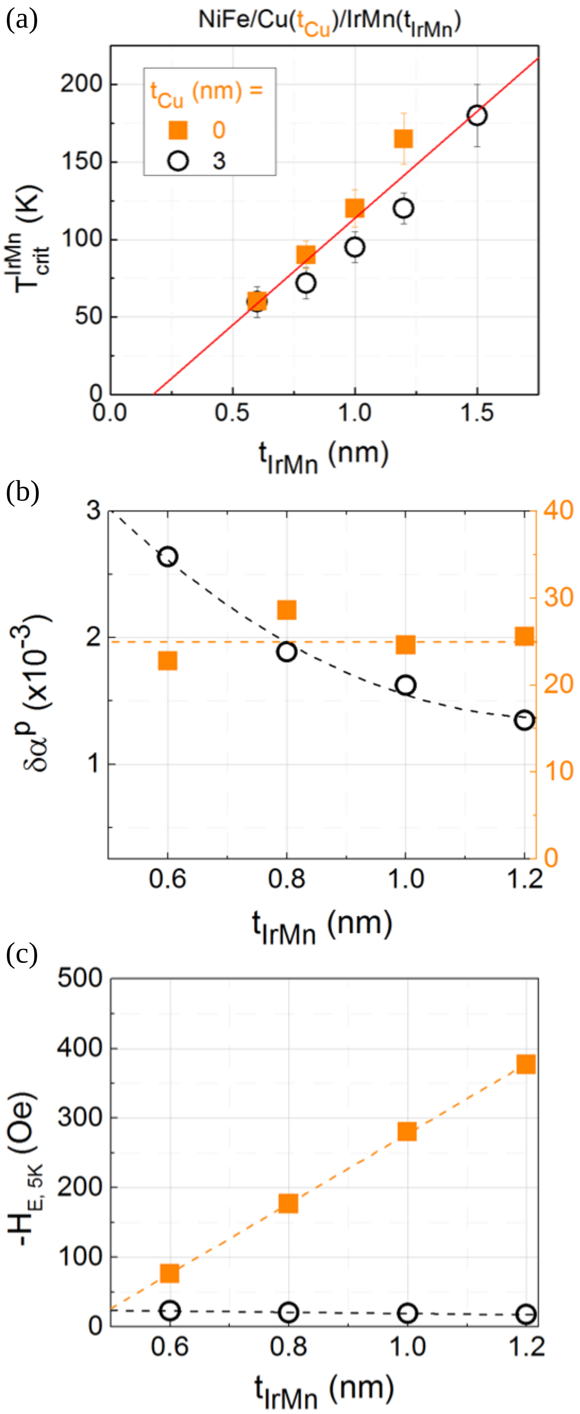

Figure 37 : Antiferromagnetic thickness dependence of: (a) T_{crit}^{IrMn} (b) $\delta\alpha^{p}$ (c) H_E at 5 K, for Si/SiO_2/NiFe8/Cu(t_{Cu})/IrMn(t_{IrMn})/Al2 (nm) stacks.

II.4 Influence of native (antiferromagnetic) interface and surface oxides [3]

This section is adapted from Ref. [3] where the main findings were published.

The previous two subchapters were dealing with spin current absorption in antiferromagnetic IrMn metals. The results obtained highlighted an enhanced spin pumping efficiency around the antiferromagnetic phase transition. Significant amplification of the spin pumping peak was achieved by adding interfacial exchange bias and magnonic spin transport. The aim of the work presented here, is to use the results obtained thus far, to see the relationships among seemingly isolated phenomena. In particular, the goal is to investigate the correlation between native surface-interface oxides and the temperature dependent ferromagnetic relaxation mechanism in NiFe thin films. Inspired by these recent theoretical and experimental findings related to spin-pumping [1,124,138,144–146] , we chose to investigate bare Permalloy (NiFe) in an attempt to determine the incompletely-understood origin of their non-monotonous temperature-dependence of ferromagnetic damping [147–152]. More specifically, typical 3*d* transition metals (Co, Ni, Fe) and associated alloys (including NiFe) frequently show a minimum in the temperature-dependence of their damping [85,153]. As explained in Chapter II.1.2.1 a conductivity-like term related to intraband scattering dominates local intrinsic damping at low temperatures, whereas a resistivity-like term due to interband scattering takes over at higher temperatures [85]. Sometimes for NiFe, a contrasting pronounced maximum was unexpectedly observed in the temperature-dependent [147]. This finding, and the reasons for it, remained controversial and were still being discussed.

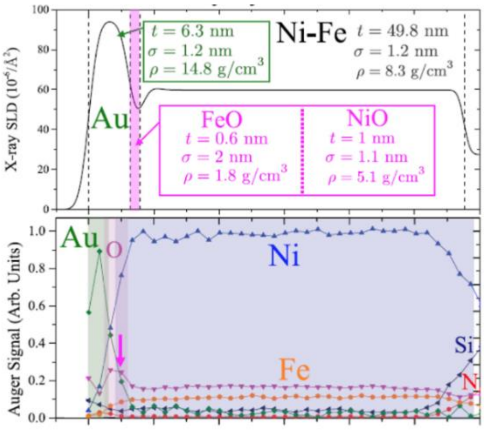

Figure 38 : X-ray scattering-length density and depth-profiled Auger electron spectroscopy for (intentionally) plasma oxidized NiFe-based structure with final composition: Si/SiN/NiFe50/NiFeOx1.6/Au6 (nm). Adapted from Ref. [154].

It has been suggested that the temperature-dependent reorientation of NiFe surface spins from in-plane to out-of-plane could account for the maximum damping observed [149–151]. As reported the surface anisotropy takes over the shape anisotropy at low temperatures pushing the magnetization out of plane giving rise to a maximum in the resonance linewidth. However, recent evidence indicates that spin reorientation may occur at a much lower temperature than the maximum damping [155]. An alternative mechanism was also proposed involving slow relaxation on paramagnetic impurities present in, or adjacent to, the oscillating ferromagnetic material, as [147,148,156,157]. More details on this subject can be found in Chapter II.1.2.2. In fact, if not protected from oxidation due to exposure to air, a few monolayers of the NiFe layer will naturally oxidize to form a passivating oxide layer (NiFeOx). Figure 38 shows the X-ray scattering-length density and depth-profiled Auger electron spectroscopy for an intentionally oxidized NiFe sample. The results point out the existence of the oxidized interface consisting of a complex mixture of NiO and FeO antiferromagnetic alloys with variable stoichiometry gradients [154].

In this context, the potential influence of relaxation of interface paramagnetic impurities in bilayers where a ferromagnet is exchange-biased to an antiferromagnet was considered in several studies [93–95,158]. However, the results of these studies led to divergent mechanisms being presented to explain the temperature-dependence of the relaxation rate for impurities [93–95,158] (see also section II.4.3. below). Beyond paramagnetic impurities or exchange-bias interactions, the presence of NiFe antiferromagnetic surface oxides raises the question of how spin angular momentum is absorbed by the antiferromagnetic layer itself [98,125]. In this process, transfer/sink and propagation of spin angular momentum involves magnons from the oscillating ferromagnet feeding into the entire antiferromagnet, due to magnetic coupling [27,28]. The end result is an overall enhancement of the total damping of the ferromagnet [98,125]. In addition, as we have already seen in section II.3, near the phase transition for the magnetic order of the antiferromagnetic layer, i.e., around its Néel temperature, the magnetic fluctuations lead to a maximum spin-pumping efficiency [1,138,145]. Here we investigate whether enhanced spin angular momentum absorption at the magnetic phase transition of native interface- and surface-oxidized layers could be an alternative mechanism explaining the temperature-dependent ferromagnetic relaxation of ‘bare’ NiFe.

II.4.1 Samples deposition, structural and magnetic characterizations

Samples deposition

We examined temperature-dependent ferromagnetic relaxation in NiFe thin films, and how it was affected by native oxidation of the NiFe layer and the number of native oxide layers surrounding the NiFe (two, one or none). Spin-pumping experiments were performed at various temperatures on a first series of samples consisting of Si/$SiO_2$500/NiFe8 (short name: Si/SiO_2/NiFe), Si/$SiO_2$500/NiFe8/Cu3/Al2 (short name: Si/SiO_2/NiFe/Cu/Al), Si/$SiO_2$500/Cu6/NiFe8 (short name: Si/SiO_2/Cu/NiFe) and Si/$SiO_2$500/Cu6/NiFe8/Cu3/Al2 (short name: Si/SiO_2/Cu/NiFe/Cu/Al) multilayers. All thicknesses are given in nanometers. Stacks were deposited at SPINTEC by Stéphane Auffret on thermally oxidized silicon substrates [Si/$SiO_2$500] at room temperature by dc-magnetron sputtering. The NiFe layer was deposited from a Permalloy target [$Ni_{81}Fe_{19}$ (at. %)]. An Al(2) cap was added, forming a protective passivating AlOx film, to block oxidization by air in some samples. The other samples were exposed to air. Data recorded after a week and after a month overlapped, indicating that oxidation has reached a maximum after a week. Uncapped layers were therefore exposed to air for a minimum of one week before any measurements were performed.

Note that, like in section II.2.5, the thickness of the Cu buffer layer (Cu6 between SiO_2 and NiFe) had to be optimized. More about that will be presented in section II.5.

Structural characterization

Transmission electron microscopy (TEM) analysis (Figure 39) was used to view oxidation of the NiFe layer in the Si/SiO_2/NiFe stack. After exposure to air, some sample pieces were capped with Pt in preparation for the TEM experiment. This cap protects the sample's surface from damage during the thinning and polishing steps required for TEM. It also enhances the TEM contrast around the sample surface. Results of the TEM investigations indicated a NiFe surface oxide (NiFeOx) produced by NiFe oxidation in air. The thickness of the NiFeOx surface oxide, as determined from the TEM data was approximately 1.6 ± 0.2 nm. The margin of error corresponds to typical errors in thickness measurements performed at various locations in TEM images. The NiFeOx thickness value is in line with data from the literature, where passivating surface oxides were reported to measure nanometers thick [152,154,159] (see also Figure 38).

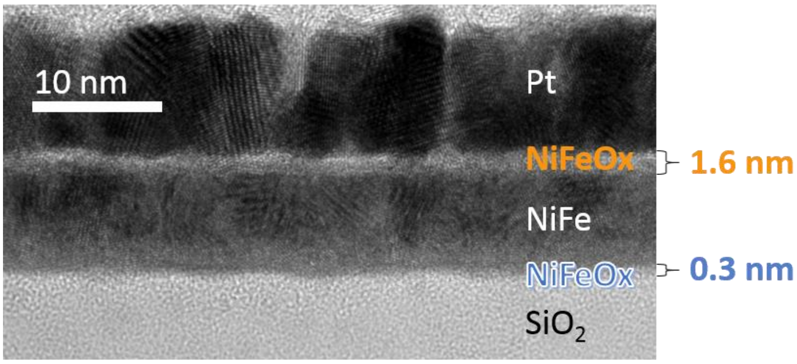

Figure 39 : Transmission electron microscopy image (TEM) for a Si/SiO_2/NiFe sample. From Ref. [3]. The TEM measurement was subcontracted to SERMA technologies.

Results from energy dispersive x-ray spectroscopy (EDX) measurements (Figure 40) confirm the presence of a surface-oxidized layer and reveal the presence of another native oxidized layer at the interface between the SiO_2 and NiFe layers. This lower oxide layer was not visible in the TEM image due to a lack of contrast with the SiO_2 underlayer. Unlike the top oxide, this bottom oxide is not produced due to oxidation in air. Rather, it forms naturally at the SiO_2/NiFe interface, likely activated by the Ni and Fe atoms when they interact with the SiO_2 surface during sputter deposition. The presence and thickness (around 0.3 ± 0.2 nm) of this bottom oxide layer was determined from the horizontal shift in the oxygen and silicon traces in EDX data (visible in Figure 40). Indeed, Figure 40 represents atomic weight as a function of sample depth. Since the O signal rises before the Si signal, some oxygen atoms must have mixed with the NiFe layer. The shift between the Si and O traces along the sample depth corresponds to the thickness of this bottom NiFeOx layer. The margin of error corresponds to typical errors reported for EDX data due to measurements performed at different locations in the film.

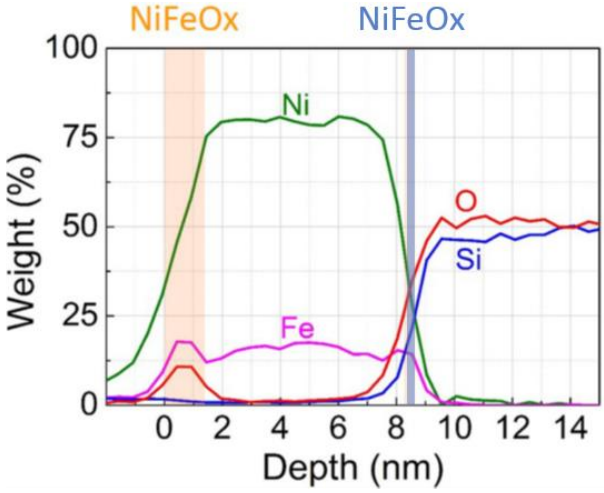

Figure 40 : Energy-dispersive x-ray spectroscopy (EDX) data for a Si/SiO_2/NiFe sample. From Ref. [3]. The EDX measurement was subcontracted to SERMA technologies.

From the EDX data, we also calculated that in the SiO_2/NiFe sample, the Ni and Fe atoms extend over a total thickness of around 8.1 ± 0.2 nm. Complementary EDX measurements performed on a Si/SiO_2/NiFe/Cu/Al sample, where the NiFe layer was not air-oxidized, indicated that the Ni and Fe atoms also extend over a total thickness of around 8 ± 0.3 nm. This observation suggests negligible expansion of the lattice parameter for the oxide layer in Si/SiO_2/NiFe samples. The margins of error reported here give an estimate of the typical error level between nominal and actual thickness. To sum up, from the TEM and EDX experiments we can conclude that the initial Si/SiO_2/NiFe, Si/SiO_2/NiFe/Cu/Al, Si/SiO_2/Cu/NiFe and Si/SiO_2/Cu/NiFe/Cu/Al multilayers are in fact the following stacks Si/SiO_2/NiFeOx(0.3)/NiFe/NiFeOx(1.6), Si/SiO_2/NiFeOx(0.3)/NiFe/Cu/AlOx, Si/SiO_2/Cu/NiFe/NiFeOx(1.6) and Si/SiO_2/Cu/NiFe/Cu/AlOx, respectively.

Magnetic characterization

We next investigated the magnetic nature of the surface-oxidized layers by measuring hysteresis loops at various temperatures using a magnetometer (Figure 41). These results show a loop shift (H_E) along the axis of the magnetic field, demonstrating magnetic exchange-bias interactions [15,16] between the NiFe ferromagnetic layer and the NiFeOx surface-oxidized layer. These data confirmed the antiferromagnetic nature of the top surface-oxidized layer. The data presented in Figure 42 further indicated that H_E decreases as the temperature rises. The ferromagnetic/antiferromagnetic blocking temperature (T_B) can be extracted from H_E vs. T by determining the temperature at which H_E vanishes [15,16]. T_B is expected to be much smaller than the critical temperature (T_{crit}) for the antiferromagnetic to paramagnetic transition [15,16], and for exchange bias interactions with the top NiFeOx(1.6) layer, it was found to be about 15K (see data for the Si/SiO2/Cu/NiFe and Si/SiO2/NiFe samples). This relationship can be explained as T_B is linked to the interfacial exchange interactions between the ferromagnet and the antiferromagnet, whereas T_{crit} relates to the exchange stiffness between all antiferromagnetic moments.

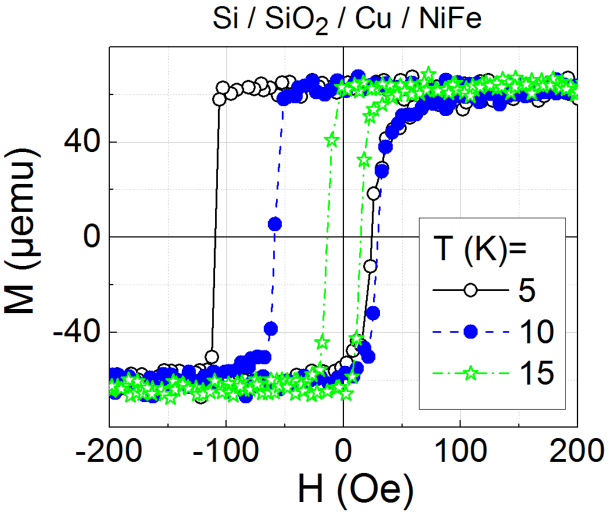

Figure 41 : Representative magnetization (M) vs field (H) hysteresis loops at different temperatures for a Si/SiO2/Cu/NiFe sample. From Ref. [3].

For exchange bias interactions with the lower NiFeOx(0.3) layer (see data for the Si/SiO2/NiFe/Cu sample), T_B was determined to be sub-K. Its value could not be measured based on the data shown in Figure 42 due to the fact that the lower NiFeOx(0.3) oxide layer is very thin and displays a reduced T_{crit}. Note that for the ultra-thin NiFeOx(0.3) layer, T_{crit} probably describes a frozen to liquid spin transition. Results confirming the reduced value of T_{crit} will be discussed below.

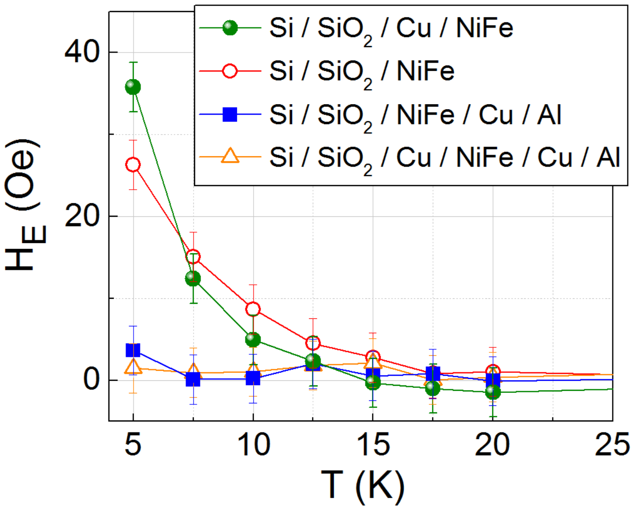

Figure 42 : Temperature dependence of the hysteresis loop shift, H_E. The existence of the exchange bias for the two samples where NiFe was air-oxidized confirm the antiferromagnetic nature of the forming oxide. From Ref. [3].

II.4.2 Enhanced spin pumping with “bare” NiFe ferromagnetic thin films

Gilbert damping was determined from spin pumping experiments as in section II.1.3. Figure 43 shows α plotted against temperature. The pronounced maximum at T = 70 K corresponds to the top NiFeOx(1.6) layer resulting from natural oxidation in air (see data for the Si/SiO_2/NiFe and Si/SiO_2/Cu/NiFe samples). The amplitude of this maximum was 3-fold the amplitude measured at 300 K. A less pronounced contribution is visible at lower temperatures in samples containing the bottom NiFeOx(0.3) layer, where the NiFe become naturally oxidized due to contact with the SiO_2 layer (see data for the Si/SiO_2/NiFe/Cu/Al sample). When the NiFe layer was isolated from oxygen atoms on both sides (in the Si/SiO_2/Cu/NiFe/Cu/Al sample) no such maximum were observed.

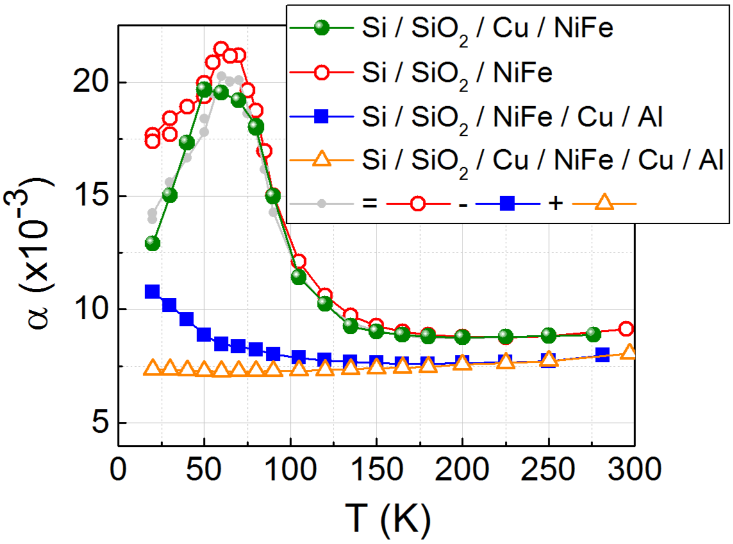

Figure 43 : Temperature dependence of the NiFe layer Gilbert damping. The NiFe layer is surrounded by two, one, or no native oxide layers. When the NiFe is deposited directly on Si/SiO_2 a 0.3-nm-thick NiFeOx naturally forms at the Si/SiO_2/NiFe interface, activated by the Ni and Fe atoms when interacting with the SiO_2 surface during sputter deposition. When the NiFe layer is left uncapped it naturally undergoes oxidation due to contact with air, resulting in a 1.6-nm-thick NiFeOx surface layer. From Ref. [3].

Since the oxidized layers are magnetic, the NiFe damping is the sum of local intrinsic damping (α^0) and additional non-local damping ($\alpha^{p,i}$) associated with the surface/interface NiFeOx oxide(s) acting as a spin absorber for angular momentum. The temperature-dependence of α can thus be expressed as: $\alpha(T)=\alpha^0(T)+\sum_i \alpha^{p,i}(T)$ [98,124,125], where i accounts for the uppermost and/or lowermost NiFeOx spin absorber. Data obtained with the Si/SiO_2/Cu/NiFe/Cu/Al sample (no spin absorber) give the temperature-dependence of the local intrinsic NiFe Gilbert damping [$\alpha_{SiO_2/Cu/NiFe/Cu/Al}(T)=\alpha^0(T)$] with a detectable conductivity-to resistivity-like progression [85,153]. From Figure 43, we can thus conclude that the temperature-dependence of α^0 can be neglected, but that $\alpha^{p,i}$ is highly temperature-dependent. We recall that the non-local damping is related to the spin mixing conductance across the NiFe/NiFeOx(1.6) and/or NiFeOx(0.3)/NiFe interfaces (g_s^i) as presented in [124] by:

$$\alpha^{p,i}(T) = \frac{1}{S_0 N_{SI}} g_s^i(T), \text{ where } g_s^i(T) = \frac{2J_{sd}^2 S_0^2 N_{\text{int}}}{\hbar^2 N_{SA}^i} \sum_k \frac{1}{\Omega_{rf}} \operatorname{Im} \chi_k^{R,i}\left(\Omega_{rf}, T\right) \quad \text{(Eq. II.27 and 28),}$$

which in turn is linked to temperature-dependent dynamic spin susceptibility of the spin absorber represented by $\chi_k^{R,i}\left(\Omega_{rf}, T\right)$. As a result, the non-local damping is given by:

$$\alpha^{p,i}(T) = \frac{2J_{sd}^2 S_0 N_{\text{int}}}{\hbar^2 N_{SA}^i N_{SI}} \sum_k \frac{1}{\Omega_{rf}} \operatorname{Im} \chi_k^{R,i}\left(\Omega_{rf}, T\right) \quad \text{(Eq. II.29).}$$

As seen already in Chapter II.2, the spin susceptibility of antiferromagnetic materials displays a maximum around the critical temperature for the magnetic phase transition due to magnetic fluctuations. This transition results in enhanced spin mixing conductance across the interface (g_s^i). In other words, magnetic fluctuations in the spin absorber open more conduction channels across the interface, which translates into enhanced spin angular momentum absorption ($\alpha^{p,i}$) and therefore into maximal NiFe total damping (α), as observed in Figure 43. From data for Si/SiO$_2$/Cu/NiFe, where $\alpha_{SiO_2/Cu/NiFe}(T) = \alpha^0(T) + \alpha^{p,NiFeOx(1.6)}(T)$, we deduced the Néel temperature for the magnetic phase transition of the top 1.6-nm-thick NiFeOx oxide, at approximately 70 K. From the Si/SiO$_2$/NiFe/Cu/Al in Figure 43, where $\alpha_{SiO_2/NiFe/Cu/Al}(T) = \alpha^0(T) + \alpha^{p,NiFeOx(0.3)}(T)$, we concluded that the critical temperature for the phase transition of the lowermost 0.3-nm-thick NiFeOx oxide, which formed naturally at the interface between the NiFe and SiO$_2$ layers, is less than 20 K. We infer that this temperature is actually well below 20 K, and probably sub-K since the amplitude of the damping peak for the 0.3-nm-thick NiFeOx oxide is expected to be 5-fold (1.6/0.3) that of the 1.6-nm-thick oxide. We recall that that this difference can be explained by the fact that α^p is inversely proportional to the number of lattice sites in the spin absorber (N_{SA}). Finally, data for the SiO$_2$/NiFe sample relate to $\alpha_{SiO_2/NiFe}(T) = \alpha^0(T) + \alpha^{p,NiFeOx(0.3)}(T) + \alpha^{p,NiFeOx(1.6)}(T)$. From the four relations above between $\alpha_{SiO_2/NiFe}$, $\alpha_{SiO_2/NiFe/Cu/Al}$, $\alpha_{SiO_2/Cu/NiFe/Cu/Al}$, $\alpha_{SiO_2/Cu/NiFe}$ and α^0, $\alpha^{p,NiFeOx(0.3)}$, $\alpha^{p,NiFeOx(1.6)}$ our experimental data should confirm the following equation: $\alpha_{SiO_2/NiFe} - \alpha_{SiO_2/NiFe/Cu/Al} + \alpha_{SiO_2/Cu/NiFe/Cu/Al} = \alpha_{SiO_2/Cu/NiFe}$. The data shown in Figure 43 clearly confirm the equation, where the small grey filled circles ($\alpha_{SiO_2/NiFe} - \alpha_{SiO_2/NiFe/Cu/Al} + \alpha_{SiO_2/Cu/NiFe/Cu/Al}$) satisfactorily overlap the green circles ($\alpha_{SiO_2/Cu/NiFe}$). This verification further supports absorption of spin angular momentum at the magnetic phase transition of the native surface-oxidized layers as an alternative mechanism explaining the temperature-dependent ferromagnetic relaxation of bare NiFe, while also indicating satisfactory reproducibility of data and native oxidation from sample to sample.

We note here that it is essential that transfer and propagation of spin angular momentum directly involves magnonic transport. In other words, the NiFeOx must be fed by spin waves through direct magnetic coupling with NiFe. The difference in spin pumping efficiency by a ~ 1.6 nm thick antiferromagnetic NiFeOx directly coupled to NiFe, or separated from the ferromagnetic NiFe layer by a 3-nm-thick Cu layer is shown in Figure 44. The enhanced damping at 70 K due to the magnetic phase transition of the NiFeOx is clearly observed in the case of direct magnonic transport but is suppressed when the Cu breaks the direct magnetic interaction between NiFe and NiFeOx. In the latter case, we recall that spin transport is mediated by a purely electronic transport regime through Cu. As the spin diffusion length for Cu is much longer than 3 nm, spin propagation will not be altered by passing through this layer. However from the data shown in Figure 44 virtually no spin angular momentum is transmitted to the NiFeOx. The presence of intermediate copper oxide at the Cu/NiFeOx interface cannot be excluded and may also account for the overall increase of α.

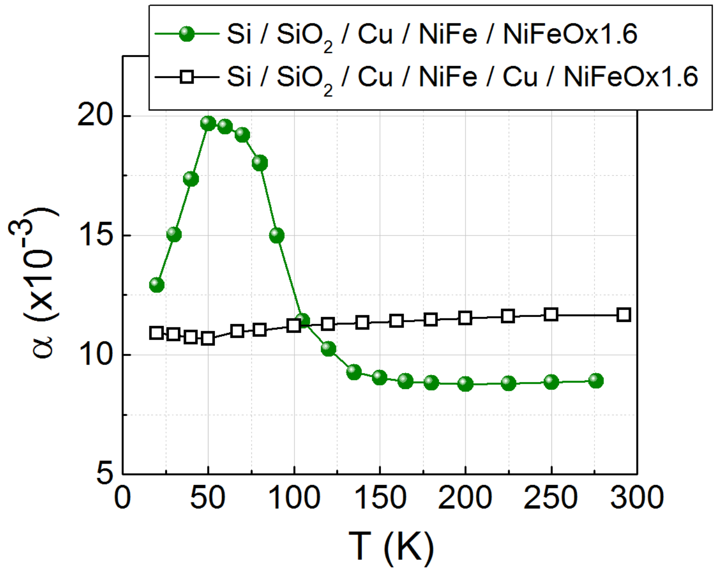

Figure 44 : Temperature dependence of damping of a NiFe ferromagnet directly coupled to a 1.6-nm-thick antiferromagnetic NiFeOx or separated by a 3-nm-thick Cu layer. In the $Si/SiO_2/Cu/NiFe/NiFeOx$ sample, NiFeOx results from the native oxidation of NiFe(8 nm), creating a passivating 1.6-nm-thick layer. In the $Si/SiO_2/Cu/NiFe/Cu/NiFeOx$ sample, NiFeOx results from complete native oxidation of a NiFe(1.6 nm) layer. From Ref. [3].

II.4.3 Discarding the slow-relaxation mechanism

An alternative mechanism to the one proposed by Ohnuma *et.al* [124] (see section II.2.2 and II.4.2) was reported earlier to explain the pronounced maximum observed in the temperature-dependent damping of NiFe. It involved slow relaxation (see section II.1.2.2) due to thermal reversal of the antiferromagnetic grains [93–96,158,160], with a relaxation rate described by the Néel-Arrhenius equation as:

$$\tau = \tau_0 \exp(E/k_B T) \qquad \text{(Eq. II.30)},$$

where τ_0 is the attempt frequency, k_B is the Boltzmann constant and E is the height of the energy barrier. In a simplified form the slow-relaxation theory predicted the following relation:

$$\frac{2\delta(H_{res})}{\delta(\Delta H)} = -\omega\tau \qquad \text{(Eq. II.31)}.$$

Figure 45(a) indicates that only the samples containing the native NiFeOx(1.6) surface oxide show an abrupt decrease of the resonance field. The latter is associated to the onset of exchange bias anisotropy below the Néel temperature (considering the Kittel formula (Eq. II.17), an increase in K indeed reduces the H_{res}). Figure 46 (log-plot) shows that the relaxation rate does not follow the Néel-Arrhenius law, Eq. II.30, meaning that the slow relaxation mechanism due to thermal reversal of antiferromagnetic grains cannot be the origin of the maximum observed in the temperature-dependent damping.

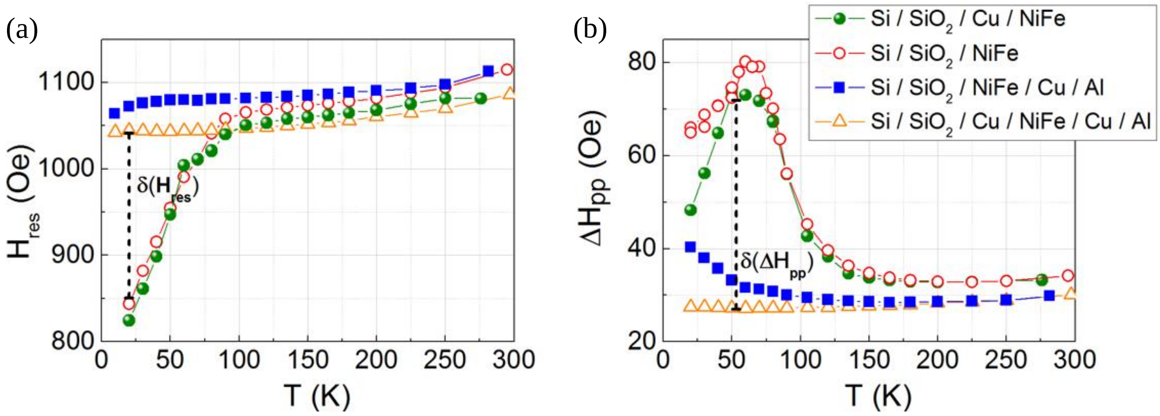

Figure 45 : The temperature dependence of: (a) the resonance field as a function of temperature and (b) the resonance linewidth.

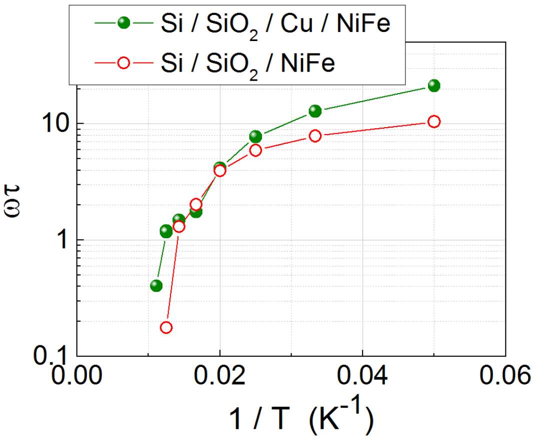

Figure 46 : ωτ versus 1/T (log-plot), where ω is the excitation angular frequency and τ is the relaxation time for $Si/SiO_2/Cu6/NiFe8$ and $Si/SiO_2/NiFe8$ samples.

II.4.4 Finite size effects

Like for IrMn, we took advantage of the findings to further investigate how T_{crit} is influenced by the thickness of the native oxide. Spin pumping experiments were performed at various temperatures on a second series of samples, where NiFe(t_{NiFe}) layers were grown on Si/SiO$_2$, naturally oxidized by air for a week before adding another NiFe(8) layer, which was left uncapped. t_{NiFe} is the thicknesses of the bottom NiFe layer (0.5, 1, or 1.5 nm). Based on the results presented above, the lowermost NiFe layer is expected to be fully oxidized in air. The samples therefore consisted of a Si/SiO$_2$/NiFeOx(t_{NiFeOx})/NiFe/NiFeOx(1.6) with nominal t_{NiFeOx} = 0.5, 1, or 1.5 nm.

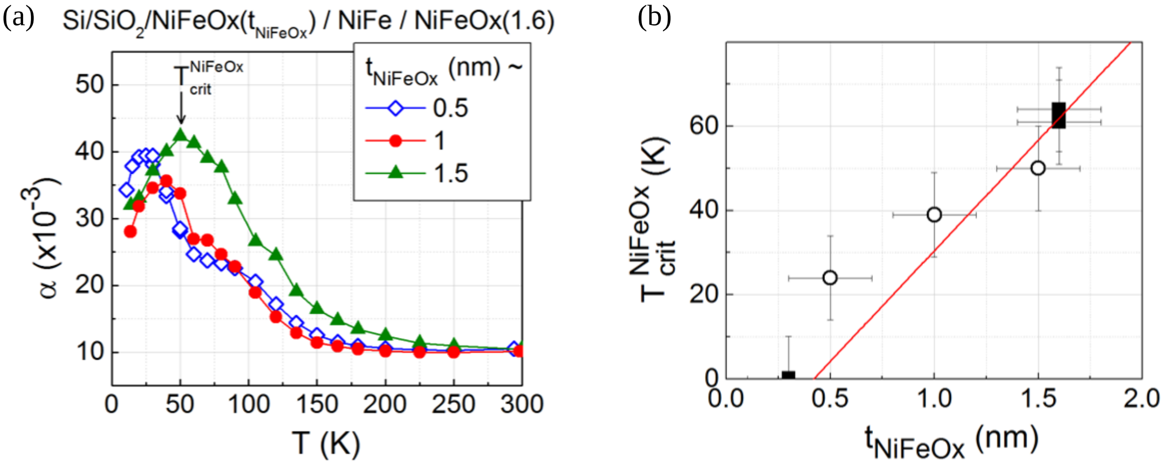

Figure 47 : (a) Temperature dependence of the Gilbert damping of the NiFe layer on temperature in Si/SiO$_2$/NiFeOx(t_{NiFeOx})/NiFe/NiFeOx(1.6) (nm) multilayers. The arrow indicates the maximum absorption of spin angular momentum at the magnetic phase transition of the forming oxides, which translates into T_{crit}^{NiFeOx}. (b) Thickness dependence of the critical temperature for the magnetic phase transition of the oxidized NiFe layer. Open circles represent data deduced from Figure 47(a). Full squares represent data deduced from Figure 43. Line fitting was based on the equation presented by Zhang et al. [139] in the thin-layer regime for a (NiO)$_{81}$(FeO)$_{19}$ alloy. From Ref. [3].

Analogous to the "double IrMn" case, discussed earlier in Chapter II.2, we can say that the NiFe layer is influenced by two spin angular momentum absorbers, and its damping will correspond to the sum of local intrinsic damping, non-local extrinsic damping due to spin absorption by the lower NiFeOx(t_{NiFeOx}), and non-local extrinsic damping due to spin absorption by the upper NiFeOx(1.6) layer: $\alpha(T) = \alpha^0(T) + \alpha^{p,NiFeOx(t_{NiFeOx})}(T) + \alpha^{p,NiFeOx(t_{1.6})}(T)$. Due to fluctuations of the antiferromagnetic order, $\alpha^{p,NiFeOx(t_{NiFeOx})}(T)$ and $\alpha^{p,NiFeOx(t_{1.6})}(T)$ are expected to show a maximum at the magnetic phase transition for the NiFeOx(t_{NiFeOx}) and NiFeOx(1.6) layer, respectively. Figure 47(a) shows α plotted against temperature for these multilayers. The data indicate two contributions to α for samples containing the 0.5- and 1-nm thick lowermost NiFeOx layers. In line with the results presented above, the contribution (shoulder) at around 70 K corresponds to the magnetic phase transition of the uppermost

NiFeOx(1.6) layer. The expected maximum in damping actually overlaps with the tail of the peak that can be observed at lower temperatures (at around 25 and 40 K for t_{NiFeOx} = 0.5 and 1 nm, respectively). The peak at the lower temperature corresponds to the magnetic phase transition of the lowermost NiFeOx(0.5 or 1) layer. From Figure 47(a), we observe that the contribution of the phase transition of the lower layer shifts towards higher temperatures as its thickness increases. With the Si/SiO_2/NiFeOx(1.5)/NiFe/NiFeOx(1.6) sample, the NiFe is sandwiched between two similar NiFeOx layers. The top and bottom NiFeOx layers in the Si/SiO_2/NiFeOx(1.5)/NiFe/NiFeOx(1.6) sample therefore absorb similar amounts of spin current on both sides ($\alpha^{p,NiFeOx(1.5)}(T) \sim \alpha^{p,NiFeOx(1.6)}(T)$) and share a similar T_{crit}, around 70 K, as previously deduced for the NiFeOx(1.6) layer (Figure 47(b)). As a result, the peaks corresponding to the magnetic phase transitions for the top NiFeOx(1.5) and bottom NiFeOx(1.6) layers overlapped. The peak's amplitude for the Si/SiO_2/NiFeOx(1.5)/NiFe/NiFeOx(1.6) sample with two similar spin absorbers (Figure 47(a)) was effectively close to twice the amplitude of the peak for the Si/SiO_2/Cu/NiFe/NiFeOx(1.6) sample (nominal Si/SiO_2/Cu/NiFe in Figure 43). Satisfactory reproducibility of data and native oxidation can also be concluded from these data.

Figure 47(b) illustrates how the critical temperature for the NiFeOx layer, regardless of its actual nature, is directly proportional to its thickness. This linear relationship is in line with theories on finite size scaling of magnetic phase transitions [139,161] (see section II.2.3). This corroboration of theory supports the fact that what we actually measured is the result of a magnetic phase transition of the NiFeOx layer, which was formed by natural oxidation of NiFe. Unfortunately, our data cannot be readily fitted to the model because the actual nature of the NiFeOx layer is complex, as it is composed of a mixture of different phases including NiO and FeO alloys (see Figure 38)and variations in thickness due to the oxidation rate [152]. Nor can cluster formations be excluded. The red line in Figure 47(b) represents a fit for the $Ni_{81}Fe_{19}Ox$ layer determined by considering it as a $(NiO)_{81}(FeO)_{19}$ alloy (approximately proportional to the initial Ni-to-Fe 20/80 atomic ratio). We used $T_N(bulk)=0.81T_{N,NiO}(bulk)+0.19T_{N,FeO}(bulk)$ for fitting, with $T_{N,NiO}(bulk)$ = 520 K, $T_{N,FeO}(bulk)$ = 200 K, $d=0.81d_{NiO}+0.19d_{FeO}$, d_{NiO} = 0.417 nm, and d_{FeO} = 0.433 nm. This fit is shown to give the reader an idea of what such a simple and straightforward assumption would give. The fit agreed with our data to a satisfactory extent, and returned n_0 = 4.4 nm (approximately ten monolayers), which is typical for ordered magnetic films [152].

II.4.5 Comparison to spin pumping by a controlled antiferromagnetic oxide: NiO

In order to show that the obtained results correlate well with what has been already reported in the literature, we present data for NiO which is an antiferromagnetic insulator. A growing body of literature has investigated experimentally its spin current absorption as a function of temperature using different experimental techniques [122,138,145]. Its finite size effects have also been studied [131,138,145,161–163] by means of nanocalorimetry or by means of susceptibility measurements.

Figure 48(a) shows our measurements of the temperature dependence of Gilbert damping for Si/SiO_2/Ta3/NiO(t_{NiO})/NiFe7/Cu3 (nm) stacks. It should be noted here that the samples were sputter-deposited by David Spenato of the OPTIMAG in Brest. Following the procedure used in section II.2.3 and II.4.4, we extracted T_{crit}^{NiO} for the various NiO thicknesses which are represented by red squares in Figure 48(b). Satisfactory agreement is found between the theoretical model proposed by Zhang and Willis [139] (dashed line) and the experimental results, indicating that the enhanced spin pumping occurs at the magnetic phase transition of the antiferromagnet.

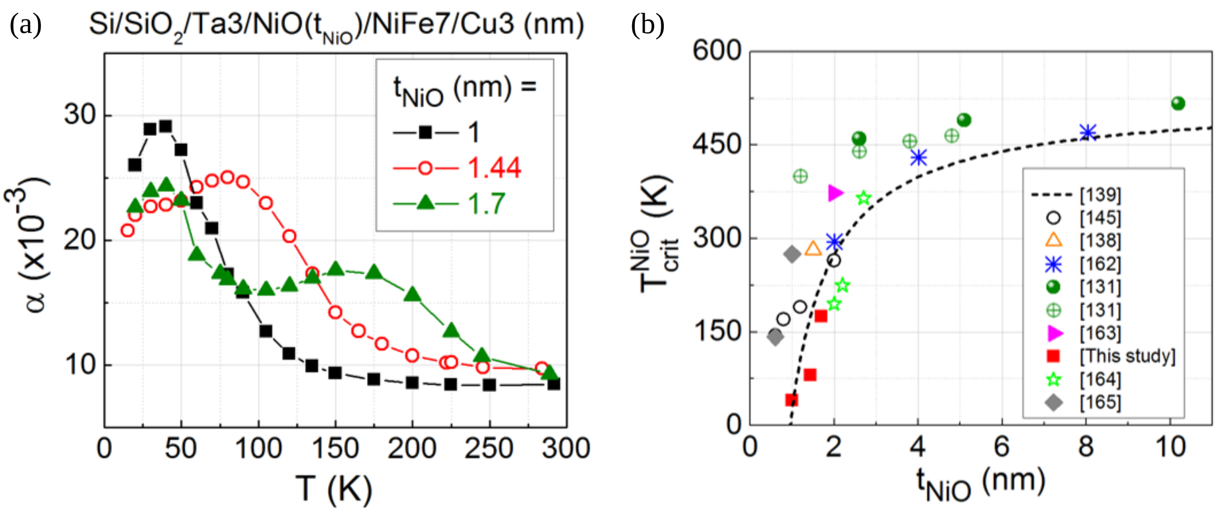

Figure 48 : (a) α Gilbert damping versus temperature. (b) Comparison of T_{crit}^{NiO} as function of NiO thickness between the model predictions and the available experimental evidences, where the data are extracted from different experimental techniques. The close squares correspond to our spin pumping experiments. The line is a fit based on Zhang et al. [139]. The fit returned a spin-spin correlation length of n_0 =1.67 nm, in agreement with Ref. [131,161].

II.5 Side study about the influence of buffer layer on surface anisotropy and eddy currents [4]

For our investigations it was crucial to understand the intrinsic Gilbert damping of NiFe. NiFe was chosen intentionally as the spin injector, on account of the fact that it presents a sufficiently low intrinsic damping, well suited for our purpose. Nonetheless, we should not neglect any extrinsic contributions that could add to the total α Gilbert damping and if possible we shall eliminate them. Figure 49 is an example of how extrinsic contributions may come into play in our previous experiments.

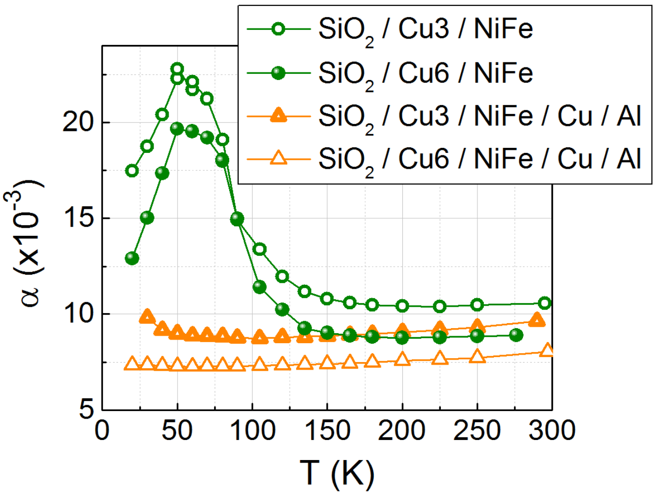

Figure 49 : Influence of Cu buffer thickness (nm) on the temperature, T dependence of NiFe Gilbert damping, α.

The figure shows that simply increasing the thickness of the Cu buffer layer is enough to reduce the overall NiFe Gilbert damping. Nonetheless, despite the overall shift of the Gilbert damping towards lower values for the samples where NiFe layer was left uncapped, the spin pumping peak attributed to the magnetic phase transition of NiFeOx (see II.4) is not affected. Note that a further increase of the Cu layer thickness does not change the overall Gilbert damping.

In this context, we systematically studied the relaxation properties of NiFe thin films in stacks consisting of; $SiO_2/Cu(t_{Cu})/NiFe/Cu/Al$, referred to as Cu^{buffer} and $SiO_2/NiFe/Cu(t_{Cu})/Al$ named as $Cu^{capping}$, where t_{Cu}=1-14 nm [4]. The second series of samples is used as a reference. FMR spectra measurements were carried out by using a coplanar waveguide setup, depicted in Figure 50(a)), which revealed a non-monotonous dependence of Gilbert damping with Cu buffer-layer thickness (Figure 50(d)). Furthermore, measurements of the resonance spectra position indicated a shift of the resonance peak towards lower magnetic fields, when thicker Cu^{buffer} layers were considered (Figure 50(b)). It is noteworthy that varying the capping layer thickness has virtually no influence on either Gilbert damping or resonance frequency.

We first attributed the non-monotonous dependence of Gilbert damping and resonance frequency on the Cu buffer-layer thickness to the non-monotonous changes in Cu/NiFe interface roughness. It is well known that Cu wets poorly on SiO_2 compared to NiFe on SiO_2 and NiFe on Cu. In practice, roughness creates spatially inhomogeneous stray fields that result in strong incoherent dephasing of the spin current, injected from the NiFe to the Cu layer, leading to damping enhancement (see Chapter II.1). The latter can be also described by means of two-magnon scattering, where a defect scatters an incident magnon (k=0) into degenerate modes (k≠0) and contributes subsequently to the overall linewidth. Interface roughness is a leading source of two-magnon scattering.

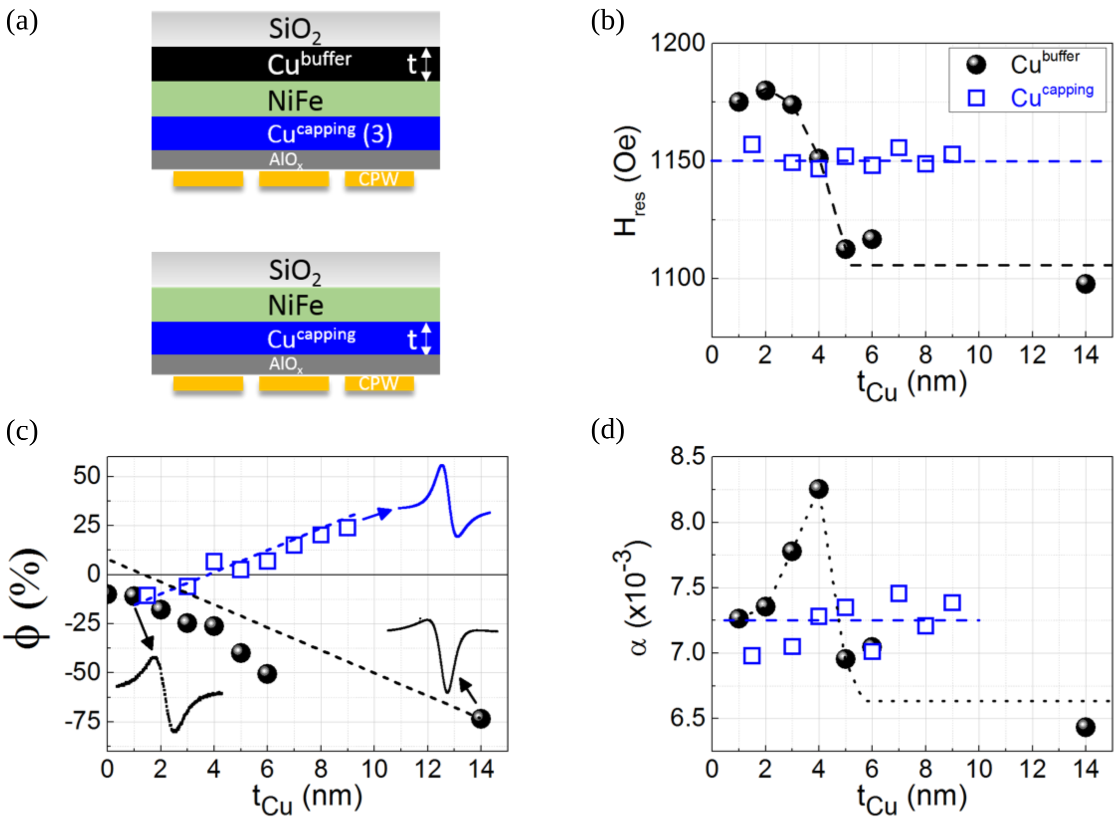

Figure 50 : (a) Schematic representation of the coplanar waveguide (CPW) – ferromagnetic resonance experiment. The sample is placed face down on the waveguide. (b)-(d) Dependence of Gilbert damping (α), resonance field (H_{res}) and spectrum asymmetry (ϕ) on capping (full circles) and buffer (open squares) Cu layer thickness, respectively. In (c) the asymmetry is given in percentage, where 0% corresponds to completely symmetric spectrum and 100% indicates completely asymmetric spectrum.

In an attempt to estimate the interface roughness between Cu layer adjacent to NiFe and SiO_2 we subcontracted transmission electron microscopy experiments (TEM) for selected samples: Si/SiO_2/NiFe8, Si/SiO_2/NiFe8/Cu3/IrMn0.6/Al2, and Si/SiO_2/Cu4/NiFe8/Cu3/Al2. The results are depicted in Figure 51. The actual composition of the films (after the various natural oxidations, see Chapter II.4) is given in Table 2 along with the interfaces roughness. Note that TEM allows for recording interfaces with sufficient contrast in Z (i. e. metal/oxide interfaces in our case).

The results displayed in Table 2 allows us to conclude that the changes in roughness between the different samples are marginal. Thus roughness cannot be used here to explain our experimental observations. It is noteworthy that, for all samples cumulative effects make the top interface rougher than the bottom one. Further investigations are being carried out in the framework of the Post-doctoral project of Olga Gladii. In particular, systematic surface anisotropy measurements are being conducted, as well as thickness dependence experiments, in an effort to disentangle how surface properties come into play.

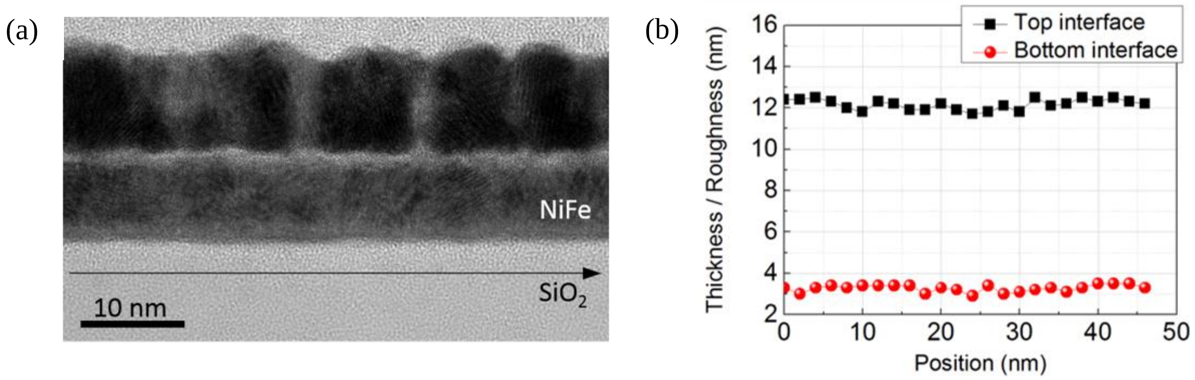

Figure 51 : (a) Transmission electron microscopy image (TEM) for Si/SiO_2//Cu4/NiFe8/Cu3//Al(Ox)2 (nm). (b) Roughness profile of the top and bottom interface. The reference axis for the position of the top and bottom interfaces is represented by the straight line in (a). The TEM measurement was subcontracted to SERMA technologies.

Actual stack	//Roughness-bottom interface (nm)	Roughness-top interface// (nm)
Si/SiO_2/NiFeOx0.3//**NiFe8**//NiFeOx1.6	0.17	0.25
Si/SiO_2/NiFeOx0.3//**NiFe8**/Cu3/IrMn0.6//AlOx2	0.17	0.28
Si/SiO_2//**Cu4/NiFe8**/Cu3//AlOx2	0.22	0.28

Table 2 : Bottom and top interface roughness for various NiFe based samples. The TEM measurement and the corresponding analysis was subcontracted to SERMA technologies.

From Figure 50(c) we also observe that a spectrum asymmetry gradually builds up with increasing the Cu layer thickness. The amplitude of this effect is independent on the position of the Cu layer in the stack (whether we are considering buffer or capping Cu layer) in contrast to the sign of the asymmetry (positive for $Cu^{capping}$ and negative for Cu^{buffer}). Such a behavior highlights the non-negligible impact of eddy currents circulating in the conductive Cu layers, as evoked in Refs. [99,100]. As introduced in section II.1.2.2 and shown in Figure 13, the oscillation of the NiFe magnetization generates an rf magnetic field that creates eddy currents in the surrounding Cu layers. In return, the eddy currents generate a feedback rf magnetic field that contributes to the dephasing of the NiFe magnetization dynamics. This dephasing translates into an asymmetry of the NiFe resonance lineshape. The feedback rf magnetic fields of the top and bottom Cu layers are naturally in antiphase to one another. More investigations are also being carried out to further understand the role of eddy currents in our systems. Note that the incoming microwave is surely partly screened by the Cu layers. Such a screening attenuates the amplitude of the wave reaching the NiFe layer.

Summary

Overall, there is a significant correlation between the experimental findings for NiFe/Cu/IrMn samples (Chapter II.2), NiFe/NiFeOx and NiO/NiFe stacks (Chapter II.4). In all cases the results highlighted the importance of the enhanced spin angular momentum absorption at the antiferromagnetic-to-paramagnetic phase transition, regardless the electrical state of the antiferromagnet under investigation. Another intriguing observation to emerge from the data is that the nature of spin transport, whether it is an electronic or magnonic transport, plays a crucial role in the absorption of the spin current by the antiferromagnetic spin sink. The interfacial exchange bias seems to act as spin current amplifier, revealing its potential to serve as a useful engineering tool for future antiferromagnetic spintronic devices.

III. In search of electrical detection of spin currents in antiferromagnets

In this chapter conversion of spin currents into charge currents by means of inverse spin Hall effect, ISHE, is used to measure electrically spin currents absorbed in antiferromagnets. Like in Chapter II, the spin pumping method is used considering NiFe as the spin injector and antiferromagnetic IrMn acting as spin sink (spin convertor). Given the fact that spin currents travel through interfaces and within antiferromagnets before being converted into charge currents we expect to probe electrically magnetic phase transitions that relate to linear fluctuations, similar to what has been seen thus far in Chapter II. In addition, we also expect to probe and demonstrate non-linear fluctuations in antiferromagnets, in analogous to Ref. [166,167] in ferromagnets. The first section is dedicated to a brief description of the underlying physical principles of (inverse) spin Hall effect, followed by the description of the experimental procedure used throughout. In sections 2 and 3 the main experimental results are discussed. In fact, the data revealed an unexpected behavior mainly related to the NiFe itself that overshadowed the physics associated to the antiferromagnet.

III.1 Introduction to (inverse) spin Hall effect

The spin Hall effect [52,168] refers to the generation of a transverse spin current, I_S, by an electric charge current, I_C, as illustrated in Figure 52(a). The reciprocal effect, where a spin current is converted into a charge current is known as the inverse spin Hall effect, depicted in Figure 52(b). In fact charge and spin are closely related to each other via a quality called the spin-orbit interaction which is responsible for the conversion between the two kinds of current.

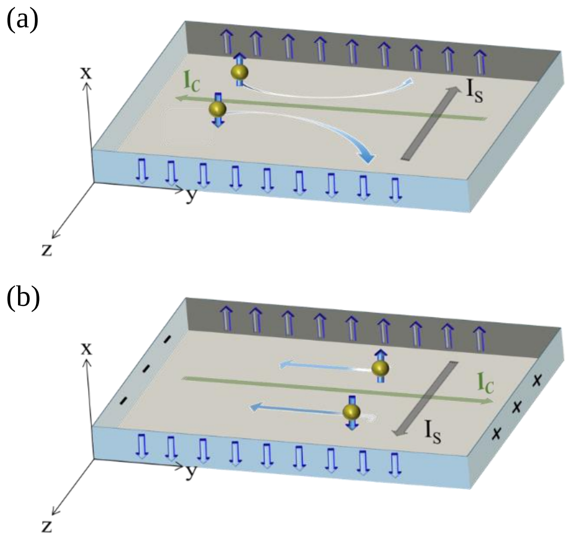

Figure 52 : Schematic diagram of: (a) spin Hall effect (SHE) and (b) Inverse spin Hall effect (ISHE). In our experiments, the sample's thickness, width and length lie along z, x and y axis, respectively.

The spin Hall effect (inverse) efficiency is usually given by the spin Hall angle, θ_{SHE}, that is defined as the ratio between spin (charge) and charge (spin) current density (it is also referred to as the ratio between longitudinal and transverse resistivity times $e/\hbar$).

In the following subsection we will very briefly introduce the possible physical mechanisms underlying the spin Hall effect: the intrinsic contribution related to the band structure of the material and the two extrinsic contributions, namely the side jump and skew scattering originated by impurity scattering.

III.1.1 Spin Hall mechanisms

III.1.1.1 Intrinsic

The origin of the intrinsic spin Hall effect is closely related to the crystal structure of the material and in particular to the intrinsic spin-orbit coupling of the band structure. In the intrinsic spin Hall effect, electrons travelling in the material acquire a transverse spin-dependent velocity leading to spin accumulation at the edges. This mechanism may be driven by the bulk band structure and is expressed in terms of the Berry curvature. Other intrinsic effects producing a transverse voltage may also arise from symmetry breaking at surfaces and interfaces (Figure 53) inducing Rashba split band structure [52,168]. It is noteworthy that the intrinsic spin Hall effect (spin Hall conductivity, resistivity) does not depend on impurities, meaning that the intrinsic contribution to the spin Hall angle increases when the sample resistivity is increased.

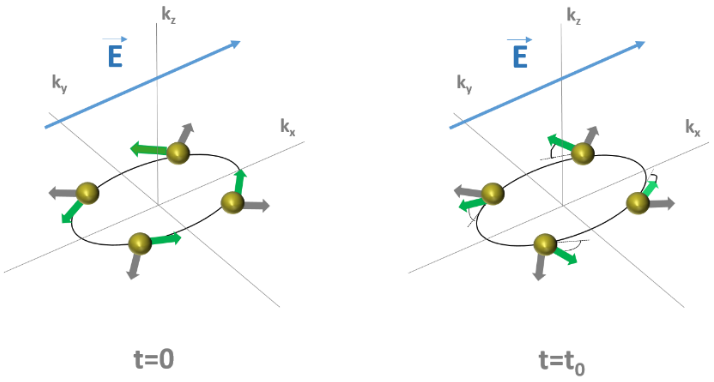

Figure 53 : Schematic illustration of the intrinsic effect in the Rashba-split band structures, as described by Sinova *et al.* [169]. The electric field applied to the system causes the distortion of the Fermi distribution which in turn makes the electrons accelerate. The spins experience a new torque due to Rashba field and precess about it. The precessing spins generate an out-of-plane spin accumulation (in z axis) which causes the spins to tilt in the perpendicular direction.

III.1.1.2 Extrinsic

The two extrinsic contributions to spin Hall effect namely the skew scattering and side jump mechanism occur due to the spin-orbit interaction with impurities, defects and phonons, present in the materials. In the skew scattering mechanism [170,171] the electrons are scattered asymmetrically by the spin-orbit coupling caused by the impurity, whereas in the side jump mechanism [172] the electrons are deflected by the impurity.

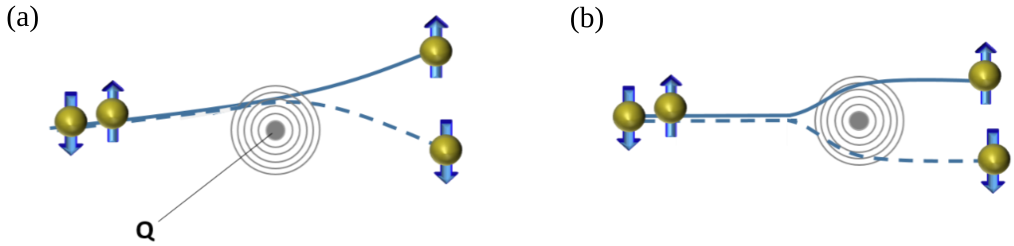

Figure 54 : Scheme of the extrinsic contribution to the spin Hall Effect: (a) skew scattering and (b) side jump mechanism originated by impurity with charge Q.

Figure 54(a) represents the skew scattering mechanism. In the central potential of the impurity with charge Q, the spin-orbit coupling breaks the inversion symmetry. As a result, the scattering cross section depends on the scattering angle but also on the incident wave vector and the spin state. Thus, the trajectories of the incident electrons presenting spin-up will preferably scatter to states of positive angular momentum therefore being scattered to the left. In the opposite case, electrons with spin-down are deviated to the right. Note that [173], the sign of the effect depends on the sign of the electron-impurity interaction; on whether the interaction is repulsive or attractive. The transversal displacement of the trajectories leads to spin accumulation on the sample edges and to spin Hall effect signal. It is noteworthy that the skew scattering mechanism depends on the amount of impurities (i.e. on the resistivity) meaning that the skew scattering contribution to the spin Hall angle is independent on the resistivity.

The second extrinsic contribution to spin Hall effect is the side jump mechanism which was proposed by Berger [172] and is illustrated in Figure 54(b). Berger described the electrons as a wave packet. The collision of the wave packet with the impurity (seen as electrical potential) involves a change in the average momentum of the wave packet, resulting in a lateral spin dependent displacement due to different spin dependent acceleration and deceleration during scattering [52].

III.1.2 Typical experimental procedure

In a typical experiment, the signal generator sends an electromagnetic wave at a frequency of 9.6 GHz to the cavity, see section II.1.3. The pumped spin current is converted into a transverse charge current, generated by the inverse spin Hall effect, resulting into a measurable voltage across two contacts. Note that, the inverse spin Hall voltage can be contaminated by other contributions, due to various mechanisms, as described later in this section. It should be mentioned here that for our experiments we used the setup and the experimental procedure previously developed by NM laboratory [121] (merged with SPINTEC, in 2016). The experimental setup is illustrated in Figure 55(a). A typical measurement consists in recording the evolution of the transverse voltage as a function of a bias magnetic field. Typical data are shown in Figure 55(b) for two directions of the applied field: θ_H=90° and θ_H=-90°. The signals have superimposed symmetric and antisymmetric Lorentzian components and can be described by the following equation [121,174]:

$$V = V_{sym}\frac{\Delta H^2}{\Delta H^2+(H-H_{res})^2} + V_{antisym}\frac{\Delta H(H-H_{res})}{\Delta H^2+(H-H_{res})^2} \qquad \text{(Eq. III.1)},$$

where ΔH is the full width at half maximum and relates to the peak to peak linewidth, $\Delta H=(\sqrt{3/2})\Delta H_{pp}$ [121]. In the most general case, when the bias field is not applied along any specific direction both symmetric, V_{sym}, and antisymmetric contributions, $V_{antisym}$, partly relate to anisotropic magnetoresistance (including planar Hall effect) as well as to anomalous Hall Effect. The physical origin of these contributions are attributed to the time varying change of resistance of the ferromagnet as the magnetization is changing which combines with radio-frequency currents induced by the incident electromagnetic wave giving rise to a dc voltage [54,121]. This is also known as spin rectification effect (V_{SRE}) [174–176]. In addition to the spin rectification effect, V_{sym} also contains a contribution due to the inverse spin Hall effect (V_{ISHE}). The red and blue lines in Figure 55(b) are a fit according to Eq. III.1, from which we extracted V_{sym}, and $V_{antisym}$, for θ_H=90°: 15.83μV and 0.333 μV and for θ_H=-90°: -12.99μV and 1.902 μV, respectively.

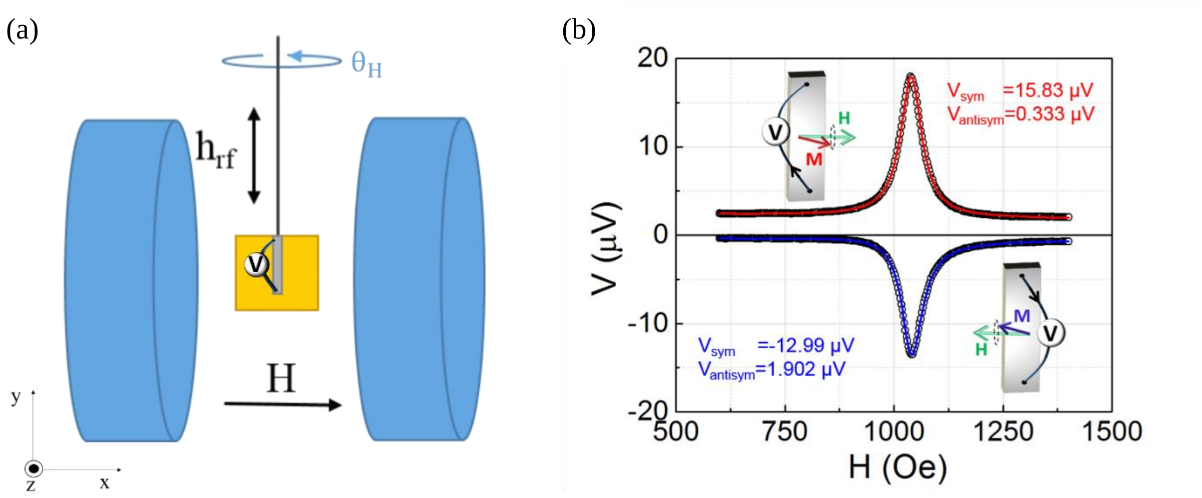

Figure 55 : (a) Schematic overview of the experimental set up. The displayed voltage probes the charge currents generated in the sample. (b) Magnetic field dependence of the generated voltage, for two directions; θ_H=90° and θ_H=-90° (see Figure 20(a) for sample and magnetic field geometry) for a typical spin injector / spin convector bilayer. The open circles present the experimental data and the solid lines indicate the fitting according to the Lorentz function which returns the symmetric and antisymmetric components.

Note that V_{sym} is zero when the field direction is along the film strip, θ_H=0° [174]. On the contrary a finite V_{sym} (=V_{ISHE} + V_{SRE}) is anticipated for θ_H=90°. Given our sample's geometry and wiring convention, a positive V_{sym} for θ_H=90° would correspond to a positive spin Hall angle, provided that the signal mostly relates to the inverse spin Hall effect. Similarly, a negative V_{sym} is expected when the field is reversed to θ_H=-90°. It is noteworthy that the angular dependences of V_{sym} and $V_{antisym}$ can be calculated and used to determine accurately the different contributions and in particular the contributions to V_{ISHE} [121,174]. In our preliminary experiments, we only used two directions for the applied field: θ_H=90° and θ_H=-90°. It should be emphasized here that the strength of the microwave excitation experienced by the sample is not strictly the same for θ_H=90° and θ_H=-90°. Thus to allow for accurate comparison of the dc transverse signals between the two magnetic field directions one must normalize and average the data by h_{rf}^2. Based on the specifications of our resonance cavity; $h_{rf} = 2*\sqrt{(P*Q/500)}$, where the quality factor of the cavity, Q, is measured for every experiment: $Q = f/\Delta f$. P is the power of the electromagnetic wave generator. Our power dependence measurements (V_{sym} vs P) revealed a linear dependence for P= 5 to 60 mW, demonstrating that the heating effect due to the microwave application was negligible. Therefore, we conducted our experiments with an input microwave power of 40 mW.

Figure 56 shows the temperature dependence of V_{sym} for positive (θ_H=90°) and negative bias field (θ_H=-90°), top and bottom panel respectively.

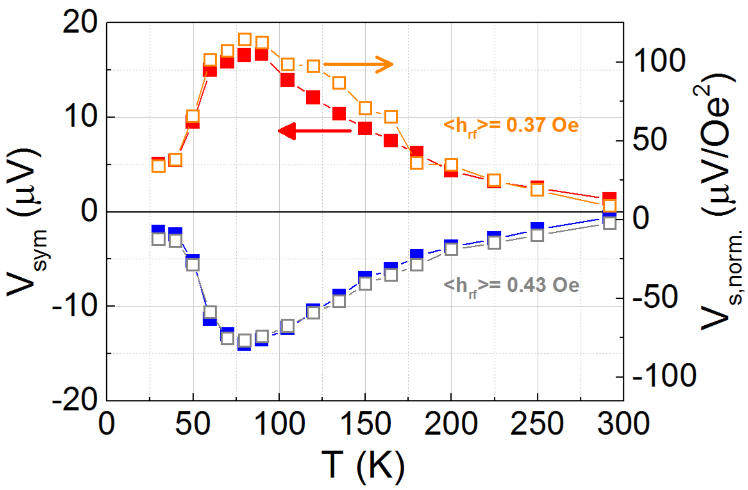

Figure 56 : Temperature dependence of the generated voltage; symmetric Lorentzian component, V_{sym} and normalized voltage, $V_{s,norm.}$ on the right axis. The top panel refers to positive bias field (θ_H=90°) whereas the bottom to negative bias field (θ_H=-90°). The mean value of h_{rf} was found to be 0.37 Oe and 0.43 Oe for positive and negative bias field, with standard deviation of 0.02 Oe and 0.03 Oe, respectively.

The overall normalized transverse dc voltage (induced by spin pumping) is defined as $V_{s,norm.} = \langle V_{sym}/h_{rf}^2 \rangle$, where $\langle V_{sym} \rangle$ stands for the averaged values of V_{sym} for both θ_H=90° and θ_H=-90°, see right axis in Figure 56. The resulting temperature dependence of the overall transverse voltage (left axis) is depicted in Figure 57. A maximum is observed at 80-100K. The reasons for it will be discussed later in section II.3 and II.4. Whenever relevant, the corresponding charge current induced by spin pumping is defined as $I_{C,norm.} = V_{s,norm.}/R$. From spin pumping theory (see Chapter II.1.2.2), the dc-component of the spin current flowing through the stack is given by the following equation:

$$I_s = \frac{\frac{2e}{\hbar}\,\frac{g_{eff}^{\uparrow\downarrow}}{S}\,\gamma^2\,\hbar\,(\,\mu_0 h_{rf}\,)^2}{8\,\pi\,\alpha^2}\;\frac{M\gamma\mu_0+\sqrt{(M\gamma\mu_0)^2+4\,\omega^2}}{(M\gamma\mu_0)^2+4\,\omega^2} \qquad \text{(Eq. III.2),}$$

where M is the effective magnetization, $\frac{g_{eff}^{\uparrow\downarrow}}{S}$ the effective spin mixing conductance, h_{rf} the microwave magnetic field strength and ω the resonant frequency. When the spin current is converted into charge current via inverse spin Hall effect the resulting inverse spin Hall effect (ISHE) contribution is expressed as:

$$V_{ISHE} = RI_C = R\,W\theta_{SHE}\,l_{sf}^N \tanh\frac{t_N}{2\,l_{sf}^N}\;I_S \qquad \text{(Eq. III.3),}$$

where l_{sf}^N corresponds to the spin diffusion length, t_N to the thickness of the spin sink, W to the width of the sample, R to the sample’s resistance and θ_{SHE} to the spin Hall angle.

Replacing now Eq. III.2 to Eq. III.3, V_{ISHE} is given by:

$$V_{ISHE} = R\,W\theta_{SHE}\,l_{sf}^N \tanh\frac{t_N}{2\,l_{sf}^N}\;\frac{\frac{2e}{\hbar}\,\frac{g_{eff}^{\uparrow\downarrow}}{S}\,\gamma^2\,\hbar\,(\,\mu_0 h_{rf}\,)^2}{8\,\pi\,\alpha^2}\;\frac{M\gamma\mu_0+\sqrt{(M\gamma\mu_0)^2+4\,\omega^2}}{(M\gamma\mu_0)^2+4\,\omega^2} \qquad \text{(Eq.III.4).}$$

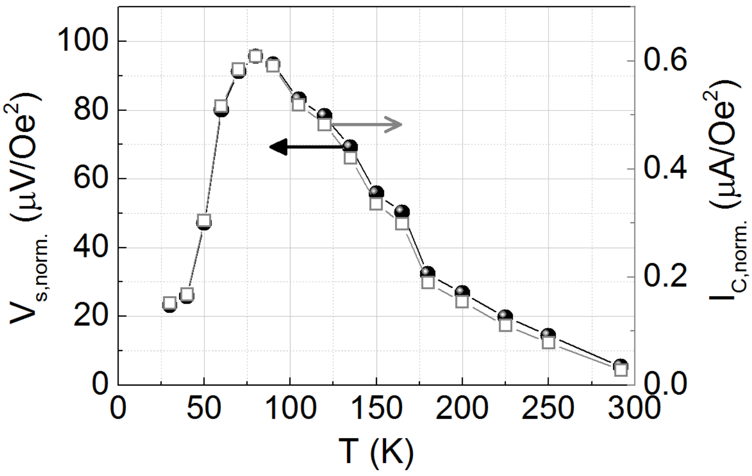

Figure 57 : Typical graph of $V_{s,norm.}$ and $I_{C,norm.}$ versus temperature data. The sample’s resistance is 194 Ohm at room temperature and 153.1 Ohm at 30K.

III.2 State of the art

In retrospect, the observation of inverse spin Hall effect in nonmagnetic materials such as Pt, Ta, Pd [56,177–180] has triggered a considerable attention in the scientific community. Since the origin of intrinsic as well as extrinsic spin Hall effect lies on physical principles, independent of the magnetic order, it is only natural to expect spin Hall phenomena in the case of antiferromagnets. In the following paragraphs, we will briefly address the existing literature and subsequently describe the motivation behind our study.

Preliminary work in this field was focused primarily on the investigation and determination of the spin Hall angle in antiferromagnets. A cumulative list of spin Hall angle for various antiferromagnets is presented in Table 3 [24]. Mendes *et al.* in 2014 [26] were one of the first to study the spin Hall effect in IrMn layers and show a spin Hall angle comparable to the one of platinum. These results triggered a new series of studies in the same context based though on different experimental schemes and different antiferromagnets. Notably, Zhang *et al.* [29] performed a systematic study considering various metallic antiferromagnets where they recorded the transverse voltage as a function of the film thickness and deduced in turn some fundamental parameters specific to antiferromagnets, see Figure 58. In their work, they pointed out the importance of spin-orbit coupling of the heavy metals for the properties of the Mn-based antiferromagnetic alloys, after confirming that *5d*-metal alloys present larger spin Hall angle in compare to their *4d* counterparts.

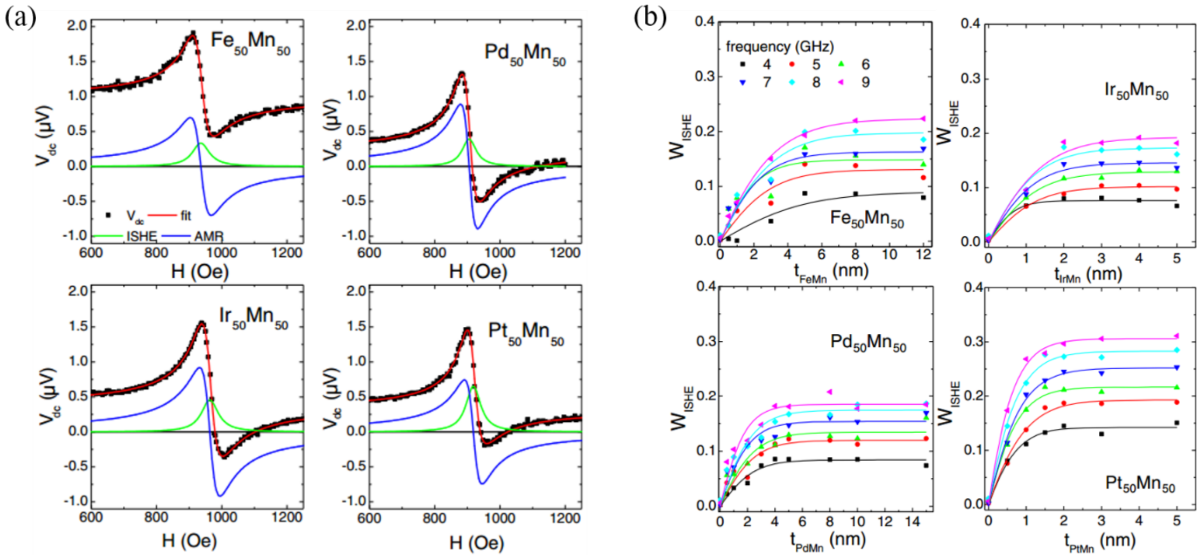

Figure 58 : (a) Magnetic field dependence of the generated dc voltage at 300K for various metallic antiferromagnets: FeMn, IrMn, PdMn and PtMn. (b) Relationship between the weight, W_{ISHE}, of the symmetric Lorentzian component to the thickness of the antiferromagnet, where $W_{ISHE}=1/(1+V_{AMR}/V_{ISHE})$. From Ref. [29].

Further studies [32,140,181] showed the impact of *d*-orbital filling and pointed out the additive nature of effects due to atomic number which seems to apply also in the case of antiferromagnetic alloys, as shown in Figure 59. Since the majority of the corresponding studies refer to room temperature measurements, attention also must be paid to the role of magnetic ordering to the spin Hall effect [24].

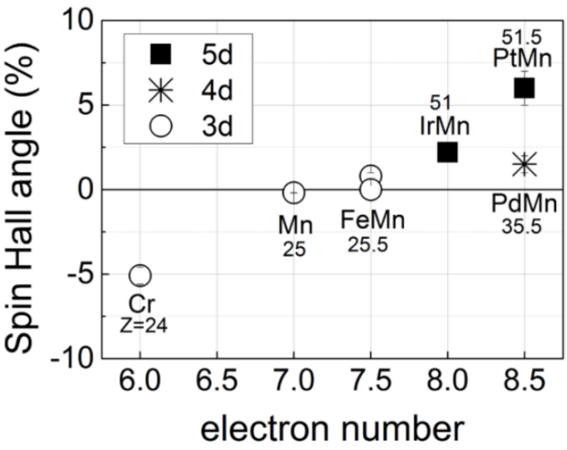

Figure 59 : Spin Hall angle as a function of electron number. From Ref. [24].

Here inspired by our recent experimental findings related to spin pumping and magnetic ordering of antiferromagnets (see Chapter II) we investigated the electrical detection of spin currents by means of the inverse spin Hall effect as a function of temperature and especially near the magnetic phase transition. The main point of interest is to examine the effect of spin fluctuations at the magnetic phase transition on the spin Hall effect [166,167].

AF material	Effective spin Hall angle (%)	Technique	Stack
Pt$_{50}$Mn$_{50}$	6 ± 1	SP	NiFe/Cu/PtMn
Pt$_{50}$Mn$_{50}$	6.4 – 8.1	ST-FMR	NiFe/Cu/PtMn
Pt$_{50}$Mn$_{50}$	8 (DL), 2 (FL)	MOD	NiFe/Cu/PtMn
Pt$_{50}$Mn$_{50}$ (c-axis)	4.8 – 5.2	ST-FMR	NiFe/Cu/PtMn
Pt$_{50}$Mn$_{50}$ (a-axis)	8.6 – 8.9	ST-FMR	NiFe/Cu/PtMn
Pt$_{50}$Mn$_{50}$	10	ST-FMS	[Co/Ni]/PtMn (oop)
Pt$_{50}$Mn$_{50}$	16 – 19 (DL)* 4 – 0 (FL)	ST-FMR (HR)	Co/PtMn and reversed
Pt$_{50}$Mn$_{50}$	9.6 – 17.4 (DL)* 4.3 – 3.6 (FL)	ST-FMR (HR)	FeCoB/PtMn and reversed
Pt$_{50}$Mn$_{50}$	11 (DL)*, 4 (FL)	ST-FMR (HR)	FeCoB/PtMn (oop)
Pt$_{50}$Mn$_{50}$	24 (DL)*	ST-FMR (HR)	FeCoB/Hf/PtMn (oop)
Ir$_{50}$Mn$_{50}$	2.2 ± 0.5	SP	NiFe/Cu/IrMn
Ir$_{50}$Mn$_{50}$	5.3 – 5.7	ST-FMR	NiFe/Cu/PtMn
Ir$_{50}$Mn$_{50}$ (~poly., tentatively a-axis)	2.3	ST-FMR	NiFe/Cu/PtMn
Ir$_{50}$Mn$_{50}$ (c-axis)	5 ± 0.5	ST-FMR	NiFe/Cu/PtMn
γ-Ir$_{20}$Mn$_{80}$	0.8 – 6.4 ; 0.8 x Pt**	SP and SSE	YIG/IrMn
Ir$_{20}$Mn$_{80}$	2.9 ± 1.5 (DL)	ST-FMR (HR)	CoFeB/IrMn
Ir$_{20}$Mn$_{80}$	4.3 ± 0.1 (DL)	MOD	NiFe/Cu/IrMn
Ir$_{20}$Mn$_{80}$	5.6 ± 0.9	ST-FMR	NiFe/Cu/IrMn
Ir$_{22}$Mn$_{78}$	5.7 ± 0.2 (DL)	ST-FMR (HR)	CoFeB/IrMn
Ir$_{20}$Mn$_{80}$	> 10.9***	ST-FMR	NiFe/IrMn
Ir$_{20}$Mn$_{80}$	13.5 (DL)	MOD	NiFe/IrMn
Ir$_{25}$Mn$_{75}$	2	ST-FMR	NiFe/IrMn
Ir$_{25}$Mn$_{75}$	~9	ST-FMR	NiFe/IrMn
Ir$_{25}$Mn$_{75}$ (111)	~11	ST-FMR	NiFe/IrMn
Ir$_{25}$Mn$_{75}$ (100)	~20	ST-FMR	NiFe/IrMn
Pd$_{50}$Mn$_{50}$	1.5 ± 0.5	SP	NiFe/Cu/PdMn
Pd$_{50}$Mn$_{50}$	2.8 – 4.9	ST-FMR	NiFe/Cu/PtMn
Pd$_{50}$Mn$_{50}$ (c-axis)	3.2 ± 0.6	ST-FMR	NiFe/Cu/PtMn
Pd$_{50}$Mn$_{50}$ (a-axis)	3.9 ± 0.5	ST-FMR	NiFe/Cu/PtMn
Cr	-5.1 ± 0.5	SP	YIG/Cr
Cr (30 - 345K)	-9 (-1.38 x 20 x Cu)	SSE	YIG/Cr
Mn	-0.19 ± 0.01	SP	YIG/Mn
Fe$_{50}$Mn$_{50}$	0.8 ± 0.2	SP	NiFe/Cu/FeMn
Fe$_{50}$Mn$_{50}$	2.2 – 2.8	ST-FMR	NiFe/Cu/FeMn
γ-Fe$_{50}$Mn$_{50}$	-(7.4 ± 0.8) x 10^{-3}	SP	YIG/FeMn

Table 3 : Spin Hall angles determined for various antiferromagnets. When not specified, the investigation temperature was 300 K, and the layers were polycrystalline. SP and SP (ΔH) = ferromagnetic resonance spin pumping excitation – detected based on the inverse spin Hall effect, or ferromagnetic resonance linewidth (when (ΔH) is specified), ST-FMR and ST-FMR (HR) = spin torque ferromagnetic resonance excitation induced by spin Hall effect subsequent to an ac current flow – detected based on anisotropic magnetoresistance, or 2nd harmonic response detection of the anomalous Hall effect and/or anisotropic magnetoresistance (when (HR) is specified), MOD = spin Hall effect excitations induced by a dc current flow - detection of the modulation of the ferromagnetic resonance damping, ST-FMS = spin torque ferromagnetic switching induced by spin Hall effect subsequent to a dc current flow – anomalous Hall effect detection, SSE = longitudinal spin Seebeck excitation induced by a thermal gradient – inverse spin Hall effect detection, and oop = out-of-plane magnetization. DL and FL refer to damping-like and field-like torque components, respectively. *Values of the spin torque efficiency [effective interface transparency (<1) x spin Hall angle]. **The values of the effective spin Hall angle for Pt were taken from [182] and typically range between values close to 1% and 10%. ***Linear increase with the IrMn thickness. Table and caption from Ref. [24], see also Refs. therein.

III.3 Influence of spin fluctuations on the spin Hall effect

Temperature dependence inverse spin Hall effect experiments are expected to confirm the results illustrated in Chapter II (see Figure 26), where a more prevalent spin transport at $T \sim T_{crit}$ was demonstrated. In other words we expect to see a peak in the temperature dependence of the spin Hall voltage at the magnetic phase transition of the antiferromagnet, where maximum spin fluctuations occur. In addition, we expect to probe asymmetric signals that relate to non-linear fluctuations, as presented in Ref. [166,167]. To this end, we conducted electrical experiments considering the same IrMn based stacks, as in section II.2.1: $Si/SiO_2/NiFe8/Cu3/IrMn(t_{IrMn})/Al2$ (nm). The results are depicted in Figure 60(a). A maximum of transverse dc voltage is observed for all IrMn thicknesses. Nonetheless, this maximum is also observed in the case of our reference sample ($t_{IrMn} = 0$), which allows us to conclude that it is unrelated to the presence of the antiferromagnetic layer. Moreover the position of the maximum transverse dc voltage is independent of the IrMn thickness contrary to what is expected considering our previous experimental observations (see Figure 60(b)), where the spin pumping peak relates to the IrMn magnetic phase transition, T_{crit}^{IrMn}. This points to the potential influence of the Cu/AlOx interface (we recall that Al becomes AlOx when exposed to air). However, results obtained considering different interfaces, e.g. $Si/SiO_2/NiFe8/Cu3/PtMn1/MgO3$ (nm) produced a similar maximum amplitude. Interestingly, the amplitude of the maximum transverse dc voltage at 80K is larger for the $Si/SiO_2/NiFe8/Cu3/Al2$ (nm) sample ($t_{IrMn} = 0$) compared to the IrMn samples. In fact the maximum transverse dc voltage shows to decrease with the thickness of the IrMn layer. This is specific to the spin Hall effect in the IrMn layer.

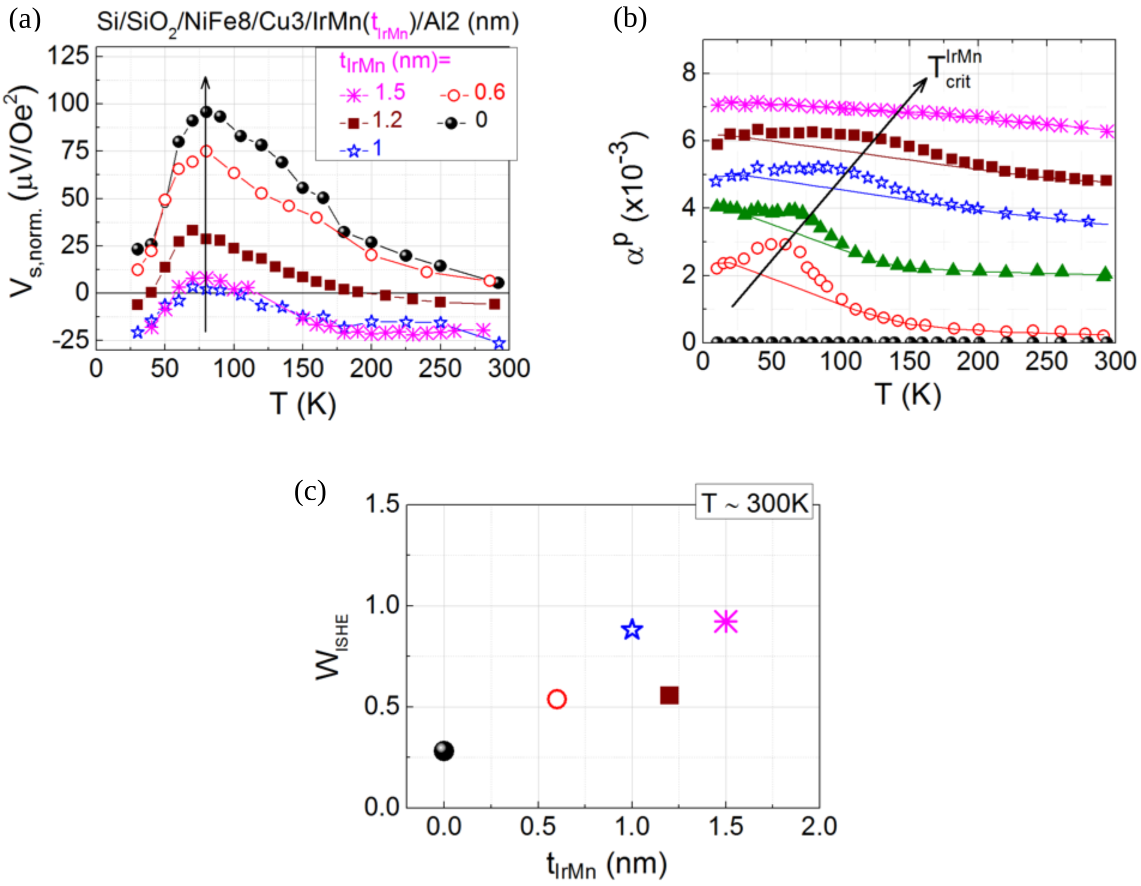

Figure 60 : (a) Temperature dependence of $V_{s,norm.}$ for $Si/SiO_2/NiFe8/Cu3/IrMn(t_{IrMn})/Al2$ (nm) stacks, where t_{IrMn} corresponds to thickness of the IrMn layer. (b) α^p vs. temperature for the same samples. To facilitate reading, the data were shifted vertically. The baselines are used as guides to the eye. (c) Thickness dependence of W_{ISHE} at 300K deduced from Figure 60(a).

As in Ref. [29] (see also Figure 58) we use here the parameter W_{ISHE} to account for the inverse spin Hall effect in the IrMn layers at room temperature. W_{ISHE} refers to the weight of the symmetric Lorentzian component and is defined as $W_{ISHE} = 1/(1+V_{antis.norm.}/V_{s,norm.})$. Figure 60(c) shows the thickness dependence of W_{ISHE} (as deduced from Figure 60(a)) exhibiting a linear dependence that is expected to saturate above t_{IrMn}=2nm. The results are found to be in qualitative accordance to what has been reported before in the literature [29,31] for IrMn layers (see Figure 58(b) and Figure 23). In particular, W_{ISHE} is found to be about an order of magnitude larger than that given in Ref. [29] (Figure 58). This disparity is likely related to the difference in sample size used in the studies. The value of W_{ISHE} for $Si/SiO_2/NiFe8/Cu3/Al2$ (nm) sample ($t_{IrMn} = 0$) suggests a likely contribution of spin rectification effect to the dc generated voltage. As a matter of fact, we recall that the transverse dc voltage induced by spin pumping contains a contribution related to spin rectification effects and more specifically to the planar Hall effect (proportional to $R_{//} - R_{\perp}$). It is known that magnetoresistance effects are non-negligible in the case of NiFe, as highlighted in Ref. [183]. Here, we measured a value of 0.8% at room temperature, as depicted in Figure 61, where we plotted the temperature dependence of the anisotropic magnetoresistance for $Si/SiO_2/NiFe8/Cu3/Al2$ (nm) sample. The resistance showed a few percent change when a magnetic field of 10000 Oe was applied along or across the current. To allow adequate evaluation of the AMR signal we interpolated the resistance curves, $R_{//}$ and $R_{\perp}$, before calculating AMR, see inset Figure 61. The results show that the magnitude of the effect is of the order of 1.25 % at 20K which further decreases monotonously as thermal activation increases, representative for NiFe thin films. In that regard, Figure 61 demonstrates that the non-monotonous behavior of the transverse voltage observed in Figure 60 does not arise from spin rectification effects.

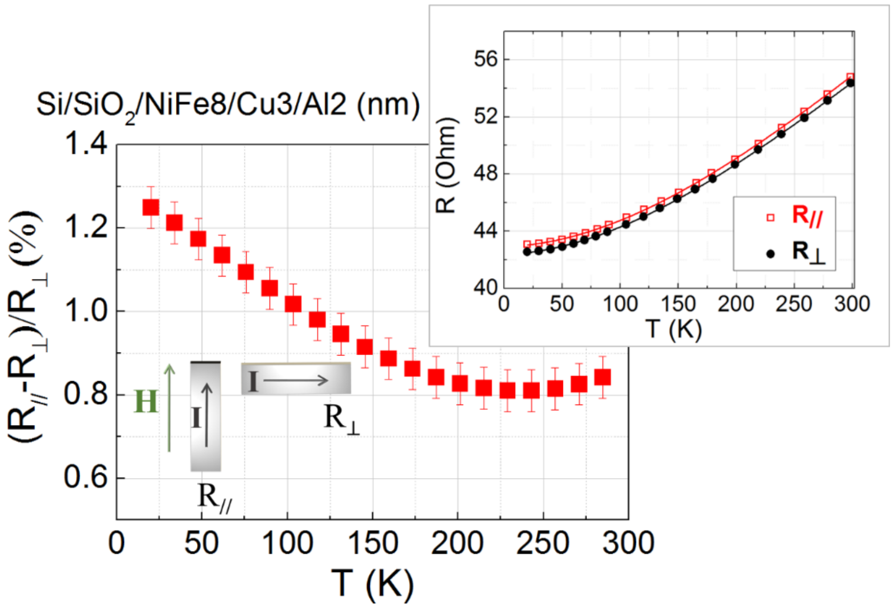

Figure 61 : Temperature dependence of the anisotropic magnetoresistance (AMR) for $Si/SiO_2/NiFe8/Cu3/Al2$ (nm) sample. R⊥ and R// denotes the resistance when the magnetic field of 10000 Oe is applied perpendicular or parallel to the sample plane, respectively, see sketch. Inset: Temperature dependence of the resistance for $R_{\perp}$ and $R_{//}$.

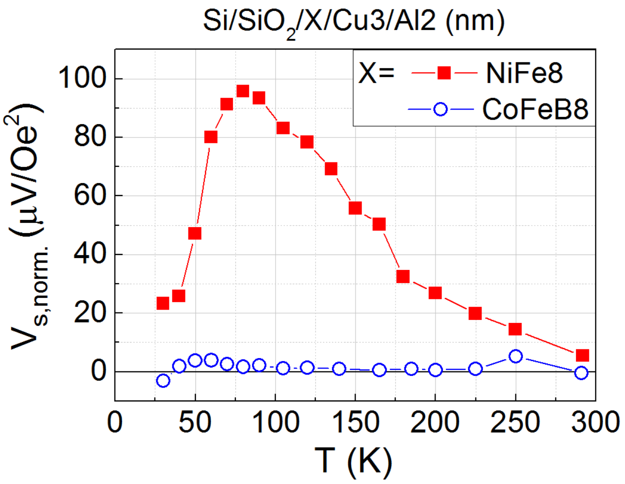

Figure 62 : $V_{s,norm.}$ versus temperature for $Si/SiO_2/NiFe8/Cu3/Al2$ and $Si/SiO_2/CoFeB8/Cu3/Al2$ (nm). The samples resistance is 194 Ohm for NiFe and 365 Ohm for CoFeB, at room temperature.

To shed light on the nature of the maximum transverse dc voltage observed here and to demonstrate whether this is specific to NiFe we tested also a CoFeB based sample, see Figure 62. The results revealed that the maximum observed at 80K should be specific to the intrinsic properties of NiFe itself.

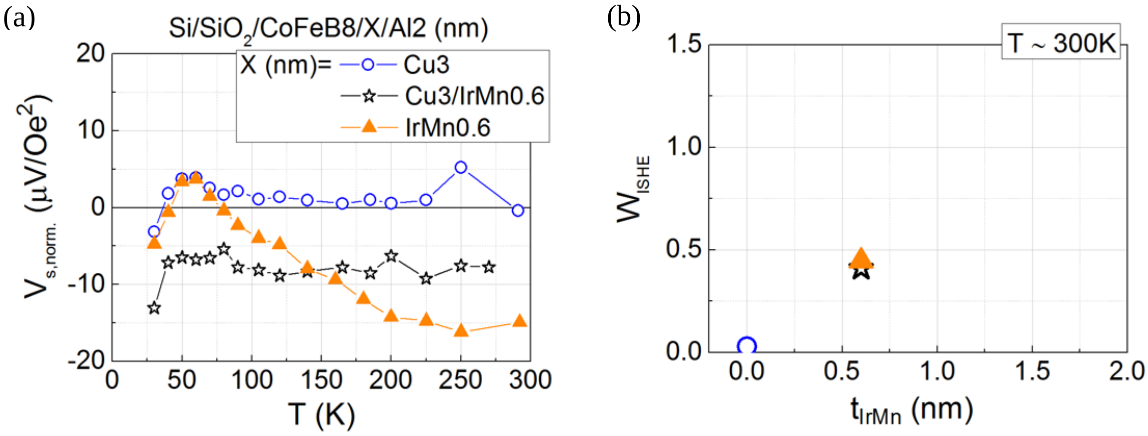

Figure 63 : (a) $V_{s,norm.}$ versus temperature for CoFeB based samples; $Si/SiO_2/CoFeB8/X/Al2$ nm, where X= Cu3, Cu3/IrMn0.6 and IrMn0.6. (b) Thickness dependence of W_{ISHE} at 300K deduced from Figure 63(a).

Given the fact that the bare CoFeB sample is free of any ‘intrinsic’ non monotonous temperature dependence of transverse dc voltage, we believe that it could act as an ideal spin injector that allows to probe spin fluctuations in IrMn layers at the magnetic phase transition, through electrical measurements. Note that the overall transverse dc voltage in CoFeB is zero (see Figure 62) justified by the relatively small AMR value of about 0.026% [184], compared to that typically found in NiFe (see Figure 61). Figure 63(a) shows the temperature dependence of $V_{s,norm.}$ for $Si/SiO_2/CoFeB8/X/Al2$ nm stacks, where X corresponds to Cu3, Cu3/IrMn0.6 and IrMn0.6. A maximum transverse dc voltage is anticipated at the magnetic phase transition, which for IrMn0.6 nm is found to be at 65K, as illustrated in Chapter II.2.2, Figure 26. Indeed, a small enhancement is observed in the case of CoFeB/IrMn0.6 nm sample located at 65K, see Figure 63(a). This maximum is hardly observed in the case of CoFeB/Cu/IrMn0.6 nm sample, consistent with our previous results (see Chapter II.3) that showed more efficient spin injection when the antiferromagnet is fed by spin waves through direct coupling with the ferromagnet.

Figure 63(b) shows W_{ISHE} as function of IrMn. For the $Si/SiO_2/CoFeB8/Cu3/Al2$ sample no W_{ISHE} contribution is observed, consistent with prior literature [185]. The value of W_{ISHE} corresponding to IrMn0.6 nm is in good accordance with the experimental values of W_{ISHE} for NiFe/Cu/IrMn (t_{IrMn}) samples, see Figure 60(c). Note that in the latter case the value of W_{ISHE} is slightly larger for IrMn0.6 nm as it is contaminated by the NiFe AMR contribution which is rather important, compared to the negligible AMR for CoFeB. Moreover, different IrMn growth is probably expected when IrMn and Cu/IrMn grow on top of the amorphous CoFeB compared to the polycrystalline NiFe. Undoubtedly, more systematic experiments are needed to draw conclusions on the effects of linear and nonlinear antiferromagnetic fluctuations on the inverse spin Hall effect. At the moment, further investigations are being carried out in the framework of the Post-doctoral project of Olga Gladii.

III.4 Anomalous spin Hall enhancement in bare NiFe ferromagnetic films

In an effort to understand the origin of the anomalous temperature dependence of transverse dc voltage observed for bare NiFe thin films, we investigated various thicknesses of NiFe in Si/SiO_2/Cu14/NiFe(t_{IrMn})/Cu3/Al2 (nm) stacks. The use of Cu buffer layer of 14 nm eliminates any potential contribution related to the SiO_2/NiFe interface. In fact, it has been suggested that NiFe when in contact with SiO_2 or yttrium iron garnet, YIG substrates acts as a pure spin current detector generating a transverse dc voltage in the NiFe itself [186–189]. In the corresponding literature, the experimental observations are interpreted in terms of strong spin-orbit interaction in NiFe and extrinsic structural symmetry breaking perpendicular to NiFe plane, which coupled to spin current gives rise to transverse dc voltage signals. Figure 64(a) and (b) shows the temperature dependence of $V_{s,norm.}$ and $I_{C,norm.}$ (see section III.1) for different NiFe thickness. It is important to plot also $I_{C,norm.}$ as a function temperature as the value of resistance slightly varies when considering different NiFe thickness. In general, plotting $V_{s,norm.}$ or $I_{C,norm.}$ all depends on the mechanism at the origin of the phenomenon.

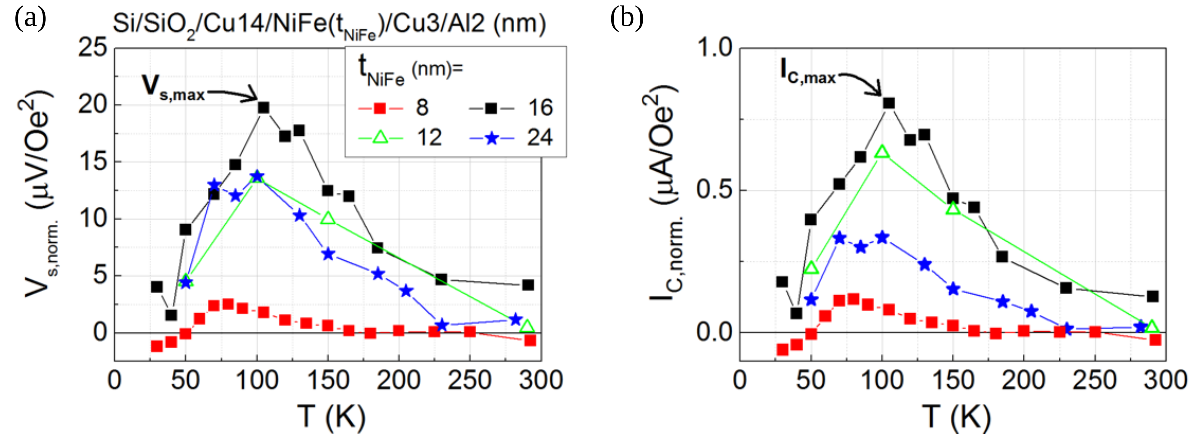

Figure 64 : Temperature dependence of (a) $V_{s,norm.}$ and (b) $I_{C,norm.}$ considering different NiFe thicknesses: 8 to 24 nm. The arrow indicates the maximum values of $V_{s,norm.}$ and $I_{C,norm.}$.

A maximum transverse dc voltage is observed regardless the thickness of the NiFe layer, located at approximately 100K. An arrow is added in Figure 64 to indicate the maximum value. While an enhanced transverse dc voltage is observed for all the sample, its amplitude varies significantly with the NiFe thickness. For the sake of comparison we have plotted the maximum values of $V_{s,norm.}$ and $I_{C,norm.}$ as a function of the NiFe thickness, as well as the thickness dependence of $V_{s,norm.}$ and $I_{C,norm.}$ at 300K, see Figure 65(a) and (b) respectively. The results show that the maximum transverse dc voltage enhancement is more pronounced for NiFe layer with 16 nm thickness. In fact the results at room temperature are similar to those previously observed by Azevedo *et al* [190]. In the corresponding study the authors attributed the generated transverse dc voltage in Si/SiO$_2$/NiFe(t_{NiFe}) stacks to the magnonic charge pumping, MCP. Magnonic charge pumping converts magnetization dynamics into charge current via spin-orbit coupling in ferromagnetic materials with broken spatial inversion symmetry, as explained also in Ref. [191].

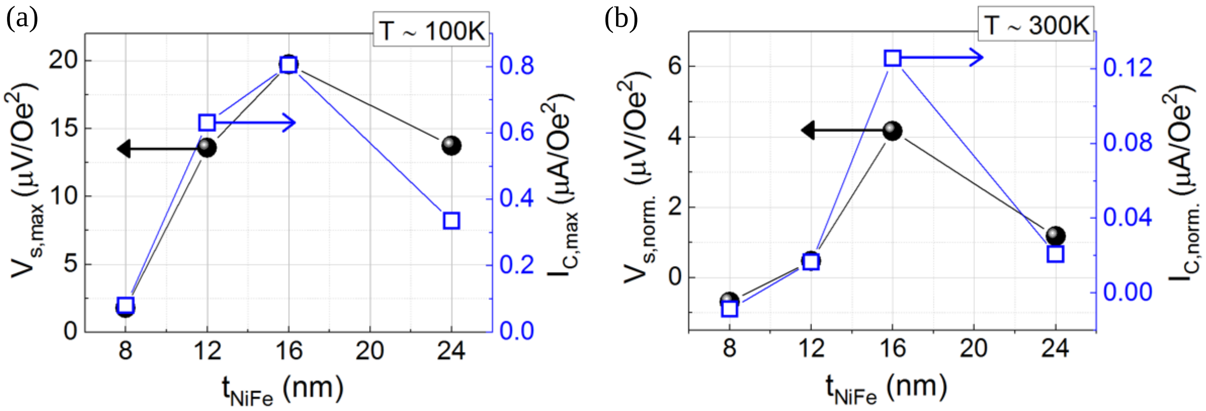

Figure 65 : Thickness dependence of (a) maximum $V_{s,max.}$ and $I_{C,max.}$ and (b) $V_{s,norm.}$ and $I_{C,norm.}$ measured at 300K.

Figure 66 shows the thickness dependence of magnonic charge pumping voltage, V_{MCP} for Si/SiO$_2$/NiFe(t_{NiFe}) (nm) stacks, as observed by Azevedo *et al.* [190]. The origin of the magnonic charge pumping is attributed to an extrinsic structural symmetry breaking perpendicular to the NiFe plane associated to the oxide layer forming on top of the NiFe surface. It was concluded that the forming NiFeOx is responsible for the charge density gradient which in turn gives rise to Rashba spin-orbit coupling, which manifests itself in the surface magnetic anisotropy. The peak at 20 nm of NiFe, observed in Figure 66, is the threshold after which the perpendicular anisotropy field is not important anymore.

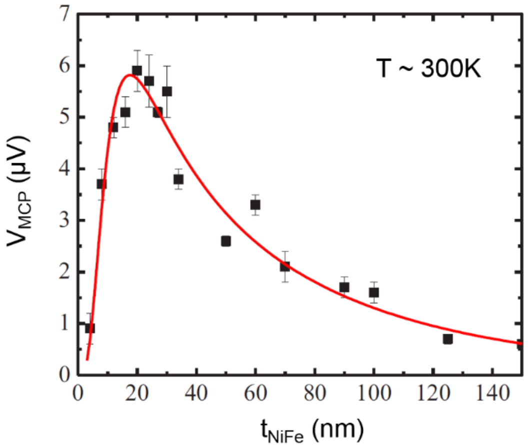

Figure 66 : Thickness dependence of magnonic charge pumping voltage, V_{MCP} for Si/SiO$_2$/NiFe(t_{NiFe}) (nm) stacks, at room temperature. The solid line is the result of theoretical model. From Ref. [190].

While the abovementioned study provides some insight into the transverse dc voltage generated in NiFe thin films at room temperature (although in our case it would probably imply oxidation of the NiFe through the Cu/Al cap), it cannot be invoked to explain the anomalous transverse dc voltage enhancement observed at 100K, thus remaining an open question. Further experiments are currently being pursued in the framework of the Post-doctoral project of Olga Gladii.

Summary

We performed temperature dependence dc voltage measurements in an attempt to probe electrically linear as well as non-linear fluctuations at the magnetic phase transition of IrMn antiferromagnetic films, in NiFe/Cu/IrMn stacks. We demonstrated a non-monotonous temperature dependence of transverse dc voltage mostly related to bare NiFe itself, which overshadowed the effects associated to antiferromagnet. Altering the thickness of NiFe resulted in significant modulation of the amplitude of the generated dc voltage. These findings provide more insight into a growing body of literature on spin current absorption, highlighting the need for further investigations and theoretical understanding. We also showed encouraging preliminary data considering CoFeB as spin injector. Future works using CoFeB as spin injector may allow for electrical detection of spin currents and spin fluctuations in antiferromagnets.

IV. Tuning bulk and interface magnetic properties of antiferromagnets

This chapter complements chapters II and III and is more focused on the magnetic properties of antiferromagnets. In particular, the main goal of this chapter is to tune the properties of antiferromagnets so that they can be used as functional materials in antiferromagnetic spintronics. Via exchange bias, antiferromagnets are usually used to manipulate and study ferromagnets through magnetization pinning, see Chapter I.1. In a reciprocal manner the antiferromagnetic order can be manipulated and studied via exchange bias. Throughout this chapter, we will use exchange bias to characterize the antiferromagnets. Section IV.1 intends to quickly introduce the reader to the exchange bias phenomenology as well as to some theoretical models and to the methodology used in our studies. Sections IV.2-IV.4 are devoted to the experimental results. More specifically, in section IV.2 we will discuss about the influence of spatial dispersion of antiferromagnetic properties in spintronic devices. Next in section IV.3 we will explain how to reduce such dispersions and improve simultaneously the thermal stability of the antiferromagnet. Finally, in Chapter IV.4 we will discuss about what extent is possible to dope an antiferromagnet with a heavy element in order to boost its spin-orbit coupling.

IV.1 Introduction to bulk vs. interface properties probed by exchange bias

IV.1.1 Brief views about exchange bias

IV.1.1.1 Exchange anisotropy

A new type of anisotropy was demonstrated in 1956 by Meiklejohn and Bean [192], which is known as exchange anisotropy but it is more often referred to as exchange bias. The exchange bias effect is a result of the coupling between the ferromagnetic, F, and antiferromagnetic, AF, spins at the interface. Experimentally, exchange bias manifests itself as a shift in the ferromagnet hysteresis loop along the magnetic field axis, see Figure 67(a). In practice, the exchange bias sets a reference direction to ferromagnet, which means that when the coercive field is larger than the hysteresis loop shift, the ferromagnet cannot be demagnetized by any magnetic field as its magnetization will return to the original direction after the field is removed. Exchange bias has found important technological applications such as in magnetoresistive read heads for hard disk drives and in magnetic random access memories, for more details about that please refer to Chapter I.1.

It should be emphasized here that the exchange bias phenomenon is highly temperature dependent. It ceases to exist when approaching the Néel temperature, T_N. In fact, the displacement of the hysteresis loop vanishes at a temperature usually referred to as blocking temperature, T_B. For thick monocrystalline antiferromagnets it has been proved experimentally that $T_N \approx T_B$, whereas for thin films $T_B < T_N$ [15,192–194]. Contrary to T_N, the blocking temperature is not intrinsic to the antiferromagnet but linked to F/AF interactions. It thus depends on interfacial exchange stiffness as well as on the antiferromagnetic grain core properties, such as the antiferromagnetic grain anisotropy energy: KV, where K and V are the antiferromagnetic anisotropy and volume, respectively. Size effects via volume contributions play a crucial role, often resulting in T_B distributions in the case of polycrystalline films due to grains sizes dispersions. T_B distributions will be used systematically in our studies to get information on grains size contribution as well as on the interfacial disordered spins, which role will be described later in this chapter.

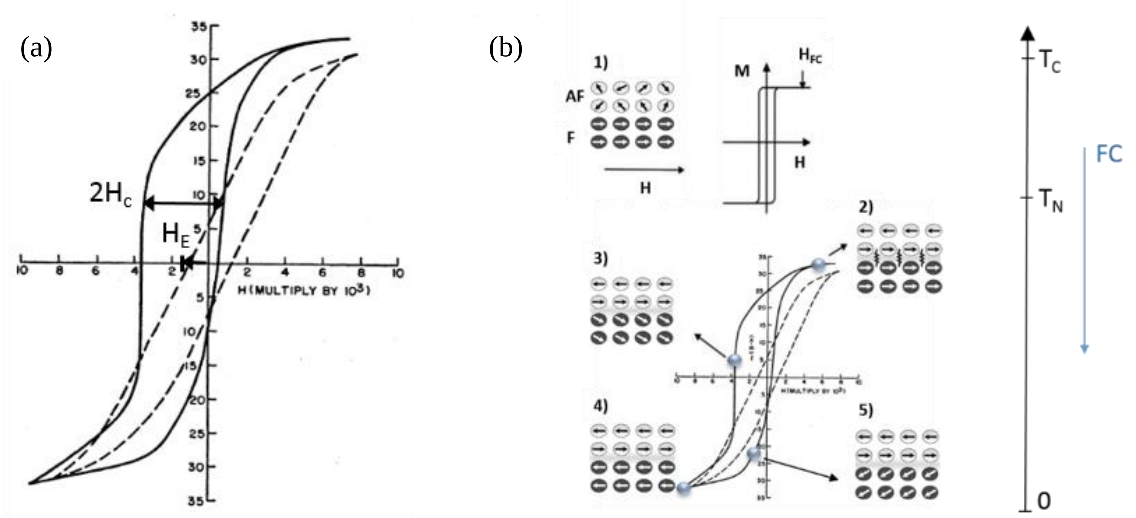

Figure 67 : (a) Hysteresis loops of Co-CoO at 77 K. Solid line: after field cooling the system in a 10000 Oe field. Dashed line: when the F/AF is cooled in zero field (b) schematic diagram describing the shift of hysteresis loop for a F/ AF bilayer system at different stages: 1) above T_B and 2-5 below T_B during the hysteresis loop. Adapted from [192,194].

IV.1.1.2 Setting exchange bias

In order to set exchange bias in a bilayer F/AF system, a specific procedure [15,192,194,195] is employed which is explained in Figure 67(b). The bilayer is heated above T_B, in the presence of a static magnetic field: at this point, all the ferromagnetic spins align along the direction of the applied field, while the antiferromagnetic spins remain randomly oriented, see Figure 67(b)-1. Since the ferromagnet is not pinned yet to the antiferromagnet, the hysteresis loop of the ferromagnet is symmetric about zero. The next step involves cooling the system below T_B all the while applying a static magnetic field. This procedure is also known as the field cooling process, FC. After the FC, the antiferromagnetic spins at the interface with the ferromagnet align ferromagnetically to the ferromagnetic spins. The adjacent antiferromagnetic spin plane aligns antiparallel to the previous one and so forth, resulting in a zero net magnetization. Now, when the applied field is reversed, the ferromagnetic spins start to rotate in-plane to the opposite direction whereas the antiferromagnetic spins remain fixed due to the large antiferromagnetic anisotropy. Due to the interfacial interaction, the ferromagnetic spins are coupled to the antiferromagnetic spins and thus the reversal of the magnetization direction is more difficult. The antiferromagnetic spins exert a microscopic torque to the ferromagnetic spins and thus a stronger external field is required to overcome this pinning and to rotate the ferromagnetic spins, see Figure 67(b)-4. When the external field is switched back to its original direction, the ferromagnetic spins require smaller energy in order to rotate and align ferromagnetically with the antiferromagnetic spins. The interfacial interaction favors now the switching since the torque exerted by the antiferromagnetic spins to the ferromagnet is in the same direction as the external field applied, see Figure 67(b)-5. The system feels an extra biasing field and as a result the ferromagnet hysteresis loop is shifted along the magnetic field axis. The displacement of the ferromagnet hysteresis loop is known as the exchange bias field, H_E.

IV.1.1.3 Theoretical models

The phenomenological description [192,193] used to explain the onset of exchange bias contains some of the relevant ingredients. However, this intuitive picture failed to predict accurately the value of exchange anisotropy giving values several orders of magnitude larger than the ones found experimentally. To address this discrepancy many theoretical models have been proposed in the literature. In the following section, we shall discuss briefly some of them, which will be particularly useful for further understanding of today's macroscopic view that is used in our studies.

Meiklejohn and Bean [192,193] developed a theory considering the energetic terms involved in an exchange bias system. They managed to predict well the sign of the exchange bias field as well as the dependence on the ferromagnet thickness. However, due to the strong assumptions made (e.g. a fixed antiferromagnetic configuration due to infinite anisotropy), the calculated exchange bias field could not compare to the experimental values. To account for this discrepancy, Meiklejohn improved the model by considering a finite antiferromagnetic anisotropy to explain the rotational hysteresis observed [195]. He showed that the antiferromagnet can be uniformly dragged by the ferromagnetic reversal provided that the relative strength of the inner antiferromagnetic energy is high enough. Even though it does not reduce the theoretical value of exchange bias, this model shows the importance of interface magnetization and more specifically on the antiferromagnetic side. Néel [196] and Mauri [197] further complemented Meiklejohn's approach by introducing the concept of a planar domain wall in the antiferromagnet, which develops during the magnetization reversal. The ferromagnet coupled to a weakly anisotropic antiferromagnet gives rise to the formation of an antiferromagnetic wall parallel to the interface. The latter results in a reduced value of exchange bias, but still higher than the experimental values as this model cannot account for the size of the domains. Even though Néel and Mauri's models are found to be in better agreement with the experimental results compared to the previous theoretical models, they fail to provide clues to understand how thinner antiferromagnetic layers can exhibit exchange bias or how compensated antiferromagnetic surfaces can lead to hysteresis loop shift.

These theoretical models considered only the antiferromagnetic reconfiguration due to the ferromagnetic magnetization reversal, disregarding system specific parameters such as magnetic and structural roughness, ferromagnetic and antiferromagnetic anisotropies, film thickness, to name just a few. Over the past years, a big number of theoretical models have been developed to evidence new microscopic fundamentals behind the exchange bias effect. In particular, some models, notably the ones proposed by Malozemoff and Takano, highlighted the role of magnetic frustrations. Malozemoff's model [198] suggested the presence of an interfacial random-field effect to account for the exchange anisotropy in bilayer F/AF systems. He pointed out that the surface roughness or the alloying at the interface, present in any realistic system, may generate a random-field acting from single-domain state ferromagnetic layer onto the antiferromagnetic layer. Based on Imry's ideas [199], he assumed that the antiferromagnetic layer breaks up into domains to minimize the interfacial random-field energy. The resulting exchange bias field shall increase with decreasing the antiferromagnetic domain size. His approach constitutes a good example of the influence of disordered magnetic phases on exchange bias and is in accordance with the model proposed by Takano and Berkowitz [15,200]. In the corresponding model, the F/AF system consisted of a single domain state ferromagnet as well as an antiferromagnet, composed of uncoupled grains with atomic spins and interfacial roughness. According to this model, the origin of unidirectional anisotropy is the uncompensated interfacial antiferromagnetic spins, originating from interfacial frustrations that create disordered magnetic phases. This model is in agreement with the experimental values but only when antiferromagnetic material with high magnetocrystalline anisotropy is considered.

The complexity of the various F/AF interfaces is a key problem with much of the theoretical models proposed thus far. Inevitably, they always reach a point at which critical assumptions are made. Nonetheless, these models have made the first step towards probing microscopic mechanisms which underlie macroscopic events.

IV.1.1.4 Today's macroscopic picture

Today's macroscopic picture [128,201] describes the exchange bias effect on the basis of a granular model coupled to interfacial disordered magnetic phases, inspired by Takano and Berkowitz's theoretical model. The experimental results obtained and presented in this chapter will be explained using this macroscopic picture.

At the risk of oversimplifying a complex physical process, we will describe the macroscopic picture as follows. We consider a polycrystalline F/AF bilayer system, as the one depicted in Figure 68, where the antiferromagnetic layer is represented as a group of uncoupled grains. Each grain is characterized by the antiferromagnetic anisotropy energy, K and the antiferromagnetic grain volume, V and is exchange coupled to the ferromagnetic layer by an interfacial exchange interaction per unit area $J_{F/AF}$. The stability of each antiferromagnetic grain is governed by the competition between the pinning energy KV and the thermal activation energy $\mathrm{Log}(\tau/\tau_0)k_BT$. Therefore, it is fair to conclude that the characteristic blocking temperature is defined by: $(K - J_{F/AF}/t_{AF})V \propto \mathrm{Log}(\tau/\tau_0)k_BT_B$.

The exchange bias field for a polycrystalline system is expressed by the following relation:

$$M_S H_E t_F = \int_{stable\ and\ coupled\ grains} J_{F/AF}\,\frac{V}{t_{AF}}\,P(V)\,dV \qquad \text{(Eq. IV.1).}$$

Since here we are primarily interested in thermally activated process, considerable attention must be paid when describing the exchange bias effect, as both the antiferromagnetic anisotropy and interfacial coupling are temperature dependent. In particular, interfacial disordered spins can act like disordered magnetic phases below the freezing temperature, giving rise to temperature variation of the interfacial exchange interaction $J_{F/AF}$ and consequently to a distribution of interfacial coupling, $D(J_{F/AF})$. The latter is implemented in Eq. IV.1, likewise:

$$M_s H_E t_F = \int \int_{stable\ and\ coupled\ grains} J_{F/AF} D\left(J_{F/AF}\right) \frac{V}{t_{AF}} P(V) dV dJ_{F/AF} \qquad \text{(Eq. IV.2).}$$

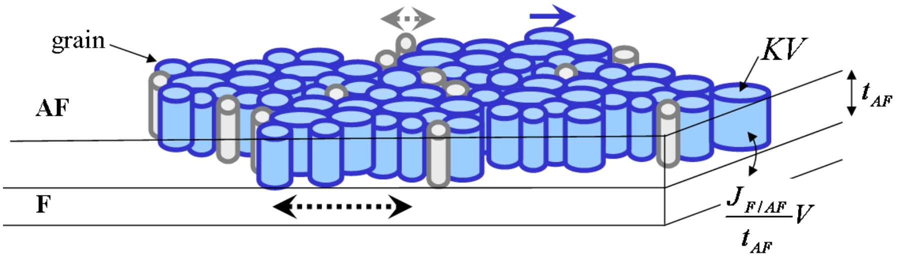

Figure 68 : Schematic diagram of a polycrystalline F/AF bilayer at a given temperature, T_M. To ease the reading, only the antiferromagnetic grains are sketched. The blue grains are pinned at T_M and contribute to exchange bias, in contrast to the grey grains [201].

IV.1.2 Blocking temperature distributions and typical experimental procedure

As mentioned in the introduction, exchange bias can be a useful tool to probe and study buried structural and interfacial properties of F/AF systems. To this end, we will discuss in the following subsection a specific procedure which measures the blocking temperature distributions, DT_B and allows for the quantification of both F/AF interfacial glassy character and antiferromagnetic grain stability. This procedure is based on the work of Soeya and coworkers [202] with an extension proposed by Baltz and coworkers [128].

The typical experimental procedure consists in applying incremental field cooling process, resulting in the gradual reorientation of the antiferromagnetic entities. As an illustration, Figure 69 shows typical hysteresis loops, measured at a fixed temperature, T_M=4K, in accordance to the specific procedure. It should be noted here that the term antiferromagnetic entities refers to both grains and disordered magnetic phases. In this process, the F/AF system is field cooled from a high temperature, well above the blocking temperature, $T_{B,max}$, down to T_M, under a positive magnetic field. As a consequence, all the antiferromagnetic spins are pointing in the same direction as the applied field, giving rise to a negative hysteresis loop shift, see full blue squares in Figure 69. Thereafter, the system is field cooled from an intermediate annealing temperature, T_a, down to T_M under a negative magnetic field. During this step, entities with $T_B < T_a$ reorient negatively while those with with $T_B > T_a$ stay oriented positively, resulting in a progressive sign change of exchange bias field, H_E (see open circles in Figure 69). The field cooling process from T_a, down to T_M under a negative magnetic field is repeated for incremental values of T_a until all the antiferromagnetic spins point towards the negative direction, as shown in Figure 69 (red stars). The corresponding change in the exchange bias field is used as a way to identify the antiferromagnetic entities affected by the field cooling procedure, having a T_B lower than the annealing temperature. Through this process, one is able to deduce the blocking temperature distributions of the F/AF system.

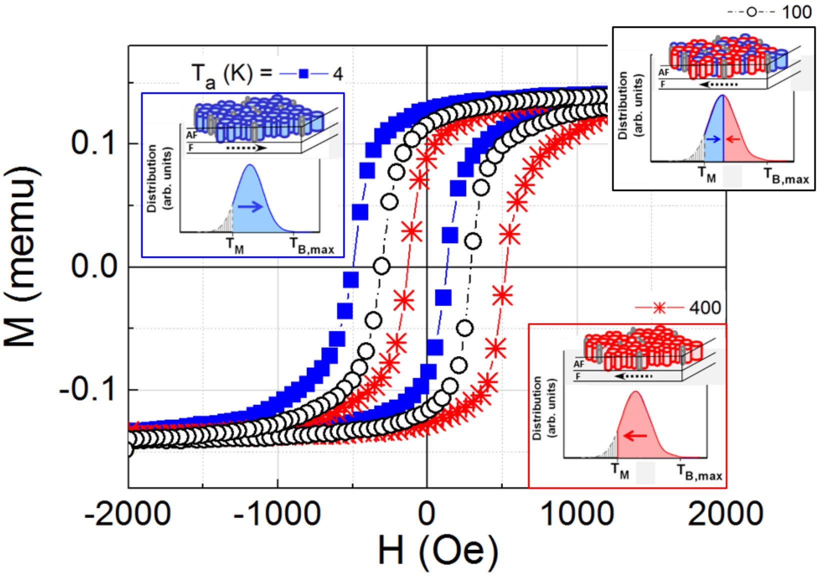

Figure 69 : Representative hysteresis loops measured along the field cooling direction by vibrating sample magnetometer, VSM at 4K, for a $Si/SiO_2/Ta3/Cu3/Co3/FeMn10/Pt2$ (nm) film. The measurements follow the procedure described in the text. The inset is a sketch representing the orientation of the antiferromagnetic entities and the blocking temperature distribution.

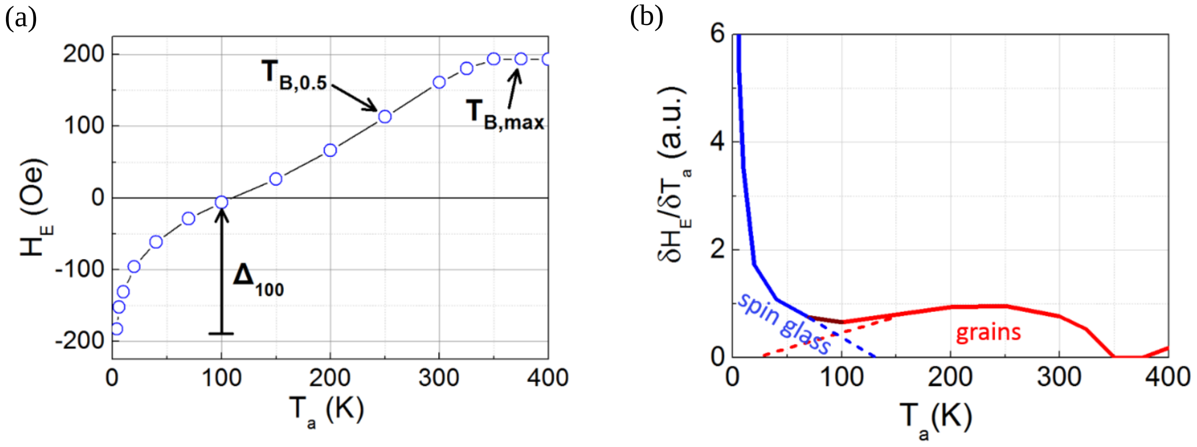

Figure 70 : Dependence of the normalized exchange bias loop shift measured at 4K on the annealing temperature, T_a for $Si/SiO_2/Ta3/Cu3/Co3/FeMn10/Pt2$ (nm). (b) Derivative of (a): this is the blocking temperature distribution; at low T is related to the spin glass whereas at high T to the grains.

Figure 70(a) shows the change of exchange bias field as a function of T_a. As expected H_E changes both in amplitude and sign with increasing Ta. The derivative $\delta H_E/\delta T_a$, shown in Figure 70(b), constitutes the blocking temperature distribution, DT_B of the F/AF system. Actually, for every increment of T_a, H_E integrates the antiferromagnetic entities still oriented positively (with T_B larger than T_a and unaffected by the negative FC from T_a down to 4K) minus those reoriented negatively (with T_B lower than T_a). Therefore, the plot of H_E vs. T_a (see Figure 70(a)) relates to the integral of the T_B distribution. As a result, a peak in the distribution reads as an inflection point in the H_E vs T_a plot and the surface of the corresponding peak is equal to the amplitude around the inflection point. The position of the peak (inflection point) is an indication of the thermal stability of the corresponding antiferromagnetic entities and the surface (amplitude around the inflection point) is proportional to the amount of antiferromagnetic entities. The T_B distributions consist of two contributions, namely the low-T contribution related to F/AF interfacial disordered magnetic phases and the high-T contribution which is associated with thermally activated reversal of the antiferromagnetic grains spin-lattice. The interfacial F/AF glassy character of the systems is denoted as Δ_{100}, which is represented with an arrow in the Figure 70(a). It represents the difference between H_E measured after T_a = 4 K and T_a = 100K. The larger the Δ_{100} the more glassy the interface is.

In the following, we will extract the values of Δ_{100} to compare the interfacial disordered magnetic phases between various structures. To ease the interpretation, such a comparison usually uses normalized data: Δ_{100}^* (or Δ^* to simplify the notation) equals Δ_{100} normalized to the total expected variations of H_E, i.e. 2 for normalized H_E: from -1 (when all the antiferromagnetic entities contributing to H_E at 4K are initially oriented positively) to 1 (when all the entities are reoriented negatively after completion of the FC procedure). We recall that when all the antiferromagnetic entities are reoriented, when T_a is equal to the maximum T_B, H_E reaches again its maximum amplitude but with opposite sign compared to the initial value of H_E and it then levels out (see Figure 70(a)). Contrary to Δ that characterizes the interface, $T_{B,max}$ is a good indicator of the antiferromagnetic grains volumes stability and refers to the maximum blocking temperature that is reached when H_E vs T_a saturates, see Figure 70(a). Nonetheless, $T_{B,max}$ cannot be reached for all our samples during the DT_B measurement, since our VSM equipment cannot reach temperatures higher than 400K. For this reason, we arbitrary picked $T_{B,0.5}$ to account for the antiferromagnetic volume (see arrow in Figure 70(a)).

IV.2 Importance of interfacial spatial dispersions for applications [5]

Spatial variability of magnetic properties refers to how the magnetic properties are distributed when measured at different spatial locations. In spintronic devices, the spatial variability of magnetic properties is a particularly serious issue which was observed after the arrival of the very first-generation of MRAM devices, see Chapter I.1. Since then it has received considerable attention by the scientific community. Most studies are focused on the variability of the shapes of memory bits, produced during the nanofabrication process. In general, the use of nanostructures calls for statistical representations, a need which becomes even more important when antiferromagnetic materials are getting involved. This is because both polycrystalline and epitaxial antiferromagnetic thin films are very sensitive to spin texture faults (due to roughness, atomic stacking faults, etc.) that create in turn randomly-spread disordered magnetic phases (see section IV.1.2).

In this work, we experimentally demonstrated that antiferromagnetic disordered magnetic phases, initially present in the continuous film, cause nanostructure-to-nanostructure dispersion of the antiferromagnet-related properties when the film is patterned. The latter gives rise to spatial variability of exchange bias related to the amount of disordered magnetic phases. It should be noted that the results discussed in this section were obtained in the frame of the PhD thesis of Kamil Akmaldinov (2012-2015) and the beginning of my master 2 thesis in 2014. This section is adapted from Ref. [5] where the main findings were published. In fact, it is added here in order to introduce the next section, IV.3.

Previous studies conducted at SPINTEC [133] suggested that mixed antiferromagnets, consisting of IrMn/FeMn multilayers, can be used in order to tune simultaneously the amount of disordered magnetic phases and the antiferromagnetic grains stability, which are specifically important for thermally-assisted MRAM, (TA)-MRAM applications, see Chapter I.1. In this section we will consider the impact of disordered magnetic phases, which exhibit low freezing temperatures and are located in the F/mixed-AF thin film, on the device-to-device variability of exchange bias in functional TA-MRAM.

The following multilayers are studied: CMOS//buffer/[AF_1/ Ru2/F_1]/MgO1.4/[F_2/AF_2]/thermal barrier/cap (nm), with AF_1 = PtMn20; F_1 = CoFeB1.2; F_2 = CoFeB2/NiFe1.5, and AF_2 = IrMn10; {IrMn1/FeMn1}×5, {FeMn1/IrMn1}×5 and FeMn10. CMOS stands for complementary metal-oxide semiconductor. The total thickness of AF_2 is kept constant. The multilayer structures are deposited by dc magnetron sputtering (at CROCUS Technology, a spin-off of SPINTEC) with an Ar pressure of 2.5×10^{-3} mbar onto 8-in standard CMOS wafers with typical pre-processed back-end transistors. Note that IrMn and FeMn are made from $Ir_{20}Mn_{80}$ and $Fe_{50}Mn_{50}$ targets (at. %) with 80 and 50 at.% of Mn respectively. Here, we specifically worked on the exchange bias properties of the F_2/AF_2 storage layer. Therefore, to ease the data interpretation and in contrast to the TA-MRAM final product [39], the [AF_1/Ru2/F_1] reference layer is downgraded to a simple free layer by decoupling AF_1 and F_1 with a thick Ru spacer. For similar reasons, we used ferromagnetic layers instead of synthetic-AF stacks.

The relative amount of disordered magnetic phases spread over the sheet wafer, Δ^*, is extracted following the experimental procedure presented in Chapter IV.1.2. For the structures under investigation, Δ^* is found to be 52, 40, 36, and 27%, corresponding to AF_2 = IrMn10; {IrMn1/FeMn1}×5, {FeMn1/IrMn1}×5, and FeMn10 (nm), respectively. These results are in agreement with previous findings [133] and are ascribed to the proportion of Mn atoms. It was inferred that the larger the amount of Mn atoms, the more glassy the interface. In particular, Mn atoms diffuse at the interface and create spin-glass phases [133]. Having verified the magnetic behavior of the sheet films, the wafers are processed using a standard cleanroom lithography and etching techniques (by CROCUS Technology partner). The two series of TA-

MRAM chips obtained have circular magnetic cells with a diameter of 180 and 240 nm. Figure 71(a) is a transmission electron microscopy, TEM, cross section showing two of our magnetic memory cells sandwiched between two metallic contacts, M3 and M4 (dark contrast), surrounded by an insulator (bright contrast). The metallic contacts connect the magnetic stack to the bit-lines and word-lines. The electrical properties of the individual memory cells of the chips are tested at room temperature using an automated electrical prober: a bias voltage of 50 mV is applied between the bit-lines and word-lines to read the resistance (R) and external coils are used to sweep the magnetic field (H) between ±800 Oe. As a result, for each one of the four multilayer compositions, we obtain two sets of approximately two hundred R versus H loops: one for the 180 nm cells and one for the 240 nm cells.

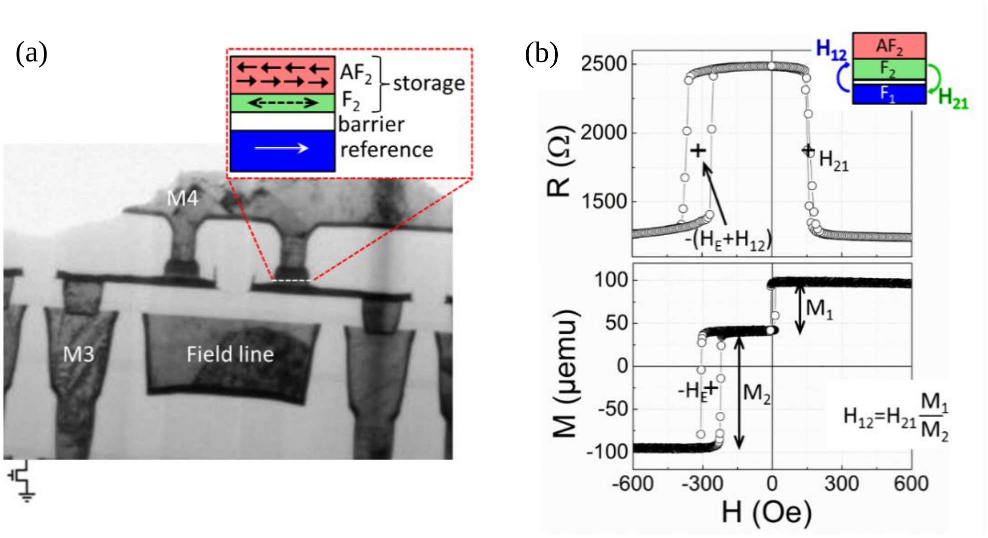

Figure 71 : (a) Transmission electron microscopy, TEM cross-section zoomed on two magnetic memory cells of a typical TA-MRAM chip on CMOS. (b) Top: resistance, R versus magnetic field, H for a TA-MRAM circular cell with a diameter of 140 nm and with composition: CMOS // buffer / [AF_1/Ru2/F_1] / MgO1.4 / [F_2/AF_2] / cap (nm), with AF_1 = PtMn20; F_1 = CoFeB1.2; F_2 = CoFeB2/NiFe1.5 and AF_2 = FeMn10. From Ref. [5].

Figure 71(b) shows a typical R versus H loop, as well as a typical hysteresis loop of M versus H, both measured by VSM at room temperature, for the corresponding sheet film. It is reasonable to assume that the layers are conformal in shape. From simple considerations, it results that the ratio between stray fields from one layer to another (H_{12}/H_{21}) is equal to the ratio between the layer magnetizations (M_1/M_2). This latter ratio is deduced from the VSM measurement of the sheet film. For every memory cell, it is thus possible to extract the exchange bias field from the R versus H data, with $H_E = (H_E + H_{12}) - H_{21} \times (M_1/M_2)$.

We performed cumulative frequency analysis on the cell-to-cell distribution of H_E over the TA-MRAM chips. Figure 72(a) shows the cumulative distribution functions, CDF versus H_E for the four TA-MRAM chips, all four having different AF_2 layers. Note that a data point in the graph corresponds to a measurement of one TA-MRAM cell. The graph reads as follows: for AF_2 =

IrMn10, when the cumulative distribution equals 30%, the corresponding value of H_E is 135 Oe. In practice this means that 30% of the cells have a value of H_E less than 135 Oe. The value of H_E with an occurrence of 50%, $H_{E,50\%}$ is indicated in Figure 72(a) for AF_2 = IrMn10. The main point here is how the exchange bias loop shift dispersion differs between the various AF_2 layers. Figure 72(b) shows the cumulative distributions versus H_E normalized to $H_{E,50\%}$, which allows comparing the cumulative distributions for the four different compositions. The standard deviations, σ_{HE} of these curves account for the cell-to-cell variability of H_E. This latter seems to be larger when the AF_2 layer evolves from pure FeMn to pure IrMn. In order to quantitatively analyze such a cell-to-cell variability of H_E, we calculated σ_{HE}. Figure 73(a) summarizes for the four AF_2 layer compositions, the amount of disordered magnetic phases, Δ^* deduced from blocking temperature distributions measurements on the sheet wafers (left axis) and shows σ_{HE} over the TA-MRAM cells of the chips (right axis). The graph shows that tuning the AF_2 layer composition allows us controlling the amount of disordered magnetic phases.

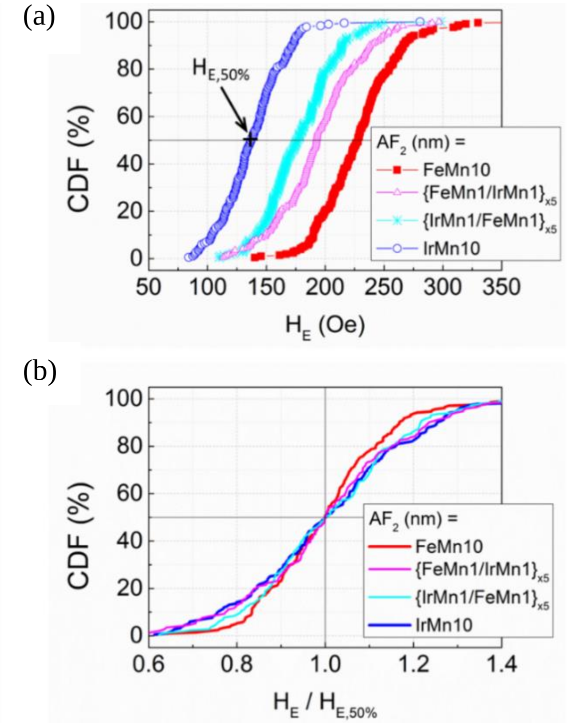

Figure 72 : For TA-MRAM chips, cumulative distribution function of hysteresis loop shift (CDF) over TA-MRAM cells as a function of: (a) the hysteresis loop shift (H_E) and (b) the normalized hysteresis loop shift ($H_E/H_{E,50\%}$) . From Ref. [5].

From Figure 73(a), we see that the two dependences of σ_{HE} with the AF_2 layer composition follow the same trend as that Δ^*, except in the case of AF_2 = FeMn/IrMn with 180 nm cells. It should be noted here that, the FeMn/IrMn and IrMn/FeMn multilayers resemble more FeIrMn alloys than laminated structures [133], which is supported by the fact that the values of Δ^* and σ_{HE} are close for both structures. The interplay between the amount of disordered magnetic phases, measured at the sheet film level, and cell-to-cell variability of H_E in TA-MRAM processed chips is better visible in Figure 73(b), which shows σ_{HE} versus Δ^*. Essentially, the disordered magnetic phases, resulting from magnetic frustrations, are spread over the wafer and, thus, over the memory cells after nanofabrication as shown in Figure 73(c). Cells with more of such disordered magnetic phases are more prone to thermal activation as the F/AF interfacial coupling is disrupted on a large part of the cell area, resulting in a weaker hysteresis loop shift. By applying a linear regression on the data points of Figure 73(b), we extrapolated a value of σ_{HE} which equals 8% when Δ^* tends to 0. This may give an estimate for the part of the cell-to-cell variability of H_E that is independent on the disordered magnetic phases. This independent part likely originates from process-induced variability in, for example, cell sizes and shapes [203]. The fact that all of our four samples were subject to the same process flow suggests that such types of variability are independent on the sample. Although Figure 73(b) shows that the amount of disordered magnetic phases influences the variability of H_E, finding the exact ratio between these two parameters is not straightforward and trying to push the analysis to a further quantitative level would probably be misleading.

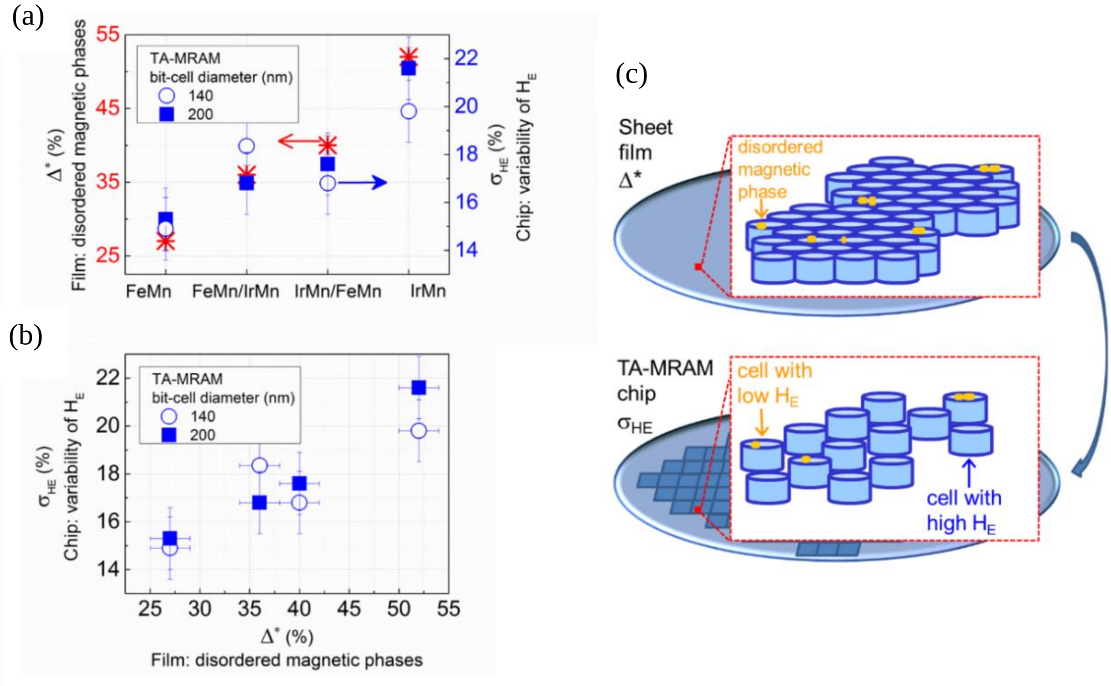

Figure 73 : (a) For the four corresponding compositions, amount of disordered magnetic phases, Δ^* in the sheet wafers and the cell-to-cell variability σ_{HE} over the ~200 cells of TA-MRAM chips with cells diameters of 140 and 200 nm (b) σ_{HE} vs Δ^*. (c) Sketch showing the spread of disordered magnetic phases (orange dots) over a polycrystalline film on a sheet wafer and the resulting TA-MRAM cell-to-cell variability of exchange bias after patterning the sheet film in the form of memory cells. Here, to ease the reading, a grain (blue cylinder) defines a cell although in reality each cell contains tenth of grains. From Ref. [5].

In conclusion, we have experimentally demonstrated the correlation between the amount of disordered magnetic phases spread over F/AF thin films and the device-to-device variability of exchange bias in magnetic applications. For the specific field of TA-MRAM, this brings about an alternative method for the qualification of magnetic stacks before launching a full nanofabrication process. The latter can also potentially be used in the field of antiferromagnetic spintronics, for instance when dealing with the interaction between a current and an antiferromagnetic material in a nanostructure. In general, the spatial variability factor, through statistical analysis, is of big importance as it can help avoid drawing conclusions based on potentially misleading individual events. From the moment that arrays of nanostructures are involved, statistical analysis should be performed.

IV.3 Tuning the bulk contribution without affecting the interface [6]

Would it be possible to adjust the bulk properties of an antiferromagnetic layer by changing its antiferromagnetic nature but without affecting its interface? This question was initially raised for the case of TA-MRAM applications, but it can also apply in antiferromagnetic spintronics. One of the key challenges for antiferromagnet-based devices is to preserve the integrity of the antiferromagnetic interface so as to reduce the device-to device variability, (see section IV.2) while at the same time reassuring low write power consumption as well as data retention. In this spirit, we combined here $Fe_{50}Mn_{50}$ and $Ir_{20}Mn_{80}$, two commonly used antiferromagnets in industry, in order to exploit the advantages of both antiferromagnets; FeMn's good interfacial properties and IrMn's higher thermal stability. Nonetheless, simply laminating FeMn and IrMn layers (as shown in section IV.2) is not sufficient since it provides intermediate properties between FeMn and IrMn for both the disordered phases (Δ) and the thermal stability (related to T_B) [133]. Since Mn diffusion is a known source of disordered magnetic phases, reducing as much as possible the Mn-content or adding diffusion barriers to avoid Mn-diffusion are some of the possible pathways to reduce the subsequent variability of exchange bias properties in devices. Actually, through its affinity with Mn, it was previously demonstrated that Pt acts as a good diffusion barrier for Mn. To this end, we will examine in the following section the impact of Pt layer to the Mn diffusion in AF layer consisting of FeMn/Pt/AF.

The results of this section were published in Ref. [6].

The specimens are deposited on thermally oxidized silicon substrates, Si/SiO_2, using a magnetron sputtering machine with an argon plasma. The multilayers consist of Si/SiO_2//Ta3/Cu3/Co3/AF/Pt2(nm). A tantalum/copper bilayer, Ta3/Cu3, is used as buffer and a cap of 2 nm of platinum, Pt2, prevents oxidation of the specimens. The active magnetic stacks consist of different antiferromagnetic structures coupled to the same ferromagnetic material: here, 3 nm of cobalt: Co3. The antiferromagnetic structures are split in two groups, depending on whether it is FeMn or IrMn which is in contact with Co at the F/AF interface: AF = FeMn10, FeMn2/Pt0.4/(IrMn1/FeMn1)x4, FeMn2/Pt0.4/IrMn8; and AF = IrMn10. The overall thickness of the antiferromagnetic layer is kept constant at 10 nm. In the absence of a diffusion barrier to Mn, IrMn/FeMn interfaces mix. Thus, the (IrMn1/FeMn1)x4 multilayer resembles more an IrFeMn alloy [133] than a laminated structure. To preserve the integrity of the antiferromagnetic layer at the interface with the ferromagnet, we inserted a Pt spacer that acts as a diffusion barrier/getter to Mn [204,205]. It is however thin enough, 0.4 nm, to ensure the magnetic coupling between the antiferromagnetic layers situated on both sides. Note that the antiferromagnetic structures are grown on top of the ferromagnetic layer, so as to avoid any growth variability between the various antiferromagnetic structures.

We followed the experimental procedure described in Chapter IV.1.2. The values accounting for the contribution of the interfacial disordered magnetic phases, Δ_{100}^{*}, and the thermal stability of the antiferromagnetic grains, $T_{B,0.5}$, are plotted in Figure 74 for the various Co/AF structures. While the thermal stability of the antiferromagnetic grains, $T_{B,0.5}$, evolves gradually from sample to sample, the contribution of the interfacial disordered magnetic phases, Δ_{100}^{*}, seems to show slightly distinct behaviors depending on whether a Co/IrMn interface is considered, for AF = IrMn10, or a Co/FeMn is used for AF =FeMn2/Pt0.4/IrMn8, FeMn2/Pt0.4/(IrMn1/FeMn1)x4, and FeMn10. It should be noted that FeMn2/Pt0.4/(IrMn1/FeMn1)x4 can also be written as FeMn2/Pt0.4/IrFeMn8 since IrMn/FeMn are known to resemble more IrFeMn alloys, with intermediate properties between IrMn and FeMn [133], than laminated structures. For consistency, FeMn10 will also be written FeMn2/FeMn8.

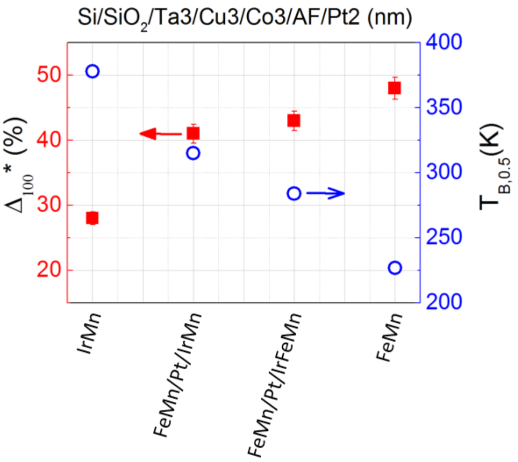

Figure 74 : Comparison of the contribution of the disordered magnetic phases at the F/AF interface ($\Delta_{100*} = \Delta_{100/2}$) and of the thermal stability of the AF grains, $T_{B,0.5}$, for Si/SiO$_2$//Ta3/Cu3/Co3/AF/Pt2 (nm) multilayers with various composite AF materials: AF (nm) = IrMn10, FeMn2/Pt0.4/IrMn8, FeMn2/Pt0.4/(IrMn1/FeMn1)x4 and FeMn10. From Ref. [6].

For a constant F/AF interface and various antiferromagnetic bulks, the differences in the thermal stability of the antiferromagnetic grains mostly relate to the differences in the antiferromagnetic volume times the magnetic anisotropy product [128,206]. As a first approximation, this explains the variation of $T_{B,0.5}$. The bulk IrMn8 for instance shows grains with smaller volumes compared to a thicker IrMn10 layer. It is known from the literature [206] that the grains' diameter may increase when increasing the thickness of the layer, which cannot be excluded in our case. Second, earlier x-ray diffraction measurements for similar samples confirmed that, in this range of thicknesses, the vertical coherence length of the structure of the grains is equal to the IrMn thickness. This was obtained by fitting the full width at half maximum of the IrMn (111) specular peak with the Scherrer formula. Thus, increasing the thickness of the layer also increases the volume of the grains. On the other hand, the FeMn grains are less stable than IrMn grains, likely due to a smaller anisotropy. As mentioned previously the grains in the laminated IrMn/FeMn layers are expected to show intermediate thermal stabilities between IrMn and FeMn grains [133]. Here however, this simple picture is probably more complex. Although the samples with AF = FeMn2/Pt0.4/IrMn8, FeMn2/Pt0.4/IrFeMn8, and FeMn2/FeMn8 have the same Co/FeMn interface, the respective coupling to the FeMn2 interface of the IrMn8 and IrFeMn8 bulks are done across a thin Pt layer of 0.4 nm for the first two compositions in contrast to the last composition where the FeMn8 bulk directly couples to the FeMn2 interface. This may also explain the fact that the values of Δ_{100}^* for these three samples are not strictly the same.

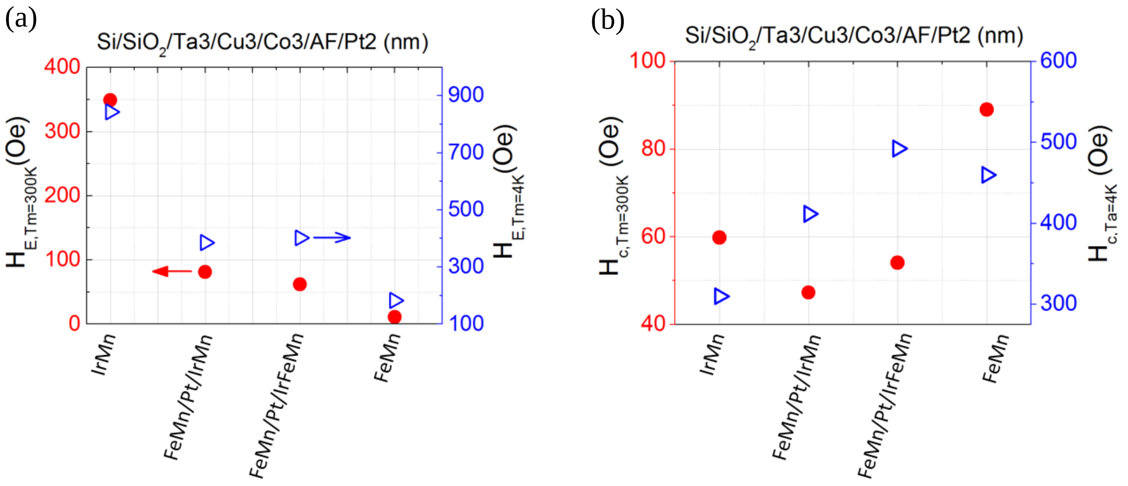

Figure 75 : (a) Exchange bias and (b) coercive fields measured at T_M= 4 and 300 K for Si/SiO$_2$/Ta3/Cu3/Co3/AF/Pt2 (nm) multilayers with various composite AF materials: AF (nm) = IrMn10, FeMn2/Pt0.4/IrMn8, FeMn2/Pt0.4/(IrMn1/FeMn1)x4 and FeMn10. From Ref. [6].

Figure 75(a) and (b) shows the hysteresis loop shift, H_E, and the coercive field, H_C, respectively, both measured at 4 and 300K for the various Co/AF structures. Although H_E seems to follow distinct behaviors depending on whether Co is in contact with IrMn or FeMn at the interface, the values of H_E and H_C also depends on other materials parameters, such as the F/AF interfacial exchange stiffness and the amplitude of the antiferromagnetic moments. Another parameter that needs to be considered is the amount of antiferromagnetic entities remaining fixed during the magnetization reversal of the ferromagnetic layer and that relate to both the interface, the antiferromagnetic bulk and the connection between the two. Most importantly, these parameters depend on temperature. At 300K, the case is complex since only part of the distribution is integrated: only the antiferromagnetic grains with T_B larger than 300K remain fixed. In contrast, at 4K, the antiferromagnetic entities, interfacial disordered magnetic phases and antiferromagnetic grains, are fixed since all the distribution is integrated (only the few and smallest interfacial disordered magnetic phases with T_B smaller than 4K do not contribute to H_E).

In conclusion, by changing the nature of the antiferromagnetic material in F/AF bilayers, we showed that it is possible to tune the antiferromagnetic volume contribution to exchange bias without affecting much the F/AF interface. To achieve so, we engineered composite antiferromagnetic materials using FeMn and IrMn alloys in which we inserted a thin Pt diffusion/trap barrier to Mn in order to preserve as much as possible the integrity of the antiferromagnetic layer at the interface. Although materials engineering is still needed to match all the requirements for applications, our results mean that it is a priori possible to find antiferromagnetic materials with various intrinsic properties such as T_N (i.e. at a TA-MRAM level with various write power) without affecting the F/AF interface (i.e. without affecting the cell-to-cell variability of the exchange bias properties in MRAM chips).

IV.4 Influence of heavy metal insertion on antiferromagnetic properties [7]

Chapter IV.2 and IV.3 showed that it is possible to tune the interfacial properties in F/AF systems by using mixed/composite antiferromagnetic structures. In this section, in the same context, we demonstrate that IrMn/Pt multilayers can be used in order to tune the surface to volume contribution of the antiferromagnetic properties so as to possibly enhance the interfacial spin-orbit coupling, SOC. It should be noted that the results discussed in this section are in the frame of the Post-doctoral project of Guillaume Forestier (2016-2018). The chapter is adapted from Ref. [7] where the main findings were summarized.

Recent studies [20,47,49] have highlighted the leading role of spin-orbit coupling as well as its high potential prospects for realizing pure antiferromagnetic spintronics and more specifically in the direction of tunnelling anisotropic magnetoresistance, TAMR devices, see Chapter I.2. To achieve high tunnel anisotropic magnetoresistance signals a large spin-orbit coupling and large spontaneous moments are necessary [47]. To this end, we will show here how and up to what extent the magnetic properties of antiferromagnetic materials shall and can be adjusted for use as functional materials. Here we determined how heavy metal (Pt) insertion in the bulk influences the antiferromagnetic properties of an IrMn layer. Series consisting of NiFe(8)/[IrMn(t_{IrMn})/Pt(t_{Pt})]x10 and [Pt(1)/Co(0.5)]x4/[IrMn(t_{IrMn})/Pt(t_{Pt})]x10 (nm) multilayers were grown by sputtering. The IrMn and Pt thicknesses were adjusted between 0 and 0.6 nm in order to vary the IrMn to Pt ratio.

The [IrMn/Pt] antiferromagnets were exchange biased to ferromagnetic NiFe and [Pt/Co] layers with in-plane and out-of-plane anisotropy, respectively. For all our samples, the hysteresis loops were measured at various temperatures from 4 to 300 K. The temperature dependence of the hysteresis loop shift and coercive field are shown in the Figure 76. The low-temperature contribution is observed for all samples, which corresponds to the sharp decrease of H_E as T increases between 4 and 25 K. Note that compared to the previous procedure, these data include thermal variations of K, M_s etc, but still it is possible to draw some qualitative conclusion at the expense of lengthy procedures. Adding Pt increases the amplitude of the low-temperature contribution, which demonstrates the presence of more interfacial disordered magnetic phases, likely due to more intermixing up to the interface. The high-temperature contribution corresponds to H_E further decreasing towards zero, present for all our samples. Adding Pt therefore shifts the high-temperature contribution towards smaller temperature indicating an alteration of IrMn grains' properties. The results are similar whether the ferromagnet has in-plane or out-of-plane anisotropy, showing that the observations relate to the [IrMn/Pt] antiferromagnetic material. To conclude, we found that inserting layers made of a heavy element (Pt) in the bulk of an IrMn antiferromagnet provides a way to tune the surface to volume contribution of the antiferromagnetic properties. This could further be used as a knob to tune and study electrical properties. Some of these samples are being processed in order to study the influence of Pt heavy metal doping on the tunnel anisotropic response of IrMn antiferromagnets

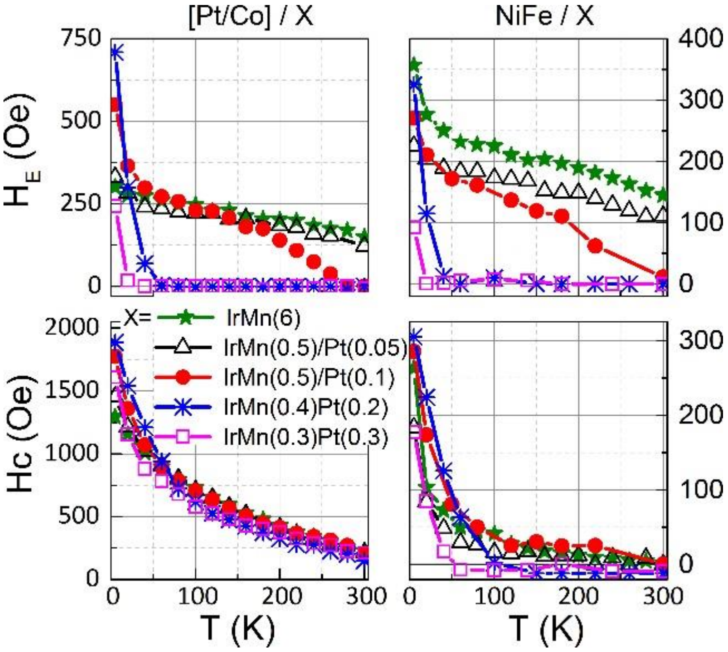

Figure 76 : Temperature-dependence of hysteresis loop shift and coercive field for NiFe8/[IrMn(tI_{rMn})/Pt(t_{Pt})]x10 (Left) and [Pt1/Co0.5]x4/[IrMn(t_{IrMn})/Pt(t_{Pt})]x10 (nm) multilayers (Right).

Summary

In the context of antiferromagnetic spintronics we have presented here a way to manipulate the spatial dispersion of antiferromagnetic properties in spintronic devices, by minimizing the amount of the interfacial disordered magnetic phases. At the same time we showed how to reduce such dispersions and improve simultaneously the thermal stability of the antiferromagnet. And finally, we demonstrated how and up to what extent it is possible to dope an antiferromagnet with a heavy element in order to potentially boost its spin-orbit coupling.

Conclusion

A better understanding of the antiferromagnetic spin dependent transport properties is necessary for the future development of antiferromagnet-based spintronic devices. In this direction, this thesis investigated spin current injection, transmission and detection in antiferromagnets, in an effort to determine some of the basic parameters specific to these magnetic materials. In particular, we studied the spin-pumping effect by means of ferromagnetic resonance technique in systems consisting of a spin injector / (spin conductor) / spin sink. NiFe was used as the spin injector and metallic IrMn and insulating NiO and NiFeOx as the spin sink. The results revealed a novel spin pumping effect at the antiferromagnetic-to-paramagnetic phase transition, due to linear magnetic fluctuations, that further confirmed the theoretical prediction by Ohnuma *et al.* [124]. Remarkably, it was shown that the effect does not depend on the electrical state of the antiferromagnet and it is equally present in both metallic and insulating antiferromagnets. Such an effect opens new opportunities for more efficient spin pumping, while at the same time providing an innovative desktop microprobe for critical temperatures, in ultrathin films. More experiments including various antiferromagnets, like Tb and Cr, fabricated by our collaborators at LPS in Orsay, are envisioned to further prove the universality of spin pumping as a versatile method to probe phase transitions.

Within the scope of this thesis, we further investigated the role of exchange bias on spin current absorption by antiferromagnetic spin sinks and especially at their critical temperature. As a matter of fact, we demonstrated that the exchange bias defines the nature of spin transport, whether it is an electronic or magnonic transport or a combination of both, and acts as an efficient spin current amplifier. Currently, more systematic studies are conducted in the group, along with the development of a theoretical model by our collaborators at the University of Mainz, in order to elucidate the physics of enhanced spin pumping via exchange coupling.

Next, we investigated the electrical detection of spin currents in IrMn, in an attempt to probe electrically linear as well as non-linear fluctuations at the magnetic phase transition. The experiments were conducted in a spin Hall geometry, where spin current was generated by spin pumping. A novel non-monotonous temperature dependence of transverse dc voltage appeared for all IrMn thicknesses. Nonetheless, the effect was equally present in the case of bare NiFe, suggesting that it is mostly related to the spin injector itself. This enhancement overshadowed the effects associated to the antiferromagnetic spin sink, but triggered interest towards spin current detection in ferromagnets. To further investigate the nature of this effect, we tried different NiFe thicknesses. The amplitude of the generated dc voltage showed a peak at 16 nm of NiFe layer. Further investigations are performed in the group to shed light into the physical origin of the enhanced dc voltage. Note that we also tested CoFeB as spin injector. The results revived hope for possible electrical detection of spin currents and spin fluctuations in antiferromagnets, as a peak appears at the magnetic phase transition of IrMn. More systematic work is undertaken to draw conclusions on the effects of linear and nonlinear antiferromagnetic fluctuations on the inverse spin Hall effect.

In the last chapter, we used exchange bias as a mean to investigate and further engineer the magnetic and electric properties of different metallic antiferromagnets, IrMn and FeMn, which are commonly used in spintronic devices. From a technological point of view, it is important to minimize the spatial dispersion of antiferromagnetic properties, as it can significantly affect the functionalities of the device. A leading source of spatial dispersion of antiferromagnetic properties is the presence of interfacial disordered magnetic phases. Here, we demonstrated a way to reduce such dispersions and improve simultaneously the thermal stability of the antiferromagnet. In the same context, we investigated possible ways to augment the IrMn spin-orbit coupling, which is of particular importance for tunneling anisotropic magnetoresistance devices. The insertion of Pt layer altered the surface to volume contribution of the IrMn properties that could be used in the future as an alternative way to tune its electrical properties.

In the emerging field of antiferromagnetic spintronics much remain to be done to bear the promise of highly functional pure antiferromagnet-based devices. Various fields of condensed matter physics are still unexploited and ask for deeper investigation. The manipulation of antiferromagnetic domain walls, as well as the use of antiferromagnetic topological insulators fall into this category of current and future studies.

Bibliography

[1] L. Frangou, S. Oyarzún, S. Auffret, L. Vila, S. Gambarelli, V. Baltz, Enhanced Spin Pumping Efficiency in Antiferromagnetic IrMn Thin Films around the Magnetic Phase Transition, Phys. Rev. Lett. 116 (2016) 77203.

[2] L. Frangou, O. Gladii, G. Forestier, K. Yamamoto, J. Sinova, H. Gomonay, V. Baltz, Electronic versus magnonic spin transport in antiferromagnets, Unpublished. (2017).

[3] L. Frangou, G. Forestier, S. Auffret, S. Gambarelli, V. Baltz, Relaxation mechanism driven by spin angular momentum absorption throughout antiferromagnetic phase transition in NiFe surface oxides, Phys. Rev. B. 95 (2017) 54416.

[4] L. Frangou, O. Gladii, G. Forestier, S. Auffret, U. Ebels, S. Gambarelli, V. Baltz, Unravelling the effects associated with ferromagnetic dynamics in non-magnet/ferromagnet metallic multilayers, Unpublished, see also Abstr. Colloq. Louis Néel. (2017).

[5] K. Akmaldinov, L. Frangou, C. Ducruet, C. Portemont, J. Pereira, I. Joumard, B. Dieny, J. Alvarez-Hérault, V. Baltz, Correlation Between Disordered Magnetic Phases in Ferromagnetic/Antiferromagnetic Thin Films and Device-to-Device Variability of Exchange Bias in Spintronic Applications, IEEE Magn. Lett. 6 (2015) 3000404.

[6] L. Frangou, K. Akmaldinov, C. Ducruet, I. Joumard, B. Dieny, V. Baltz, Tuning the granular contribution to exchange bias by varying the antiferromagnetic material but without affecting the ferromagnetic/antiferromagnetic interface, Phys. Procedia. 75 (2015) 1058.

[7] G. Forestier, L. Frangou, Y. Wen, S. Auffret, X. Zhang, A. Manchon, V. Baltz, Influence of Pt layer insertion on IrMn antiferromagnetic properties, Unpublished, see also Abstr. Intermag. (2017).

[8] M.N. Baibich, J.M. Broto, A. Fert, F.N. Van Dau, F. Petroff, P. Etienne, G. Creuzet, A. Friederich, J. Chazelas, Giant magnetoresistance of (001)Fe/(001)Cr magnetic superlattices, Phys. Rev. Lett. 61 (1988) 2472.

[9] G. Binasch, P. Grünberg, F. Saurenbach, W. Zinn, Enhanced magnetoresistance in layered magnetic structures with antiferromagnetic interlayer exchange, Phys. Rev. B. 39 (1989) 4828.

[10] I. Žutić, J. Fabian, S. Das Sarma, Spintronics: Fundamentals and applications, Rev. Mod. Phys. 76 (2004) 323.

[11] B. Dieny, R.B. Goldfarb, K.-J. Lee, Introduction to magnetic random-access memory, Wiley-IEEE Press. (2017).

[12] A. Kohn, A. Kovács, R. Fan, G.J. McIntyre, R.C.C. Ward, J.P. Goff, The antiferromagnetic structures of IrMn3 and their influence on exchange-bias, Sci. Rep. 3 (2013) 2412.

[13] T. Kampfrath, A. Sell, G. Klatt, A. Pashkin, S. Mährlein, T. Dekorsy, M. Wolf, M. Fiebig, A. Leitenstorfer, R. Huber, Coherent terahertz control of antiferromagnetic spin waves, Nat. Photonics. 5 (2011) 31.

[14] P. Wadley, V. Hills, M.R. Shahedkhah, K.W. Edmonds, R.P. Campion, V. Novák, B. Ouladdiaf, D. Khalyavin, S. Langridge, V. Saidl, P. Nemec, A.W. Rushforth, B.L. Gallagher, S.S. Dhesi, F. Maccherozzi, J. Železný, T. Jungwirth, Antiferromagnetic structure in tetragonal CuMnAs thin films, Sci. Rep. 5 (2015) 17079.

[15] J. Nogués, I.K. Schuller, Exchange bias, J. Magn. Magn. Mater. 192 (1999) 203.

[16] A.E. Berkowitz, K. Takano, Exchange anisotropy—a review, J. Magn. Magn. Mater. 200 (1999) 552.

[17] J. Železný, H. Gao, K. Výborný, J. Zemen, J. Mašek, A. Manchon, J. Wunderlich, J.

Sinova, T. Jungwirth, Relativistic Néel-Order Fields Induced by Electrical Current in Antiferromagnets, Phys. Rev. Lett. 113 (2014) 157201.

[18] P. Wadley, B. Howells, J. Železný, C. Andrews, V. Hills, R.P. Campion, V. Novák, K. Olejnik, F. Maccherozzi, S.S. Dhesi, S.Y. Martin, T. Wagner, J. Wunderlich, F. Freimuth, Y. Mokrousov, J. Kuneš, J.S. Chauhan, M.J. Grzybowski, A.W. Rushforth, K.W. Edmonds, B.L. Gallagher, T. Jungwirth, Electrical switching of an antiferromagnet, Science. 351 (2016) 558.

[19] X. Marti, I. Fina, C. Frontera, J. Liu, P. Wadley, Q. He, R.J. Paull, J.D. Clarkson, J. Kudrnovský, I. Turek, J. Kuneš, D. Yi, J.-H. Chu, C.T. Nelson, L. You, E. Arenholz, S. Salahuddin, J. Fontcuberta, T. Jungwirth, R. Ramesh, Room-temperature antiferromagnetic memory resistor, Nat. Mater. 13 (2014) 367.

[20] B.G. Park, J. Wunderlich, X. Marti, V. Holý, Y. Kurosaki, M. Yamada, H. Yamamoto, A. Nishide, J. Hayakawa, H. Takahashi, A.B. Shick, T. Jungwirth, A spin-valve-like magnetoresistance of an antiferromagnet-based tunnel junction, Nat. Mater. 10 (2011) 347.

[21] A.H. MacDonald, M. Tsoi, Antiferromagnetic metal spintronics, Philos. Trans. R. Soc. 369 (2011) 3098.

[22] T. Jungwirth, X. Marti, P. Wadley, J. Wunderlich, Antiferromagnetic spintronics, Nat. Nanotechnol. 11 (2016) 231.

[23] O. Gomonay, T. Jungwirth, J. Sinova, Concepts of antiferromagnetic spintronics, Phys. Status Solidi - RRL. 11 (2017) 1700022.

[24] V. Baltz, A. Manchon, M. Tsoi, T. Moriyama, T. Ono, Y. Tserkovnyak, Antiferromagnetic spintronics, Rev. Mod. Phys. in press, see also arXiv:1606.04284 (2016).

[25] H. V Gomonay, V.M. Loktev, Spintronics of antiferromagnetic systems, Low Temp. Phys. 40 (2014) 17.

[26] J.B.S. Mendes, R.O. Cunha, O. Alves Santos, P.R.T. Ribeiro, F.L.A. Machado, R.L. Rodriguez-Suárez, A. Azevedo, S.M. Rezende, Large inverse spin Hall effect in the antiferromagnetic metal Ir20Mn80, Phys. Rev. B. 89 (2014) 140406.

[27] H. Wang, C. Du, P.C. Hammel, F. Yang, Antiferromagnonic Spin Transport from Y3Fe5O12 into NiO, Phys. Rev. Lett. 113 (2014) 97202.

[28] C. Hahn, G. De Loubens, V. V Naletov, J. Ben Youssef, O. Klein, M. Viret, Conduction of spin currents through insulating antiferromagnetic oxides, Europhys. Lett. 108 (2014) 57005.

[29] W. Zhang, M.B. Jungfleisch, W. Jiang, J.E. Pearson, A. Hoffmann, F. Freimuth, Y. Mokrousov, Spin hall effects in metallic antiferromagnets, Phys. Rev. Lett. 113 (2014) 196602.

[30] W.T. Soh, Y. Yeow, X. Zhong, C.K. Ong, Inverse spin Hall effect of antiferromagnetic MnIr in exchange biased NiFe/MnIr films, J. Phys. D. Appl. Phys. 48 (2015) 345002.

[31] P. Merodio, A. Ghosh, C. Lemonias, E. Gautier, U. Ebels, M. Chshiev, H. Béa, V. Baltz, W.E. Bailey, Penetration depth and absorption mechanisms of spin currents in Ir20Mn80 and Fe50Mn50 polycrystalline films by ferromagnetic resonance and spin pumping, Appl. Phys. Lett. 104 (2014) 32406.

[32] C. Du, H. Wang, F. Yang, P.C. Hammel, Systematic variation of spin-orbit coupling with d-orbital filling: Large inverse spin Hall effect in 3d transition metals, Phys. Rev. B. 90 (2014) 140407.

[33] R. Acharyya, H.Y.T. Nguyen, W.P. Pratt, J. Bass, Spin-Flipping Associated With the Antiferromagnet IrMn, IEEE Trans. Magn. 46 (2010) 1454.

[34] C. Chappert, A. Fert, F.N. Van Dau, The emergence of spin electronics in data storage, Nat. Mater. 6 (2007) 813.

[35] S. Parkin, X. Jiang, C. Kaiser, A. Panchula, K. Roche, M. Samant, Magnetically engineered spintronic sensors and memory, Proc. IEEE. 91 (2003) 661.

[36] J.-G. Zhu, New heights for hard disk drives, Mater. Today. 6 (2003) 22.

[37] D. Apalkov, B. Dieny, J.M. Slaughter, Magnetoresistive Random Access Memory, Proc. IEEE. 104 (2016) 1796.

[38] I.L. Prejbeanu, M. Kerekes, R.C. Sousa, H. Sibuet, O. Redon, B. Dieny, J.-P. Nozières, Thermally assisted MRAM, J. Phys. Condens. Matter. 19 (2007) 165218.

[39] I.L. Prejbeanu, S. Bandiera, J. Alvarez-Hérault, R.C. Sousa, B. Dieny, J.-P. Nozières, Thermally assisted MRAMs: ultimate scalability and logic functionalities, J. Phys. D. Appl. Phys. 46 (2013) 74002.

[40] P. Nemec, M. Fiebig, T. Kampfrath, A. V. Kimel, Antiferromagnetic opto-spintronics: Part of a collection of reviews on antiferromagnetic spintronics, arXiv:1705.10600. (2017).

[41] T. Moriyama, N. Matsuzaki, K.J. Kim, I. Suzuki, T. Taniyama, T. Ono, Sequential write-read operations in FeRh antiferromagnetic memory, Appl. Phys. Lett. 107 (2015) 122403.

[42] D. Kriegner, K. Výborný, K. Olejnik, H. Reichlova, V. Novak, X. Marti, J. Gazquez, V. Saidl, P. Nemec, V. V Volobuev, G. Springholz, V. Holy, T. Jungwirth, Multiple-stable anisotropic magnetoresistance memory in antiferromagnetic MnTe, Nat. Commun. 7 (2016) 11623.

[43] H.-C. Wu, M. Abid, A. Kalitsov, P. Zarzhitsky, M. Abid, Z.-M. Liao, C.Ó. Coileáin, H. Xu, J.-J. Wang, H. Liu, O.N. Mryasov, C.-R. Chang, I.V. Shvets, Anomalous Anisotropic Magnetoresistance of Antiferromagnetic Epitaxial Bimetallic Films: Mn2Au and Mn2Au/Fe Bilayers, Adv. Funct. Mater. 26 (2016) 5884.

[44] R. Galceran, I. Fina, J. Cisnero-Fernandez, B. Bozzo, C. Frontera, L. Lopez-Mir, H. Deniz, H.-W. Park, B.-G. Park, L. Balcells, X. Marti, T. Jungwirth, B. Martinez, Isothermal anisotropic magnetoresistance in antiferromagnetic metallic IrMn, Sci. Rep. 6 (2016) 35471.

[45] I. Fina, X. Marti, D. Yi, J. Liu, J.H. Chu, C. Rayan-Serrao, S. Suresha, A.B. Shick, J. Zelezný, T. Jungwirth, J. Fontcuberta, R. Ramesh, Anisotropic magnetoresistance in an antiferromagnetic semiconductor, Nat. Commun. 5 (2014) 4671.

[46] J.D. Burton, R.F. Sabirianov, J.P. Velev, O.N. Mryasov, E.Y. Tsymbal, The Origin of Tunneling Anisotropic Magnetoresistance in Break Junctions, arXiv:0703345. (2007).

[47] B.G. Park, J. Wunderlich, D.A. Williams, S.J. Joo, K.Y. Jung, K.H. Shin, K. Olejnik, A.B. Shick, T. Jungwirth, Tunneling Anisotropic Magnetoresistance in Multilayer-(Co/Pt)/AlOx/Pt Structures, Phys. Rev. Lett. 100 (2008) 87204.

[48] A.B. Shick, S. Khmelevskyi, O.N. Mryasov, J. Wunderlich, T. Jungwirth, Spin-orbit coupling induced anisotropy effects in bimetallic antiferromagnets: A route towards antiferromagnetic spintronics, Phys. Rev. B. 81 (2010) 212409.

[49] K. Wang, J.G.M. Sanderink, T. Bolhuis, W.G. van der Wiel, M.P. de Jong, Tunnelling anisotropic magnetoresistance due to antiferromagnetic CoO tunnel barriers, Sci. Rep. 5 (2015) 15498.

[50] H. Reichlová, V. Novák, Y. Kurosaki, M. Yamada, H. Yamamoto, A. Nishide, J. Hayakawa, H. Takahashi, M. Maryško, J. Wunderlich, X. Marti, T. Jungwirth, Temperature and thickness dependence of tunneling anisotropic magnetoresistance in exchange-biased Py/IrMn/MgO/Ta stacks, Mater. Res. Express. 3 (2016) 76406.

[51] J.E. Hirsch, Spin Hall Effect, Phys. Rev. Lett. 83 (1999) 1834.

[52] A. Hoffmann, Spin Hall Effects in Metals, IEEE Trans. Magn. 49 (2013) 5172.

[53] S. Mizukami, Y. Ando, T. Miyazaki, The Study on Ferromagnetic Resonance Linewidth for NM/80NiFe/NM (NM=Cu, Ta, Pd and Pt) Films, Jpn. J. Appl. Phys. 40 (2001) 580.

[54] O. Mosendz, J.E. Pearson, F.Y. Fradin, G.E.W. Bauer, S.D. Bader, A. Hoffmann, Quantifying Spin Hall Angles from Spin Pumping : Experiments and Theory, Phys. Rev. Lett. 104 (2010) 46601.

[55] K. Uchida, S. Takahashi, K. Harii, J. Ieda, W. Koshibae, K. Ando, S. Maekawa, E. Saitoh, Observation of the spin Seebeck effect, Nature. 455 (2008) 778.

[56] E. Saitoh, M. Ueda, H. Miyajima, G. Tatara, Conversion of spin current into charge current at room temperature: Inverse spin-Hall effect, Appl. Phys. Lett. 88 (2006) 182509.

[57] D. Qu, S.Y. Huang, C.L. Chien, Inverse spin Hall effect in Cr: Independence of antiferromagnetic ordering, Phys. Rev. B. 92 (2015) 20418.

[58] V.Tshitoyan, C. Ciccarelli, A. P. Mihai, M. Ali, A.C. Irvine, T.A. Moore, T. Jungwirth, A.J. Ferguson, Electrical manipulation of ferromagnetic NiFe by antiferromagnetic IrMn, Phys. Rev. B. 92 (2015) 214406.

[59] S.M. Wu, W. Zhang, A. KC, P. Borisov, J.E. Pearson, J.S. Jiang, D. Lederman, A. Hoffmann, A. Bhattacharya, Antiferromagnetic spin Seebeck Effect, Phys. Rev. Lett. (2016) 97204.

[60] Y. Ou, S. Shi, D.C. Ralph, R.A. Buhrman, Strong Spin Hall Effect in the Antiferromagnet PtMn, Phys. Rev. B. 93 (2016) 220405.

[61] H. Reichlová, D. Kriegner, V. Holý, K. Olejnik, V. Novák, M. Yamada, K. Miura, S. Ogawa, H. Takahashi, T. Jungwirth, J. Wunderlich, Current induced torques in structures with ultra-thin IrMn antiferromagnet, Phys. Rev. B. 92 (2015) 165424.

[62] S. Fukami, C. Zhang, S. Dutta Gupta, A. Kurenkov, H. Ohno, Magnetization switching by spin-orbit torque in an antiferromagnet/ferromagnet bilayer system, Nat. Mater. 15 (2016) 535.

[63] Y.-C. Lau, D. Betto, K. Rode, J.M.D. Coey, P. Stamenov, Spin-orbit torque switching without external field with a ferromagnetic exchange-biased coupling layer, Nat. Nanotechnol. 11 (2016) 758.

[64] A.V.D. Brink, G. Vermijs, A. Solignac, J. Koo, J.T. Kohlhepp, H.J.M. Swagten, B. Koopmans, Field-free magnetization reversal by spin-Hall effect and exchange bias, Nat. Commun. 7 (2016) 10854.

[65] J. Sklenar, W. Zhang, M.B. Jungfleisch, W. Jiang, H. Saglam, J.E. Pearson, J.B. Ketterson, A. Hoffmann, Spin Hall effects in metallic antiferromagnets – perspectives for future spin-orbitronics, AIP Adv. 6 (2016) 55603.

[66] Y.-W. Oh, S.-H. Chris Baek, Y.M. Kim, H.Y. Lee, K.-D. Lee, C.-G. Yang, E.-S. Park, K.-S. Lee, K.-W. Kim, G. Go, J.-R. Jeong, B.-C. Min, H.-W. Lee, K.-J. Lee, B.-G. Park, Field-free switching of perpendicular magnetization through spin–orbit torque in antiferromagnet/ferromagnet/oxide structures, Nat. Nanotechnol. 11 (2016) 878.

[67] A.V. Kimel, A. Kirilyuk, A. Tsvetkov, R.V. Pisarev, T. Rasing, Laser-induced ultrafast spin reorientation in the antiferromagnet TmFeO3, Nature. 429 (2004) 850.

[68] N.P. Duong, T. Satoh, M. Fiebig, Ultrafast manipulation of antiferromagnetism in NiO, Phys. Rev. Lett. 93 (2004) 117402.

[69] A.V. Kimel, B.A. Ivanov, R.V. Pisarev, P.A. Usachev, A. Kirilyuk, T. Rasing, Inertia-driven spin switching in antiferromagnets, Nat. Phys. 5 (2009) 727.

[70] M. Fiebig, V.V. Pavlov, R.V. Pisarev, Second-harmonic generation as a tool for studying electronic and magnetic structures of crystals: review, J. Opt. Soc. Am. B. 22 (2005) 96.

[71] T. Seifert, S. Jaiswal, U. Martens, J. Hannegan, L. Braun, P. Maldonado, F. Freimuth, A. Kronenberg, J. Henrizi, I. Radu, E. Beaurepaire, Y. Mokrousov, P.M. Oppeneer, M. Jourdan, G. Jakob, D. Turchinovich, L.M. Hayden, M. Wolf, M. Münzenberg, M. Kläui, T. Kampfrath, Efficient metallic spintronic emitters of ultrabroadband terahertz radiation, Nat. Photonics. 10 (2016) 483.

[72] V. Saidl, P. Němec, P. Wadley, V. Hills, R.P. Campion, V. Novák, K.W. Edmonds, F. Maccherozzi, S.S. Dhesi, B.L. Gallagher, F. Trojánek, J. Kuneš, J. Železný, P. Malý, and T. Jungwirth, Optical determination of the Néel vector in a CuMnAs thin-film antiferromagnet, Nat. Photonics. 11 (2017) 91.

[73] A. V Kimel, A. Kirilyuk, P.A. Usachev, R. V Pisarev, A.M. Balbashov, T. Rasing, Ultrafast non-thermal control of magnetization by instantaneous photomagnetic pulses, Nature. 435 (2005) 655.

[74] S.Y. Bodnar, L. Šmejkal, I. Turek, T. Jungwirth, O. Gomonay, J. Sinova, A.A. Sapozhnik, H.-J. Elmers, M. Kläui, M. Jourdan, Writing and Reading antiferromagnetic Mn2Au: Néel spin-orbit torques and large anisotropic magnetoresistance, ArXiv:1706.02482. (2017).

[75] M. Meinert, D. Graulich, T. Matalla-Wagner, Key role of thermal activation in the electrical switching of antiferromagnetic Mn2Au, ArXiv:1706.06983. (2017).

[76] P.E. Roy, R.M. Otxoa, J. Wunderlich, Robust picosecond writing of a layered antiferromagnet by staggered spin-orbit fields, Phys. Rev. B. 94 (2016) 14439.

[77] T.L. Gilbert, J.. M. Kelly, Anomalous rotational damping in ferromagnetic sheets, Conf. Magn. Magn. Mater. Pittsburgh, PA. (1955) 14.

[78] T.L. Gilbert, Classics in Magnetics A Phenomenological Theory of Damping in Ferromagnetic Materials, IEEE Trans. Magn. 40 (2004) 3443.

[79] L. Landau, E. Lifshitz, On the theory of the dispersion of magnetic permeability in ferromagnetic bodies, Phys. Z. Sowjetunion. 8 (1935) 153.

[80] H. Suhl, Theory of the magnetic damping constant, IEEE Trans. Magn. 34 (1998) 1834.

[81] J.A.C. Bland, B. Heinrich, Ultrathin Magnetic Structures III, Springer, New York, (2005).

[82] R.A. Lukaszew, Handbook of Nanomagnetism: Applications and Tools, CRC Press, (2015).

[83] B. Heinrich, D. Fraitova, V. Kambersky, The Influence of s-d Exchange on Relaxation of Magnons in Metals, Phys. Status Solidi. 23 (1967) 501.

[84] V. Kamberský, Spin-orbital Gilbert damping in common magnetic metals, Phys. Rev. B. 76 (2007) 134416.

[85] K. Gilmore, Y.U. Idzerda, M.D. Stiles, Identification of the Dominant Precession-Damping Mechanism in Fe, Co, and Ni by First-Principles Calculations, Phys. Rev. Lett. 99 (2007) 27204.

[86] M.J. Hurben, C.E. Patton, Theory of two magnon scattering microwave relaxation and ferromagnetic resonance linewidth in magnetic thin films, J. Appl. Phys. 83 (1998) 4344.

[87] R. Arias, D. Mills, Extrinsic contributions to the ferromagnetic resonance response of ultrathin films, J. Appl. Phys. 87 (2000) 5455.

[88] P. Landeros, R.E. Arias, D.L. Mills, Two magnon scattering in ultrathin ferromagnets: The case where the magnetization is out of plane, Phys. Rev. B. 77 (2008) 214405.

[89] K. Lenz, H. Wende, W. Kuch, K. Baberschke, K. Nagy, A. Jánossy, Two-magnon scattering and viscous Gilbert damping in ultrathin ferromagnets, Phys. Rev. B. 73 (2006) 144424.

[90] J. H. Van Vleck and R. Orbach, Ferrimagnetic resonance of dilute bare-earth doped iron garnets, Phys. Rev. Lett. 11 (1963) 65.

[91] H. Shi, D. Lederman, N.R. Dilley, R.C. Black, J. Diedrichs, K. Jensen, M.B. Simmonds, Temperature-induced sign change of the exchange bias in Fe0.82Zn0.18/F2/Co bilayers, J. Appl. Phys. 93 (2003) 8600.

[92] J.F. Dillon, Ferrimagnetic resonance in rare-earth-doped yttrium iron garnet. III. Linewidth, Phys. Rev. 127 (1962) 1495.

[93] J. Dubowik, F. Stobiecki, I. Gościańska, Y.P. Lee, A. Paetzold, K. Röll, Temperature

dependence of ferromagnetic resonance in permalloy/NiO exchange-biased films, Eur. Phys. J. B. 45 (2005) 283.

[94] P. Lubitz, M. Rubinstein, J.J. Krebs, S.F. Cheng, Frequency and temperature dependence of ferromagnetic linewidth in exchange biased Permalloy, J. Appl. Phys. 89 (2001) 6901.

[95] R.D. McMichael, C.G. Lee, M.D. Stiles, F.G. Serpa, P.J. Chen, W.F. Egelhoff, Exchange bias relaxation in CoO-biased films, J. Appl. Phys. 87 (2000) 6406.

[96] M. Gloanec, S. Rioual, B. Lescop, R. Zuberek, R. Szymczak, P. Aleshkevych, B. Rouvellou, Dynamical effect in measurement of the exchange-bias field: A consequence of the slow-relaxer mechanism, Phys. Rev. B. 80 (2009) 220404.

[97] S.P. Dash, S. Sharma, J.C. Le Breton, J. Peiro, H. Jaffrès, J.M. George, A. Lemaître, R. Jansen, Spin precession and inverted Hanle effect in a semiconductor near a finite-roughness ferromagnetic interface, Phys. Rev. B. 84 (2011) 54410.

[98] Y. Tserkovnyak, A. Brataas, G.E.W. Bauer, B.I. Halperin, Nonlocal magnetization dynamics in ferromagnetic heterostructures, Rev. Mod. Phys. 77 (2005) 1375.

[99] V. Flovik, F. Macia, A.D. Kent, E. Wahlström, Eddy current interactions in a ferromagnet-normal metal bilayer structure, and its impact on ferromagnetic resonance lineshapes, J. Appl. Phys. 117 (2015) 143902.

[100] V. Flovik, B.H. Pettersen, E. Wahlström, Eddy-current effects on ferromagnetic resonance: Spin wave excitations and microwave screening effects, J. Appl. Phys. 119 (2016) 163903.

[101] Y. Tserkovnyak, A. Brataas, G.E.W. Bauer, Spin pumping and magnetization dynamics in metallic multilayers, Phys. Rev. B. 66 (2002) 224403.

[102] A. Brataas, Y. Tserkovnyak, G.E.W. Bauer, B.I. Halperin, Spin battery operated by ferromagnetic resonance, Phys. Rev. B. 66 (2002) 60404.

[103] M. V. Costache, S.M. Watts, C.H. Van Der Wal, B.J. Van Wees, Electrical detection of spin pumping: Dc voltage generated by ferromagnetic resonance at ferromagnet/nonmagnet contact, Phys. Rev. B. 78 (2008) 64423.

[104] B. Hillebrands, Modern techniques for characterizing magnetic materials, Springer, (2005).

[105] S.S. Kalarickal, P. Krivosik, M. Wu, C.E. Patton, M.L. Schneider, P. Kabos, T.J. Silva, J.P. Nibarger, Ferromagnetic resonance linewidth in metallic thin films: Comparison of measurement methods, J. Appl. Phys. 99 (2006) 93909.

[106] C.G. Shull, E.O. Wollan, W.C. Koehler, Neutron scattering and polarization by ferromagnetic materials, Phys. Rev. 84 (1951) 912.

[107] S. Pizzini, J. Vogel, M. Bonfim, A. Fontaine, Time-resolved X-ray magnetic circular dichroism: a selective probe of magnetization dynamics on nanosecond timescales, in: Spin Dyn. Confin. Magn. Struct. II, Springer, (2003), 157–187.

[108] M. Grimsditch, P. Vavassori, The diffracted magneto-optic Kerr effect: what does it tell you?, J. Phys. Condens. Matter. 16 (2004) 275.

[109] A. Ghosh, Spin pumping and spin absorption in magnetic heterostructures, PhD thesis manuscript, University of Grenoble, (2013).

[110] W.R. Hagen, Biomolecular EPR Spectroscopy, CRC Press, (2008).

[111] N. Behera, S. Chaudhary, D.K. Pandya, Anomalous anti-damping in sputtered β-Ta/Py bilayer system, Sci. Rep. 6 (2016) 19488.

[112] N. Behera, A. Kumar, S. Chaudhary, D.K. Pandya, Two magnon scattering and anti-damping behavior in a two-dimensional epitaxial TiN/Py(t Py)/β-Ta(t Ta) system, RSC Adv. 7 (2017) 8106.

[113] A. Ruiz-Calaforra, T. Brächer, V. Lauer, P. Pirro, B. Heinz, M. Geilen, A. V. Chumak, A. Conca, B. Leven, B. Hillebrands, The role of the non-magnetic material in spin pumping and magnetization dynamics in NiFe and CoFeB multilayer systems, J. Appl.

Phys. 117 (2015) 163901.
[114] G. Counil, T. Devolder, J. V. Kim, P. Crozat, C. Chappert, S. Zoll, R. Fournel, Temperature dependences of the resistivity and the ferromagnetic resonance linewidth in permalloy thin films, IEEE Trans. Magn. 42 (2006) 3323.
[115] M.A.W. Schoen, J. Lucassen, H.T. Nembach, B. Koopmans, T.J. Silva, H. Back, J.M. Shaw, Magnetic properties in ultrathin 3d transition-metal alloys II : Experimental verification of quantitative theories of damping and spin-pumping, Phys. Rev. B. 95 (2017) 134411.
[116] Y. Zhao, Q. Song, S.-H. Yang, T. Su, W. Yuan, S.S.P. Parkin, J. Shi, W. Han, Experimental Investigation of Temperature-Dependent Gilbert Damping in Permalloy Thin Films, Sci. Rep. 6 (2016) 22890.
[117] X. Liu, W. Zhang, M.J. Carter, G. Xiao, Ferromagnetic resonance and damping properties of CoFeB thin films as free layers in MgO-based magnetic tunnel junctions, J. Appl. Phys. 110 (2011) 33910.
[118] J. Smit, H.G. Beljers, Ferromagnetic resonance absorption in BaFeO, a highly anisotropic crystal, Philips Res. Rep. 10 (1955) 113.
[119] H. Puszkarski, M. Kasperski, On the Interpretation of the Angular Dependence of the Main FMR/SWR Line in Ferromagnetic Thin Films, Acta Phys. Pol. A. 121 (2012) 1165.
[120] J.M.L. Beaujour, W. Chen, K. Krycka, C.C. Kao, J.Z. Sun, A.D. Kent, Ferromagnetic resonance study of sputtered Co|Ni multilayers, Eur. Phys. J. B. 59 (2007) 475.
[121] J.C. Rojas-Sánchez, M. Cubukcu, A. Jain, C. Vergnaud, C. Portemont, C. Ducruet, A. Barski, A. Marty, L. Vila, J.P. Attané, E. Augendre, G. Desfonds, S. Gambarelli, H. Jaffrès, J.M. George, M. Jamet, Spin pumping and inverse spin Hall effect in germanium, Phys. Rev. B. 88 (2013) 64403.
[122] H. Wang, C. Du, P.C. Hammel, F. Yang, Antiferromagnetic spin transport from YIG into NiO, Phys. Rev. Lett. 113 (2014) 97202.
[123] A. Ghosh, S. Auffret, U. Ebels, W.E. Bailey, Penetration Depth of Transverse Spin Current in Ultrathin Ferromagnets, Phys. Rev. Lett. 109 (2012) 127202.
[124] Y. Ohnuma, H. Adachi, E. Saitoh, S. Maekawa, Enhanced dc spin pumping into a fluctuating ferromagnet near TC, Phys. Rev. B. 89 (2014) 174417.
[125] Y. Tserkovnyak, A. Brataas, G.E.W. Bauer, Enhanced Gilbert Damping in Thin Ferromagnetic Films, Phys. Rev. Lett. 88 (2002) 117601.
[126] D. Petti, E. Albisetti, H. Reichlová, J. Gazquez, M. Varela, M. Molina-Ruiz, A.F. Lopeandia, K. Olejnik, V. Novák, I. Fina, B. Dkhil, J. Hayakawa, X. Marti, J. Wunderlich, T. Jungwirth, R. Bertacco, Storing magnetic information in IrMn/MgO/Ta tunnel junctions via field-cooling, Appl. Phys. Lett. 102 (2013) 192404.
[127] S. Soeya, T. Imagawa, K. Mitsuoka, S. Narishige, Distribution of blocking temperature in bilayered Ni81Fe19/NiO films, J. Appl. Phys. 76 (1994) 5356.
[128] V. Baltz, B. Rodmacq, A. Zarefy, L. Lechevallier, B. Dieny, Bimodal distribution of blocking temperature in exchange-biased ferromagnetic/antiferromagnetic bilayers, Phys. Rev. B. 81 (2010) 52404.
[129] T. Yamaoka, M. Mekata, H. Takaki, Neutron diffraction study of antiferromagnetism in face-centered cubic Mn-Ir alloys, J. Phys. Soc. Japan. 31 (1971) 301.
[130] T. Ambrose, C.L. Chien, Finite-size effects and uncompensated magnetization in thin antiferromagnetic CoO layers, Phys. Rev. Lett. 76 (1996) 1743.
[131] E. Abarra, K. Takano, F. Hellman, A. Berkowitz, Thermodynamic Measurements of Magnetic Ordering in Antiferromagnetic Superlattices, Phys. Rev. Lett. 77 (1996) 3451.
[132] F. Boakye, G. Adanu, The Néel temperature of Alpha-Mn thin films, Thin Solid Films. 279 (1996) 29.
[133] K. Akmaldinov, C. Ducruet, C. Portemont, I. Joumard, I.L. Prejbeanu, B. Dieny, V.

Baltz, Mixing antiferromagnets to tune NiFe-[IrMn/FeMn] interfacial spin-glasses, grains thermal stability and related exchange bias properties, J. Appl. Phys. 115 (2014) 17B718.
[134] K. Akmaldinov, S. Auffret, I. Joumard, B. Dieny, V. Baltz, Benefit of inserting a (Cu/Pt) intermixing dual barrier for the blocking temperature distribution of exchange biased Co/(Cu/Pt)/IrMn stacks, Appl. Phys. Lett. 103 (2013) 42415.
[135] M.D. Stiles, A. Zangwill, Anatomy of spin-transfer torque, Phys. Rev. B. 66 (2002) 14407.
[136] M. Zwierzycki, Y. Tserkovnyak, P.J. Kelly, A. Brataas, G.E.W. Bauer, First-principles study of magnetization relaxation enhancement and spin transfer in thin magnetic films, Phys. Rev. B. 71 (2005) 64420.
[137] I. Tomeno, H.N. Fuke, H. Iwasaki, M. Sahashi, Y. Tsunoda, Magnetic neutron scattering study of ordered Mn3Ir, J. Appl. Phys. 86 (1999) 3853.
[138] Z.Q. Qiu, J. Li, D. Hou, E. Arenholz, A.T.N. Diaye, A. Tan, K. Sato, S. Okamoto, Y. Tserkovnyak, Z.Q. Qiu, E. Saitoh, A.T. N'Diaye, A. Tan, K. Uchida, K. Sato, S. Okamoto, Y. Tserkovnyak, Z.Q. Qiu, E. Saitoh, Spin-current probe for phase transition in an insulator, Nat. Commun. 7 (2016) 12670.
[139] R. Zhang, R.F. Willis, Thickness-dependent curie temperatures of ultrathin magnetic films: Effect of the range of spin-spin interactions, Phys. Rev. Lett. 86 (2001) 2665.
[140] H.L. Wang, C.H. Du, Y. Pu, R. Adur, P.C. Hammel, F.Y. Yang, Scaling of spin hall angle in 3d, 4d, and 5d metals from Y3Fe5O12/metal spin pumping, Phys. Rev. Lett. 112 (2014) 197201.
[141] C. Kittel, Introduction to Solid State Physics, (5th Edition) by John Wiley & Sons NY, (1976).
[142] A.F. Kravets, O. V. Gomonay, D.M. Polishchuk, Y.O. Tykhonenko-Polishchuk, T.I. Polek, A.I. Tovstolytkin, V. Korenivski, Effect of nanostructure layout on spin pumping phenomena in antiferromagnet/ nonmagnetic metal/ ferromagnet multilayered stacks, AIP Adv. 7 (2017) 56312.
[143] T. Mewes, R.L. Stamps, H. Lee, E. Edwards, M. Bradford, C.K.A. Mewes, Z. Tadisina, S. Gupta, Unidirectional magnetization relaxation in exchange-biased films, IEEE Magn. Lett. 1 (2010) 3500204.
[144] R. Khymyn, I. Lisenkov, V.S. Tiberkevich, A.N. Slavin, B.A. Ivanov, Transformation of spin current by antiferromagnetic insulators, Phys. Rev. B. 93 (2016) 224421.
[145] W. Lin, K. Chen, S. Zhang, C.L. Chien, Enhancement of Thermally Injected Spin Current through an Antiferromagnetic Insulator, Phys. Rev. Lett. 116 (2016) 186601.
[146] S.M. Rezende, R.L. Rodríguez-Suárez, A. Azevedo, Diffusive magnonic spin transport in antiferromagnetic insulators, Phys. Rev. B. 93 (2016) 54412.
[147] C.E. Patton, C.H. Wilts, Temperature Dependence of the Ferromagnetic Resonance Linewidth in Thin Ni-Fe Films, J. Appl. Phys. 38 (1967) 3537.
[148] V.L. Safonov, H.N. Bertram, Linear stochastic magnetization dynamics and microscopic relaxation mechanisms, J. Appl. Phys. 94 (2003) 529.
[149] M. Dıáz De Sihues, P.J. Silva, J.R. Fermin, Effect of temperature on the ferromagnetic resonance of Ni50Fe50 thin films, Phys. B. 354 (2004) 361.
[150] J.F. Sierra, V. V Pryadun, F.G. Aliev, S.E. Russek, M. García-Hernández, E. Snoeck, V. V Metlushko, Temperature dependent dynamic and static magnetic response in magnetic tunnel junctions with Permalloy layers, Appl. Phys. Lett. 93 (2008) 172510.
[151] J.F. Sierra, V. V Pryadun, S.E. Russek, M. García-Hernández, F. Mompean, R. Rozada, O. Chubykalo-Fesenko, E. Snoeck, G.X. Miao, J.S. Moodera, F.G. Aliev, Interface and Temperature Dependent Magnetic Properties in Permalloy Thin Films and Tunnel Junction Structures, J. Nanosci. Nanotechnol. 11 (2011) 7653.

[152] R.A. Pollak, C.H. Bajorek, Surface composition and chemistry of evaporated Permalloy films observed by x-ray photoemission spectroscopy and by Auger electron spectroscopy, J. Appl. Phys. 46 (1975) 1382.
[153] S.M. Bhagat, P. Lubitz, Temperature variation of ferromagnetic relaxation in the 3d transition metals, Phys. Rev. B. 10 (1974) 179.
[154] B.L. Zink, M. Manno, L. O'Brien, J. Lotze, M. Weiler, D. Bassett, S.J. Mason, S.T.B. Goennenwein, M. Johnson, C. Leighton, Efficient spin transport through native oxides of nickel and permalloy with platinum and gold overlayers, Phys. Rev. B. 93 (2016) 184401.
[155] Y. Zhao, Q. Song, S.-H. Yang, T. Su, W. Yuan, S.S.P. Parkin, J. Shi, W. Han, Experimental Investigation of Temperature-Dependent Gilbert Damping in Permalloy Thin Films, Sci. Rep. 6 (2016) 22890.
[156] V.L. Safonov, H.N. Bertram, Impurity relaxation mechanism for dynamic magnetization reversal in a single domain grain, Phys. Rev. B. 61 (2000) 14893.
[157] A.M. Clogston, Relaxation phenomena in ferrites, Bell Syst. Tech. J. 34 (1955) 739.
[158] P. Lubitz, J.J. Krebs, M.M. Miller, S. Cheng, Temperature dependence of ferromagnetic resonance as induced by NiO pinning layers, J. Appl. Phys. 83 (1998) 6819.
[159] M. Fitzsimmons, T. Silva, T. Crawford, Surface oxidation of Permalloy thin films, Phys. Rev. B. 73 (2006) 14420.
[160] J. Dubowik, F. Stobiecki, I. Goscianska, Y.P. Lee, A. Paetzold, K. Roll, Enhanced Spin-Wave Damping in Exchange-Biased Films, J. Korean Phys. Soc. 45 (2004) 42.
[161] X.Y. Lang, W.T. Zheng, Q. Jiang, Size and interface effects on ferromagnetic and antiferromagnetic transition temperatures, Phys. Rev. B. 73 (2006) 224444.
[162] D. Alders, L. Tjeng, F. Voogt, T. Hibma, G. Sawatzky, C. Chen, J. Vogel, M. Sacchi, S. Iacobucci, Temperature and thickness dependence of magnetic moments in NiO epitaxial films, Phys. Rev. B. 57 (1998) 11623.
[163] C. Boeglin, O. Ersen, M. Pilard, V. Speisser, F. Kronast, Temperature dependence of magnetic coupling in ultrathin NiO/Fe3O4 (001) films, Phys. Rev. B. 80 (2009) 35409.
[164] D. Hou, Z. Qiu, J. Barker, K. Sato, K. Yamamoto, S. Vélez, J.M. Gomez-Perez, L.E. Hueso, F. Casanova, E. Saitoh, Tunable Sign Change of Spin Hall Magnetoresistance in Pt/NiO/YIG Structures, Phys. Rev. Lett. 118 (2017) 147202.
[165] W. Lin, C.L. Chien, Electrical Detection of Spin Backflow from an Antiferromagnetic Insulator/ Y3Fe5O12 Interface, Phys. Rev. Lett. 118 (2017) 67202.
[166] B. Gu, T. Ziman, S. Maekawa, Theory of the spin Hall effect, and its inverse, in a ferromagnetic metal near the Curie temperature, Phys. Rev. B. 86 (2012) 241303.
[167] D.H. Wei, Y. Niimi, B. Gu, T. Ziman, S. Maekawa, Y. Otani, The spin Hall effect as a probe of nonlinear spin fluctuations, Nat. Commun. 3 (2012) 1058.
[168] J. Sinova, S.O. Valenzuela, J. Wunderlich, C.H. Back, T. Jungwirth, Spin Hall effects, Rev. Mod. Phys. 87 (2015) 1213.
[169] J. Sinova, D. Culcer, Q. Niu, N.A. Sinitsyn, T. Jungwirth, A.H. MacDonald, Universal intrinsic spin Hall effect, Phys. Rev. Lett. 92 (2004) 126603.
[170] J. Smit, J. Volger, Spontaneous Hall effect in ferromagnetics, Phys. Rev. 92 (1953) 1576.
[171] J. Smith, The spontaneous Spin Hall Effect in ferromagnetics II, Physica. 24 (1958) 39.
[172] L. Berger, Side-jump mechanism for the hall effect of ferromagnets, Phys. Rev. B. 2 (1970) 4559.
[173] G. Vignale, Ten years of spin Hall effect, J. Supercond. Nov. Magn. 23 (2010) 3.
[174] R. Iguchi, E. Saitoh, Measurement of Spin Pumping Voltage Separated from Extrinsic Microwave Effects, J. Phys. Soc. Jpn. 86 (2017) 11003.
[175] H.J. Juretschke, Electromagnetic Theory of dc Effects in Ferromagnetic Resonance, J. Appl. Phys. 31 (1960) 1401.

[176] M. Harder, Y. Gui, C. Hu, Electrical detection of magnetization dynamics via spin rectification effects, Phys. Rep. 661 (2016) 1.
[177] S.O. Valenzuela, M. Tinkham, Direct electronic measurement of the spin Hall effect, Nature. 442 (2006) 176.
[178] L. Liu, C.-F. Pai, Y. Li, H.W. Tseng, D.C. Ralph, R.A. Buhrman, Spin-Torque Switching with the Giant Spin Hall Effect of Tantalum, Science. 336 (2012) 555.
[179] K. Ando, E. Saitoh, Inverse spin-Hall effect in palladium at room temperature, J. Appl. Phys. 108 (2010) 113925.
[180] T. Kimura, Y. Otani, T. Sato, S. Takahashi, S. Maekawa, Room-Temperature Reversible Spin Hall Effect, Phys. Rev. Lett. 98 (2007) 156601.
[181] T. Tanaka, H. Kontani, M. Naito, T. Naito, D.S. Hirashima, K. Yamada, J. Inoue, Intrinsic spin Hall effect and orbital Hall effect in 4d and 5d transition metals, Phys. Rev. B. 77 (2008) 165117.
[182] J.-C. Rojas-Sánchez, N. Reyren, P. Laczkowski, W. Savero, J.-P. Attané, C. Deranlot, M. Jamet, J.-M. George, L. Vila, H. Jaffrès, Spin Pumping and Inverse Spin Hall Effect in Platinum: The Essential Role of Spin-Memory Loss at Metallic Interfaces, Phys. Rev. Lett. 112 (2014) 106602.
[183] W. J.S. Garcia, R. L. Seeger, R. B. da Silva, A. Harres, Inverse spin Hall and spin rectification effects in NiFe/FeMn exchange-biased thin films, J. Magn. Magn. Mater. 441 (2017) 392.
[184] M. Ranjbar, P. Durrenfeld, M. Haidar, E. Iacocca, M. Balinskiy, T.Q. Le, M. Fazlali, A. Houshang, A.A. Awad, R.K. Dumas, J. Akerman, CoFeB-Based Spin Hall Nano-Oscillators, IEEE Magn. Lett. 5 (2014) 3000504.
[185] T. Wang, W. Wang, Y. Xie, M.A. Warsi, J. Wu, Y. Chen, V.O. Lorenz, X. Fan, J.Q. Xiao, Large spin Hall angle in vanadium film, Sci. Rep. 7 (2017) 1306.
[186] A. Azevedo, O.A. Santos, R.O. Cunha, R. Rodríguez-Suárez, S.M. Rezende, Addition and subtraction of spin pumping voltages in magnetic hybrid structures, Appl. Phys. Lett. 104 (2014) 152408.
[187] B.F. Miao, S.Y. Huang, D. Qu, C.L. Chien, Inverse spin hall effect in a ferromagnetic metal, Phys. Rev. Lett. 111 (2013) 66602.
[188] A. Tsukahara, Y. Ando, Y. Kitamura, H. Emoto, E. Shikoh, M.P. Delmo, T. Shinjo, M. Shiraishi, Self-induced inverse spin Hall effect in permalloy at room temperature, Phys. Rev. B. 89 (2014) 235317.
[189] A. Azevedo, O.A. Santos, G.A.F. Guerra, R.O. Cunha, R. Rodríguez-Suárez, S.M. Rezende, Competing spin pumping effects in magnetic hybrid structures, Appl. Phys. Lett. 104 (2014) 52402.
[190] A. Azevedo, R.O. Cunha, F. Estrada, O. Alves Santos, J.B.S. Mendes, L.H. Vilela-Leão, R.L. Rodríguez-Suárez, S.M. Rezende, Electrical detection of ferromagnetic resonance in single layers of permalloy: Evidence of magnonic charge pumping, Phys. Rev. B. 92 (2015) 24402.
[191] C. Ciccarelli, K.M.D. Hals, A. Irvine, V. Novak, Y. Tserkovnyak, H. Kurebayashi, A. Brataas, A. Ferguson, Magnonic charge pumping via spin–orbit coupling, Nat. Nanotechnol. 10 (2015) 50.
[192] W.H. Meiklejohn, C.P. Bean, New Magnetic Anisotropy, Phys. Rev. 102 (1956) 1413.
[193] W.H. Meiklejohn, C.P. Bean, New Magnetic Anisotropy, Phys. Rev. 105 (1957) 904.
[194] F. Radu, H. Zabel, Magnetic Heterostructures, Chapter 3: Exchange Bias Effect of Ferro-/Antiferromagnetic Heterostructures, Springer, (2007).
[195] W.H. Meiklejohn, Exchange anisotropy–a review, J. Appl. Phys. 33 (1962) 1328.
[196] L. Néel, Étude théorique du couplage ferro-antiferromagnetique dans les couches minces, Ann. Phys. (Paris). 14 (1967) 61.

[197] D. Mauri, H.C. Siegmann, P.S. Bagus, E. Kay, Simple model for thin ferromagnetic films exchange coupled to an antiferromagnetic substrate, J. Appl. Phys. 62 (1987) 3047.

[198] A.P. Malozemoff, Random-field model of exchange anisotropy at rough ferromagnetic-antiferromagnetic interfaces, Phys. Rev. B. 35 (1987) 3679.

[199] Y. Imry, S. Ma, Random-field instability of the ordered state of continuous symmetry, Phys. Rev. Lett. 35 (1975) 1399.

[200] K. Takano, R.H. Kodama, A.E. Berkowitz, W. Cao, G. Thomas, Interfacial Uncompensated Antiferromagnetic Spins: Role in Unidirectional Anisotropy in Polycrystalline Ni81Fe19/CoO Bilayers, Phys. Rev. Lett. 79 (1997) 1130.

[201] V. Baltz, Antiferromagnets for spintronics: exchange bias, spin dependent transport, HDR Thesis (Habilitation à diriger des recherches), University of Grenoble, (2014).

[202] S. Soeya, T. Imagawa, K. Mitsuoka, S. Narishige, Distribution of blocking temperature in bilayered Ni81Fe19/Ni0 films, J. Appl. Phys. 76 (1994) 5356.

[203] J.M. Slaughter, N.D. Rizzo, F.B. Mancoff, R. Whig, K. Smith, S. Aggarwal, S. Tehrani, Toggle and Spin-Torque MRAM: Status and Outlook, J. Magn. Soc. Japan. 5 (2010) 171.

[204] L. Lechevallier, A. Zarefy, R. Lardé, H. Chiron, J.-M. Le Breton, V. Baltz, B. Rodmacq, B. Dieny, Structural analysis and magnetic properties of (Pt/Co)3/Pt/IrMn multilayers, Phys. Rev. B. 79 (2009) 174434.

[205] F. Letellier, L. Lechevallier, R. Lardé, J.-M. Le Breton, K. Akmaldinov, S. Auffret, B. Dieny, V. Baltz, Direct imaging of thermally-activated grain-boundary diffusion in Cu/Co/IrMn/Pt exchange-bias structures using atom-probe tomography, J. Appl. Phys. 116 (2014) 203906.

[206] K. O’Grady, L.E. Fernández-Outón, G. Vallejo-Fernandez, A new paradigm for exchange bias in polycrystalline thin films, J. Magn. Magn. Mater. 322 (2010) 883.

Abstract

Antiferromagnetic spintronics is an emerging research field in the area of information technology that exploits the unique combination of properties of antiferromagnets. It is their high excitation frequency, robustness against external fields, zero net magnetization and possibility of generating large magneto-transport effects that makes them so interesting. Spin transfer, spin-orbit coupling and spin caloritronics constitute the phenomena that have shaped much of the recent research and development towards pure antiferromagnetic spintronics. Here we investigate spin transfer torque and spin pumping in both metallic and insulating antiferromagnets by means of ferromagnetic resonance technique, in ferromagnetic spin injector – NiFe, CoFeB / (spin conductor – Cu) / antiferromagnetic spin sink – IrMn, NiFeOx, NiO trilayers. Temperature dependence measurements of the ferromagnetic relaxation revealed a novel spin pumping effect associated to the linear fluctuations at the magnetic phase transition of the antiferromagnet, regardless its electronic state and the nature of the spin transport. This opens new ways towards more efficient spin pumping, while providing at the same time a versatile method to probe the critical temperature of ultrathin films with zero net magnetization. Next, in an effort to probe linear as well as non-linear fluctuations in the antiferromagnet we conducted electrical measurements in spin Hall geometry. A novel non-monotonous temperature dependence of transverse dc voltage was sometimes observed, mostly associated to the properties of a specific ferromagnet: Permalloy, unrelated to spin rectification effects. These findings add to a growing body of literature on spin current absorption, highlighting the ability of ferromagnets to act as spin current detectors, in phenomena involving magnetization dynamics. Finally, we used exchange bias to investigate and subsequently engineer the magnetic and electric properties of various antiferromagnets intended for diverse spintronic applications including reading via tunneling anisotropic magnetoresistance.

Résumé

La spintronique antiferromagnétique est un domaine de recherche émergent dans le secteur des technologies de l'information. Ce domaine exploite la combinaison unique de propriétés dans les matériaux antiferromagnétiques. Leur grande fréquence d'excitation, leur robustesse face à des champs extérieurs, une aimantation totale nulle et la possibilité de générer de forts effets de magnéto-transport les rendent particulièrement intéressants. Le transfert de spin, le couplage spin-orbite et les effets caloritroniques constituent les phénomènes qui ont façonné une grande partie de la recherche et des développements récents en spintronique. Dans cette thèse, nous avons étudié les effets de transfert et de pompage de spin dans des antiferromagnétiques métalliques et isolants au moyen de la technique de résonance ferromagnétique, dans des tricouches du type injecteur de spin ferromagnétique - NiFe, CoFeB / (conducteur de spin - Cu / absorbeur de spin antiferromagnétique - IrMn, NiFeOx, NiO. Les mesures de la dépendance en température de la relaxation ferromagnétique ont révélé un nouvel effet de pompage de spin associé aux fluctuations linéaires lors de la transition de phase magnétique de l'antiferromagnétique, quel que soit l'état électronique et la nature du transport de spin. Cela ouvre de nouvelles voies pour un pompage de spin plus efficace, tout en fournissant une méthode polyvalente pour mesurer la température critique des films ultra-minces à aimantation totale nulle. Dans le but de mesurer à la fois les fluctuations de spin linéaires et non linéaires dans l'antiferromagnétique, nous avons effectué des mesures électriques dans une configuration de mesure du type ‘spin Hall’. Une dépendance en température non-monotone inédite de la tension dc transverse a parfois été observée. Elle est principalement associée aux propriétés d’un ferromagnétique spécifique : le Permalloy, sans rapport avec les effets de rectification de spin. Ces résultats s'ajoutent à une littérature croissante sur l'absorption d’un courant de spin, soulignant la capacité des ferromagnétiques à agir comme détecteurs de courant de spin émis à la suite de phénomènes impliquant une dynamique d’aimantation. Finalement, nous avons utilisé le couplage d'échange pour étudier et ensuite façonner les propriétés magnétiques et électriques de plusieurs antiferromagnétiques destinés à diverses applications spintroniques, y compris la lecture par magnétorésistance tunnel anisotrope.